CRANFIELD UNIVERSITY

FEIYANG HE

DYNAMIC RESPONSE OF 3D-PRINTED ACRYLONITRILE BUTADIENE STYRENE (ABS) DAMAGED STRUCTURE UNDER THERMO-MECHANICAL LOADS

SCHOOL OF AEROSPACE, TRANSPORT AND MANUFACTURING
PhD in Manufacturing

PhD
Academic Year: 2018 - 2021

Supervisor: Dr Muhammad Khan
Associate Supervisor: Prof Andrew Starr
September 2021

CRANFIELD UNIVERSITY

SCHOOL OF AEROSPACE, TRANSPORT AND
MANUFACTURING

PhD in Manufacturing

PhD

Academic Year 2018 - 2021

FEIYANG HE

Dynamic Response for 3D-printed Acrylonitrile Butadiene Styrene
(ABS) Damaged Structure under Thermo-mechanical Loads

Supervisor: Dr Muhammad Khan
Associate Supervisor: Prof Andrew Starr
September 2021

This thesis is submitted in partial fulfilment of the requirements for
the degree of PhD
*(NB. This section can be removed if the award of the degree is
based solely on examination of the thesis)*

ABSTRACT

Fused deposition modelling (FDM), as the most widely used additive manufacturing (AM) process, has great potential for various applications. The structures manufactured with the FDM technique has the potential to be used in a variety of complex working environments, such as the coupled thermo-mechanical loads. The coupled thermo-mechanical loads can likely lead to fatigue cracking swiftly in structures till the catastrophic failure. Therefore, it is critical to research the fatigue crack behaviour in FDM structures. This behaviour is mainly responsible for the change of structural stiffness and hence can influence the dynamic response of the structure under the mentioned loads. The measurement of the structural dynamic response can give us an idea of the severity due to crack growth in an in-situ manner. This thesis mainly aims to investigate the dynamic response of the cracked FDM structures under thermo-mechanical loads. The relationship between the coupled loads, crack propagation and dynamic response is developed analytically and later validated experimentally. This research has improved the existing torsional spring model, which can represent the crack depth more accurately and hence estimated the fundamental frequency of the selected structure with an up to around 20% to 120% reduced error in the case of deep cracks. Furthermore, the analytical relationship between the structural displacement amplitude and crack depth and location was modelled for the very first time in the presence of the crack breathing effect. Extensive experimentation is performed to validate the developed analytical relationship and its related theory. The fatigue crack growth of FDM ABS beams under thermo-mechanical loads with varying printing parameters is also investigated. The optimal printing parameters combination (X raster orientaion, 0.8 mm nozzle size, 0.15 mm layer thickness) is determined. The underlying reasons behind the experimental data are analysed. The outcome of this optimisation can help manufacturers to print long-life and crack resistant printed structures.

Keywords: Fused Deposition Modelling; ABS; Fatigue; Crack Growth; Dynamic Response; Thermo-mechanical loads

ACKNOWLEDGEMENTS

First and foremost, I am deeply grateful to my supervisor Dr Muhammad Khan for his invaluable supervision, advice, support and patience during my PhD study. His immense knowledge and plentiful experience encouraged me in all the time of not only my academic research but also my daily life. I would not have been able to complete my PhD without his tutelage and encouragement throughout the three years of my PhD.

I would also like to thank my associate supervisor Prof Andrew Starr for his help and guidance on my study. I am also truly grateful to Dr Isidro Durazo Cardenas and Dr David Ayre for their kind laboratory equipment support and invaluable technical support in my study. My heartfelt thanks are also due to Prof Vijay Kumar Thakur for generously taking his time and attention in carefully reading and commenting on my work. Additionally, I would like to thank Dr Pavan Addepalli and all the colleagues in the B30 lab for their kind help and a cherished time spent together in the lab.

Many thanks to my parents for their continued support and understanding of a far away from home son. I would also like to express my gratitude to my beloved wife, Junyao Li. Her selfless care and devotion to our family allowed me to focus on my study. A very special thank you also to my lovely son Lvyan He. As a cute baby, his laugh deeply encouraged me and relaxed me when I felt stressed out.

My appreciation also goes out to my dear friends for their encouragement. Their kind help and support have made my study and life in the UK a wonderful time.

LIST OF PUBLICATION

1. He, F., Kumar, V. and Khan, M.A. (2020) 'Evolution and New Horizons in Modelling Crack Mechanics of Polymeric Structures', Materials Today Chemistry

2. He, F., Khan, M.A. and Zai, B.A. (2019) 'Material mechanics of crack growth in structural dynamics', Procedia Structural Integrity, 17 Elsevier B.V., pp. 72–79.

3. Baqasah, H., He, F., Zai, B.A., Asif, M., Khan, K.A., Thakur, V.K. and Khan, M.A. (2019) 'In-situ dynamic response measurement for damage quantification of 3D printed ABS cantilever beam under thermomechanical load', Polymers, 11(12)

4. He, F. and Khan, M. (2021) 'Effects of Printing Parameters on the Fatigue Behaviour of 3D-Printed ABS under Dynamic Thermo-Mechanical Loads', Polymers, 13(14), p. 2362.

5. He, F., Alshammari, Y.L.A and Khan, M.A. (2021) 'The Effect of Printing Parameters on Crack Growth Rate of FDM ABS Cantilever Beam under Thermo-mechanical Loads', Procedia Structural Integrity

6. Fleet, T., Kamei, K., He, F., Khan, M.A., Khan, K.A. and Starr, A. (2020) 'A machine learning approach to model interdependencies between dynamic response and crack propagation', Sensors (Switzerland), 20(23), pp. 1–13.

TABLE OF CONTENTS

LIST OF FIGURES

LIST OF TABLES

LIST OF EQUATIONS

LIST OF ABBREVIATIONS

ABS   Acrylonitrile Butadiene Styrene

CNT   carbon nanotube

COS   crack onset strain

CPVC   Chlorinated polyvinyl chloride

CT   Compact tension

FCG   Fatigue Crack Growth

FDM   Fused Deposition Modelling

LEFM   Linear elastic fracture mechanics

PA   Polyamide

PC   Polycarbonate

PEEK   Polyether ether ketone

PLA   Polylactic acid

PMMA   Poly methyl methacrylate

PP   Polypropylene

PS   Polystyrene

PSF   poly bisphenol-A sulfone

PVC   Polyvinyl chloride

PVF2   polyvinylidene fluoride

rCFRP   recycled short carbon fibre reinforced plastic

SIF   Stress Intensity Factor

UHMWPE Ultrahigh molecular weight polyethene

NOMENCLATURE

a	Crack depth
α_T	Loss factor $\tan\delta$
A	Beam section
A_L, A_R	Coefficients
b	Beam width
B	Coefficient
B_L, B_R	Coefficients
c	Damping
C_L, C_R	Coefficients
D_L, D_R	Coefficients
E	Elastic modulus
E_0	Elastic modulus at T_0
E^*	Complex elastic modulus
E'	Storage modulus
E''	Loss modulus
f	Frequency
$f_r(a/H)$	Shape function
H	Beam thickness
I	Area moment of inertia
J_z	Momentum of inertia
k	Torsional spring stiffness

l	Distance between the crack location and fixed end of the beam
L	Beam length
m	End mass
m_{acc}	Accelerometer mass
ω	Angular frequency
ω_s	Angular frequency of a shaker
$q_n(t)$	Modal coordinate of the n-th mode
ρ	Density
t	Time
$T(t)$	Modal coordinate
$u(t)$	Shaker displacement
U_0	Shaker displacement amplitude
U_{max}	Beam displacement amplitude
$U_{max,modified}$	Modified beam displacement amplitude
$U(x,t)$	Beam total displacement
x	Distance to the fixed end of the beam
$y(x,t)$	Beam displacement due to bending
$y_L(x,t)$	Fixed end side beam displacement
$y_R(x,t)$	Free end side beam displacement
$Y(x,t)$	Mode shape of the beam
$Y_n(x)$	n-th mode shape of the beam

1 IDENTIFICATION AND SIGNIFICANCE OF THE RESEARCH PROBLEM

1.1 Research Background

The rapid development of 3D printing technology over the last 30 years has led to an increasing number of 3D printed products being used in a wide range of industries. These include FDM products made from polymeric raw materials. These products have great potential to be used in structural applications under multiple loading conditions.

The multiple complex loads, such as temperature and mechanical loads combine, is a critical challenge to the integrity of the FDM structure. Prolonged thermo-mechanical cyclic stress has a high risk of causing structural fatigue. Fatigue damage causes cracks and eventual fracture of the structure, resulting in catastrophic failure. Therefore, it is significant to monitor the structural damage during a continuous running state without dismantling the structure. The structural dynamic response, on the other hand, is a good reflection of structural integrity. They are also affected by the couple loads to which the structure was subjected in real-time. In addition, as an advantage, the dynamic response can be easily measured in-situ even if the FDM structure continues in operation. This thesis attempts to investigate the effectiveness of measuring in-situ dynamic response to estimate the structural integrity under applied thermo-mechanical loads.

1.2 Research Problem

The research problem can be summarised as the investigation to determine the effectiveness of in-situ dynamic response measurement for estimating the structural integrity under applied coupled loads for FDM printed structures. However, to understand the theory and fundamentals, it is essential to use an analytical approach to determine the relationship between the dynamic response, structural integrity, and coupled loads. Later, this can be validated using an empirical study where the response can be measured in an in-situ

manner. It is also anticipated that the printing parameters of an FDM structure can produce a critical impact on the structural integrity estimation. Hence, the influence of these parameters on the structural properties, such as crack growth resistance, is also required to be evaluated.

1.3 Research Methodology

According to the summarised research problem in Section 1.2, the thesis proposed a suitable research methodology. The steps of the research are shown in Figure 1-1. The relationship between thermo-mechanical loads, structural integrity in terms of crack growth or resistance and dynamic response is analytically modelled. The classical torsional spring model is modified to improve the estimation of the fundamental structural frequency. Further, to make the model workable for an in-situ response comparison, the displacement response of a beam in the presence of a seeded crack is also analytically modelled with special consideration of the crack breathing effect.
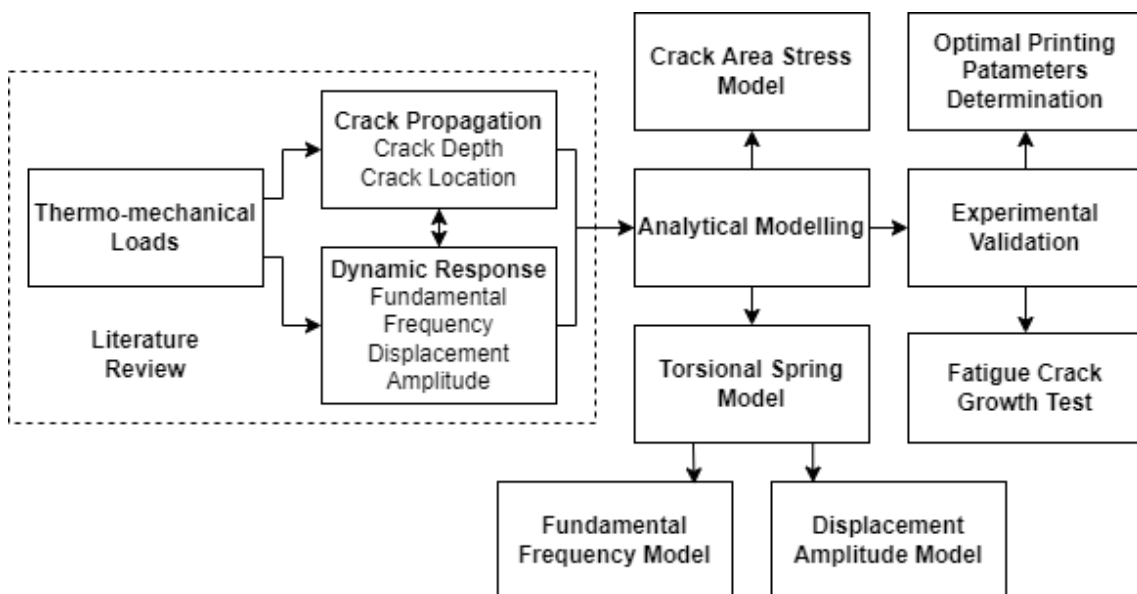
Figure 1-1 Research steps

The experimental validation for the proposed models is performed. The experiment measures the dynamic response of the beams with the propagating crack depth at different crack locations under different temperatures. The fundamental frequency of the beam with the initial seeded crack is measured by

2

impact tests. Then the beam is excited under the first mode resonance for the measurement of the displacement amplitude. The initial seeded crack propagates during the resonance and changes the structural dynamic response. The new fundamental frequency of the beam is measured again. The beam is then vibrated under the resonance with the new fundamental frequency. The corresponding displacement amplitude is recorded, too. The above steps are repeated until the beam fracture. A digital microscope measures the crack depth during the process. The collected dynamic response and crack depth data in the tests are compared with analytical models for validation.

The effect of printing parameters on the structural dynamic response and crack growth resistance is also investigated in the experiments. Three printing parameters (raster orientation, nozzle size and layer thickness) are analysed in the test. Three values, which cover the typical range of printing settings, are evaluated for each parameter under three different temperatures. The fatigue life of the beam is measured and compared in order to determine the optimal parameter combination.

1.4 Research Objectives

1. Evaluate the relationship between the crack severity and structural dynamic response for 3D-printed ABS cantilever beam at elevated temperatures.
   1.1. Develop the analytical model for the relationship between the crack size/location and structural fundamental frequency.
   1.2. Develop the analytical model for the relationship between the crack size/location and structural displacement amplitude.
2. Evaluate the relationship between the crack tip loading and structural dynamic response.
3. Develop the experiments and data post-process method for dynamic fatigue test to validate the analytical model.
4. Evaluate the dynamic fatigue life for 3D printed ABS and determine the optimal 3D printing parameter combination under dynamic thermo-mechanical loads.

1.5 Thesis Structure

Chapter 2 provides a comprehensive review of the crack propagation of FDM structure under thermo-mechanical loads. It addresses the research gap for crack growth under dynamic coupled loads. The analytical modelling between dynamic response and crack propagation is proposed in Chapters 3 and 4. Chapter 5 presents the analytical relation between the dynamic response and thermo-mechanical loads. The experimental work for model validation is provided in Chapter 6. The discussion on model validation is given in Chapter 7. The discussion on the optimisation of printing parameters and their effect on fatigue crack growth is provided in Chapter 8. Finally, Chapter 9 summarises the conclusions of the thesis.

2 LITERATURE REVIEW

The manufacturing industry uses a variety of materials to fabricate parts and structures. From the wooden structure of the building to the metal crankshaft of the engine, one can observe the development of numerous types of materials throughout history. The most prominent materials are made of either wood, ceramics, metals or polymers (Stein, 1994). Out of these prominent ones, the use of polymers has increased immensely in the past few decades. Polymers have become a high-quality choice suitable for structural applications because of the low cost and lightweight features such as wind blades and Unmanned Aeriel Vehicle (UAV) wings (Odahara, 2012)(Ning et al., 2015).

Different manufacturing processes for polymeric structures have been developed in order to satisfy the increasing industrial demand. These processes include different types of moulding (such as injection, rotation and blow), extrusion, vacuum forming, polymer casting and 3D printing. These can be further categorised into two types: Conventional Manufacturing and AM. Conventional Manufacturing parts have been widely used in mass production industries. However, compared with it, the rapid development in AM has attracted more attention from academia and industry (Gao et al., 2015). Primarily, 3D printing AM provides many advantages, including customisation

freedom, cost-effectiveness and less waste production. So it has been applied to fabricate polymeric components and structures for the applications used in aerospace, automotive, medical and biomechanical sectors (Ning et al., 2015) (Zein et al., 2002) (Long et al., 2017). Due to its specific advantage to create highly customised plastic part designs or prototypes, the medical industries apply it to create prosthetics and implants.

No matter how the structures are fabricated, they work under a complex and harsh working environment, such as the pressure sensors and sensor pads, as shown in **Figure 2-1** (Odahara, 2012) (Leigh et al., 2012). These polymeric structures may experience various damages due to fatigue, corrosion, impact and puncture (Naebe et al., 2016). Although the research has also observed possibilities of damages due to chemical and environmental conditions (Baker, Jones and Callinan, 1985), most of the past research focused on cracks and damages, which were primarily due to mechanical loads (Naebe et al., 2016). They described the mechanics of how cracks initiate and propagate in real applications under mechanical loads. However, understanding the crack propagation behaviour for such loading conditions is more significant because the coupled thermo-mechanical load is more common in an actual working environment (He, Khan and Zai, 2019). The previously published work mostly considered time-independent or quasi-static load conditions while characterising crack behaviour (Safai et al., 2019).

In contrast, the fracture theory also suggests that the load range and frequency could lead to a different crack propagation phenomenon. The modelling of the relationship between these load conditions and crack propagation is helpful to predict the potential structural failure. The load history can calculate the real-time crack state, thereby estimating fatigue life and avoiding the final failure. Therefore, it is essential to understand the crack growth behaviour for polymeric structures under dynamic loads to predict and prevent their fracture.
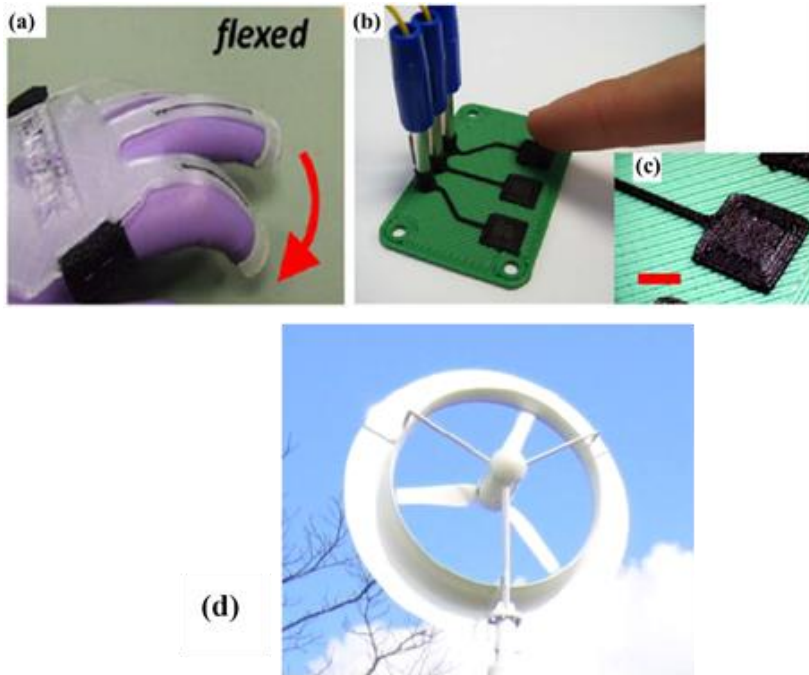
Figure 2-1 Several 3D printed polymers applications (a) Piezoresistive sensors (b) Capacitive sensors (c) Sensor pads (scale bar 5 mm) (Leigh et al., 2012) (d) Wind-lens turbine (Odahara, 2012)

In contrast to the conventional manufactured polymeric structures, crack propagation in 3D printing polymeric structures is more complicated. Because there are significant differences in microstructure due to these two manufacturing methods. Apart from load range and frequency, a variety of 3D printing parameters may affect the rupturing of the parts. The relationship between these parameters and potential crack growth properties is significant to understanding the damage evolution in printed parts.

Extensive research articles and reviews have explained the phenomenon and significance of the crack growth behaviour of polymeric structures. However, when reviewing these studies critically, a comprehensive effort is still required to emphasise the effect of thermo-mechanical couple loads on crack propagation. Therefore, Chapter 2 compiles all this previous research and considers the influence of thermo-mechanical loads on crack growth. It has been found that the actual crack growth phenomenon for real applications is different from the previous research and their conclusions. Therefore, an analytical and empirical

study about the crack propagation of polymeric structures under the dynamic thermo-mechanical loads can be a novel contribution in the fracture area.
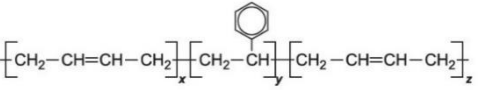
A brief overview of the main polymers applied in conventional manufacturing and 3D printing will be described in Section 2.1. Because as the raw material of the structure, their mechanical properties will potentially affect the crack propagation in polymeric structures.
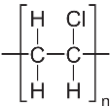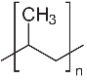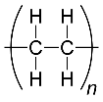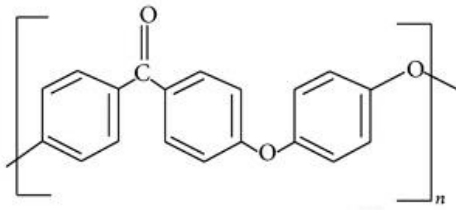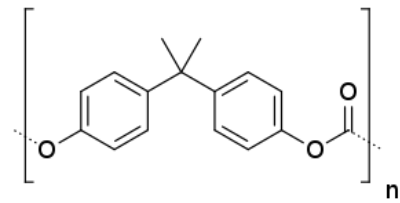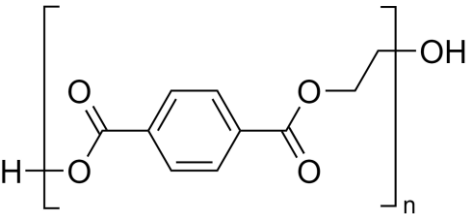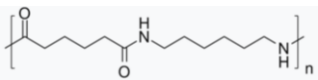
2.1 Major Polymers Used in Industries

Most polymers described in Chapter 2 are plastic materials. They are widely used in industries due to their excellent plasticity, which means they can be moulded or shaped easily. Generally, plastics also have other excellent properties such as high strength-to-weight ratio, low thermal conductivity and low electrical conductivity. These benefits allow plastics to be used in various industries (Andrady and Neal, 2009). These plastics can be divided between thermoplastics and thermosets polymers. Specifically, thermoplastic polymers are introduced below because this thesis focuses on 3D printing polymers. **Table 2-1** lists the main commercially employed polymers and their properties.

Fundamentals about crack growth will be described in Section 2.2. These fundamentals are the cornerstones of advanced research. The author believes that reviewing current advances in fracture of materials is incomplete without briefly discussing them.

Table 2-1 Main polymers structures and mechanical properties

Materials	Chemical Structure	Tensile Modulus (MPa)	Flexural Modulus (MPa)
Acrylonitrile butadiene styrene (ABS) buta-1,3-diene;prop-2-enenitrile;styrene		2027	2096

Polyvinyl chloride (PVC) poly(1-chloroethylene)		2834	3316
Polypropylene(PP) Poly(1-methylethylene)		-	1551
High-density polyethylene (HDPE)		-	1379
Polyether ether ketone (PEEK) poly(oxy-1,4-phenyene-oxy-1, 4-phenyene)		3378	4068
Polycarbonate (PC) 4-[2-(4-hydroxyphenyl)propan-2-yl]phenol		2379	2379
Polyethylene terephthalate (PET) Poly(ethyl benzene-1,4-dicarboxylate)		2758	2758
Nylon 66 Poly[imino(1,6-dioxohexamethylene) iminohexamethylene]		3241	2827

2.2 Fundamentals of Crack Growth in a Structure

Crack propagation starts soon after the crack birth at the microscale under the influence of the applied load. Significant cyclic loads lead this crack to a macroscale in the form of visible damage (Sauer and Richardson, 1980). These

repetitive loads generate various stress conditions surrounding the crack tip, which promote cracks propagate up to failure. Therefore, it is significant to understand the relation between the crack tip's stress and the FCG rate. Published research theoretically correlated these two parameters and demonstrated their interdependencies with different material properties and load conditions (Radon and Culver, 1975a). Brief details about these parameters are provided in Section 2.2.1.

2.2.1 Stress Condition at Crack Tip

In 1898, Kirsch proposed the linear elastic solution for stress conditions surrounding a hole in an infinite plate (Kirsch, 1898), as shown in Equation **(2-1)** to **(2-3)**. The hole has radius r, and the polar coordinates are r and θ. Where σ_∞ is uniaxial tension stress, σ_{rr} and $\sigma_{\theta\theta}$ are the stresses along the radial and circumferential directions and $\tau_{r\theta}$ is the shear stress.

$$\sigma_{rr} = \frac{\sigma_\infty}{2}\left[1 - \left(\frac{a}{r}\right)^2\right] + \frac{\sigma_\infty}{2}\left[1 - 4\left(\frac{a}{r}\right)^2 + 3\left(\frac{a}{r}\right)^4\right]\cos(2\theta) \tag{2-1}$$

$$\sigma_{\theta\theta} = \frac{\sigma_\infty}{2}\left[1 + \left(\frac{a}{r}\right)^2\right] - \frac{\sigma_\infty}{2}\left[1 + 3\left(\frac{a}{r}\right)^4\right]\cos(2\theta) \tag{2-2}$$

$$\tau_{r\theta} = -\frac{\sigma_\infty}{2}\left[1 + 2\left(\frac{a}{r}\right)^2 - 3\left(\frac{a}{r}\right)^4\right]\sin(2\theta) \tag{2-3}$$

The above equations can only provide stresses on a circular hole and limit any other crack geometry application. Later in 1913, Inglis proposed the solution for the stress field surrounding an ellipse and overcame the geometry-based limitation. It was the crucial next step in developing linear elastic fracture mechanics (LEFM) theory (Inglis, 1913). Similar to Kirsch's solution for the circular hole, Inglis used an infinite isotropic plate in uniaxial tension for his model. However, due to elliptical geometry, his model applied to an infinite number of different scenarios by changing the values of major and minor axes. His solution proposed that the maximum stress σ_{max} is $\sigma_\infty\left(1 + 2\frac{a}{b}\right)$. Where a and b were the half width and heigrht of ellipse, respectively.

In 1939, Westergaard developed the exact solution for the stress surrounding the crack plane. It had two advantages over Inglis's solution. Firstly, Westergaard's solution provided stresses on general crack geometry and not on an ellipse. Secondly, the stresses can be obtained in rectangular coordinates that were easy to understand compared to the elliptical ones. The stress expression at any locations around the crack tip is shown in Equation **(2-4)**,

$$Z(z) = \frac{\sigma_\infty}{\sqrt{1 - \left(\frac{a}{z}\right)^2}} \qquad\qquad \textbf{(2-4)}$$

Where $Z(z)$ is the complex numbers for the stress solution at any point, σ_∞ is the static stress applied on the structure, a is the crack length, z equals $x + iy$ as the position of the point (Westergaard, 1939). A Taylor series expansion of equation **(2-4)** was essential to calculate the stress around the crack by dividing it into its real and imaginary parts. The imaginary part made the solution complex to understand the stress state surrounding a crack. Irwin resolved this complexity and proposed the definition of stress intensity factor (SIF) K as a near-crack-tip approximation in 1957. He greatly simplified Westergaard's result to an approximate solution in the area closely near the crack tip, as shown in Equation **(2-5)** to **(2-7)**(Irwin, 1957).

$$\sigma_{xx} = \frac{\sigma_\infty \sqrt{\pi a}}{\sqrt{2\pi r}} \cos\frac{\theta}{2}\left(1 - \sin\frac{\theta}{2}\sin\frac{3\theta}{2}\right) \qquad\qquad \textbf{(2-5)}$$

$$\sigma_{yy} = \frac{\sigma_\infty \sqrt{\pi a}}{\sqrt{2\pi r}} \cos\frac{\theta}{2}\left(1 + \sin\frac{\theta}{2}\sin\frac{3\theta}{2}\right) \qquad\qquad \textbf{(2-6)}$$

$$\tau_{xy} = \frac{\sigma_\infty \sqrt{\pi a}}{\sqrt{2\pi r}} \cos\frac{\theta}{2}\sin\frac{\theta}{2}\cos\frac{3\theta}{2} \qquad\qquad \textbf{(2-7)}$$

Where σ_{xx} and σ_{yy} are the stresses along with two axis directions, τ_{xy} is the shear stress, r/θ are polar coordinates of the location near the tip. Irwin replaced $z = x + iy$ in Westergaard's solution by $z = a + re^{i\theta}$. Then Irwin simplified the equation in the following algebraic calculation based on the inequality $r \ll a$. He also applied the polar coordinates to simplify the calculation

by Euler's identity rather than the Taylor series expansion. These simplifications led to the final stress was calculated accurately only near the crack tip, as shown in **Figure 2-2**.
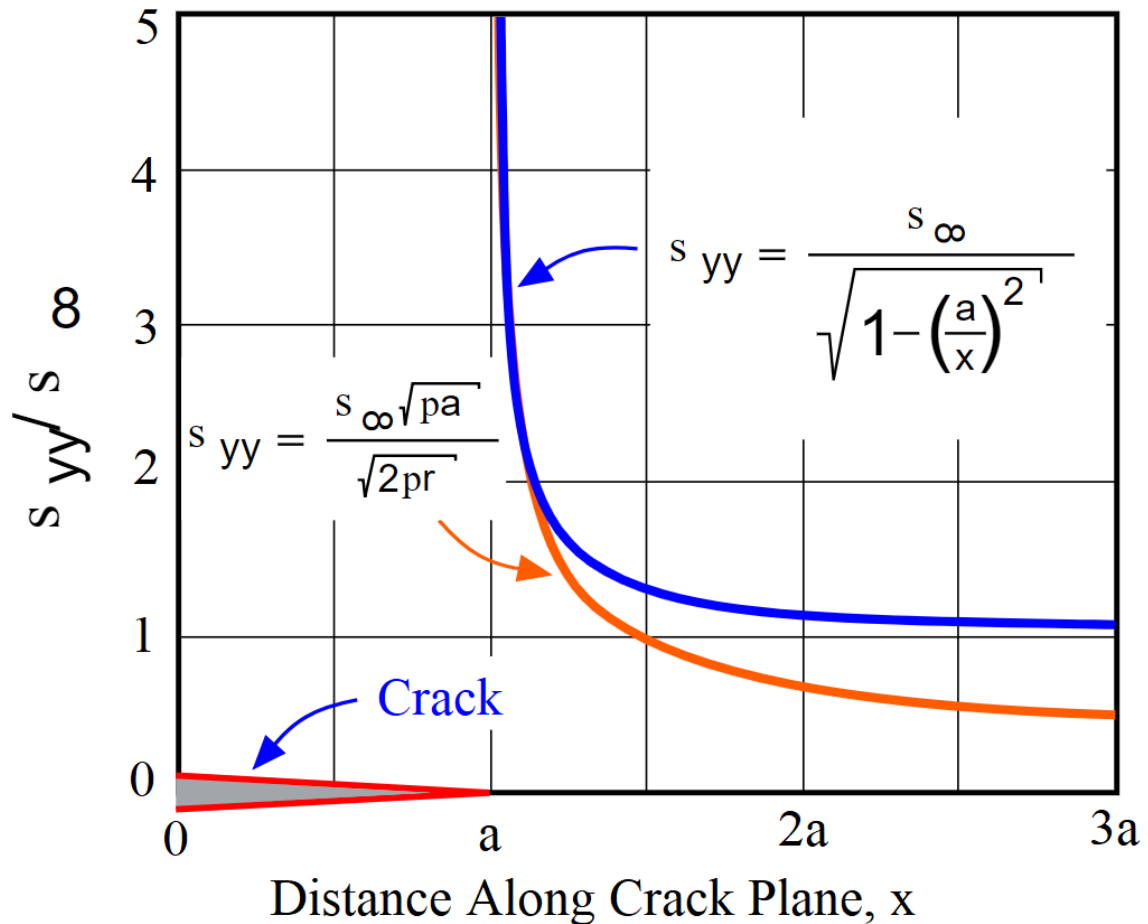
Figure 2-2 Stress modelling near crack tip (McGinty, n.d.)

There are the same expression $\sigma_\infty \sqrt{\pi a}$ in Equation **(2-5)** to **(2-7)**. The expression of σ_∞ and a fully represents the stress condition around the crack tip. Irwin first recognised this as SIF, which causes the different cracks to initiate and propagate as the various stress state at a crack tip (Irwin, 1957).

2.2.2 Modelling of Stress Condition and Crack Propagation

A large amount of research used above approximate stress solutions at crack tip to develop the analytical relations about crack growth. Most of them aimed to link the stress condition to the crack growth rate. Paris, Gomez and Anderson used Irwin's research to introduce the idea that the FCG rate was strongly

dependent on the SIF. The reason was due to the maximum SIF K_{max} and SIF range ΔK give both the intensity and variation of loading and geometry (Paris, Gomez and Anderson, 1961). They proposed the famous Paris' Law as an empirical crack growth rate equation **(2-8)**. It showed the relationships between the SIF range and subcritical FCG in a specific fatigue life stage (Paris and Erdogan, 1963).

$$\frac{da}{dN} = C(\Delta K)^m \qquad \textbf{(2-8)}$$

Where $\frac{da}{dN}$ is the FCG rate, C and m are parameters determined by the materials, environmental conditions and stress ratio, and ΔK is the range of the SIF during the fatigue cycle. SIF in Equation **(2-8)** is defined as a parameter based on the static loads. The range of SIF cannot represent the dynamic loads. Radon further simplified this relationship, as shown in Equation **(2-9)**,

$$\frac{da}{dN} = F\emptyset^\alpha \qquad \textbf{(2-9)}$$

where $\emptyset$ is a function about the SIF. F and α are two coefficients. Radon also pointed out that a single analytical da/dN "law" cannot appropriately reflect the crack propagation characteristics. The formula can only partially represent regression values of the data derived from a huge amount of tests due to the influence of the experimental environment. Essentially, this crack growth rate model is based on semi-analytical methods, so the coefficients F and α are dependent on the experimental setup (Radon, 1980). Despite all the limitations, which we have discussed above, much research has used this formulation for estimating the crack growth in polymers.

2.3 Crack Propagation of Polymeric Structures under Mechanical Loads

Irwin and Paris's results were commonly applied to investigate the crack growth in polymeric structures (Bretz, Hertzberg and Manson, 1981)(Michel, Manson and Hertzberg, 1984). Odahara performed the FCG test of a wind-lens blade manufactured with Dicyclopentadiene material. The relationship between FCG

rate and ΔK was obtained as the format of Paris Law, as shown in Equation **(2-10)** and **Figure 2-3** (Odahara, 2012).
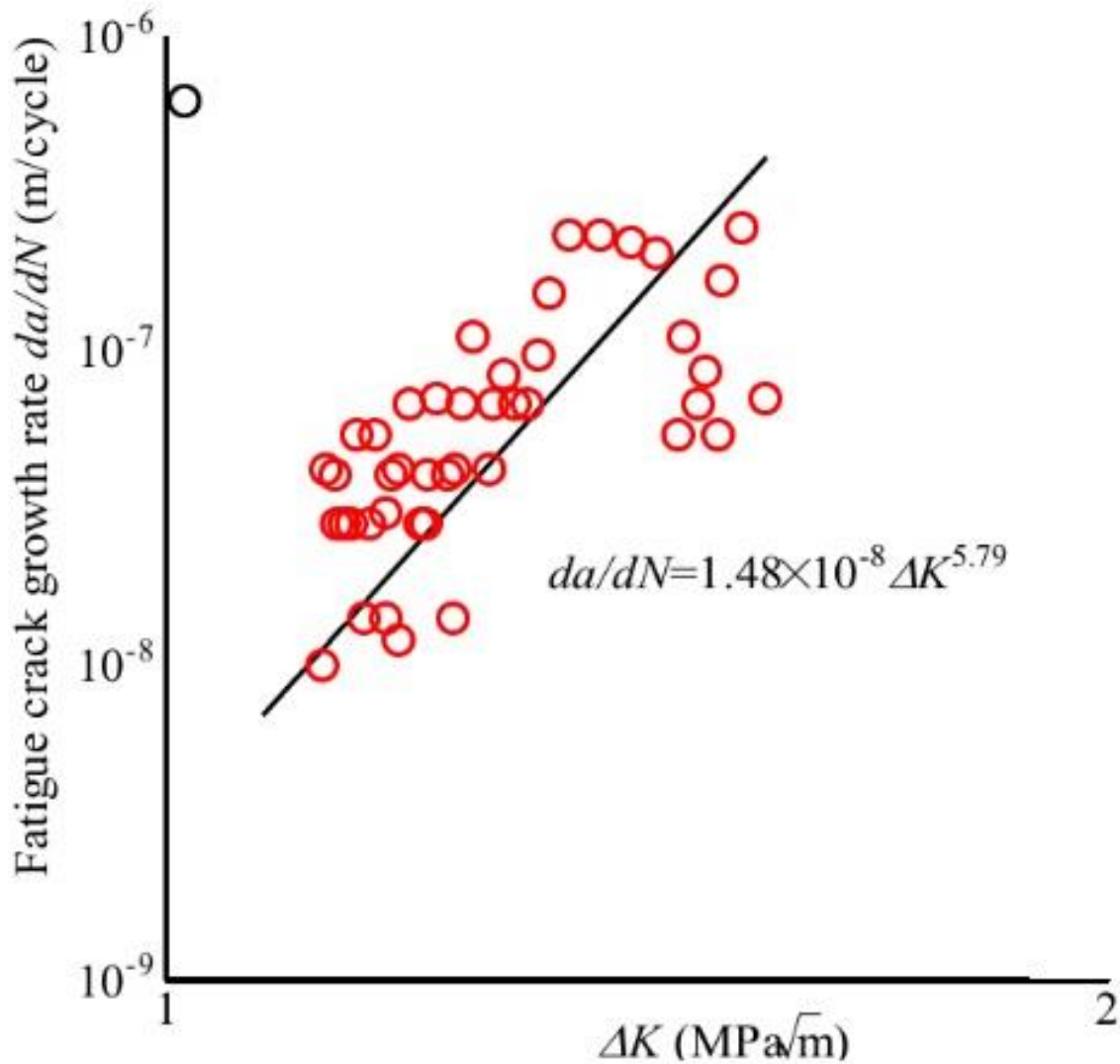
Figure 2-3 da/dN - ΔK relation of Dicyclopentadiene material (replotted) (1 mm initial crack depth, 1.1 to 1.5 ΔK range, 4.5MPa stress amplitude, 5.5MPa average stress, stress ratio R = 0.1 and 2Hz cycle frequency) (Odahara, 2012)

$$\frac{da}{dN} = 1.48 \times 10^{-8} \Delta K^{5.79} \tag{2-10}$$

Suyitno and Lazuardi analysed how the load ratio R can affect the FCG rate in UHMWPE. They carried out experiments with CT specimens. The experimental results showed that higher load ratio R increased the fatigue crack propagation

resistance, which resulted in the lower FCG rate, as shown in **Figure 2-4**. (Suyitno and Pujilaksono, 2017)
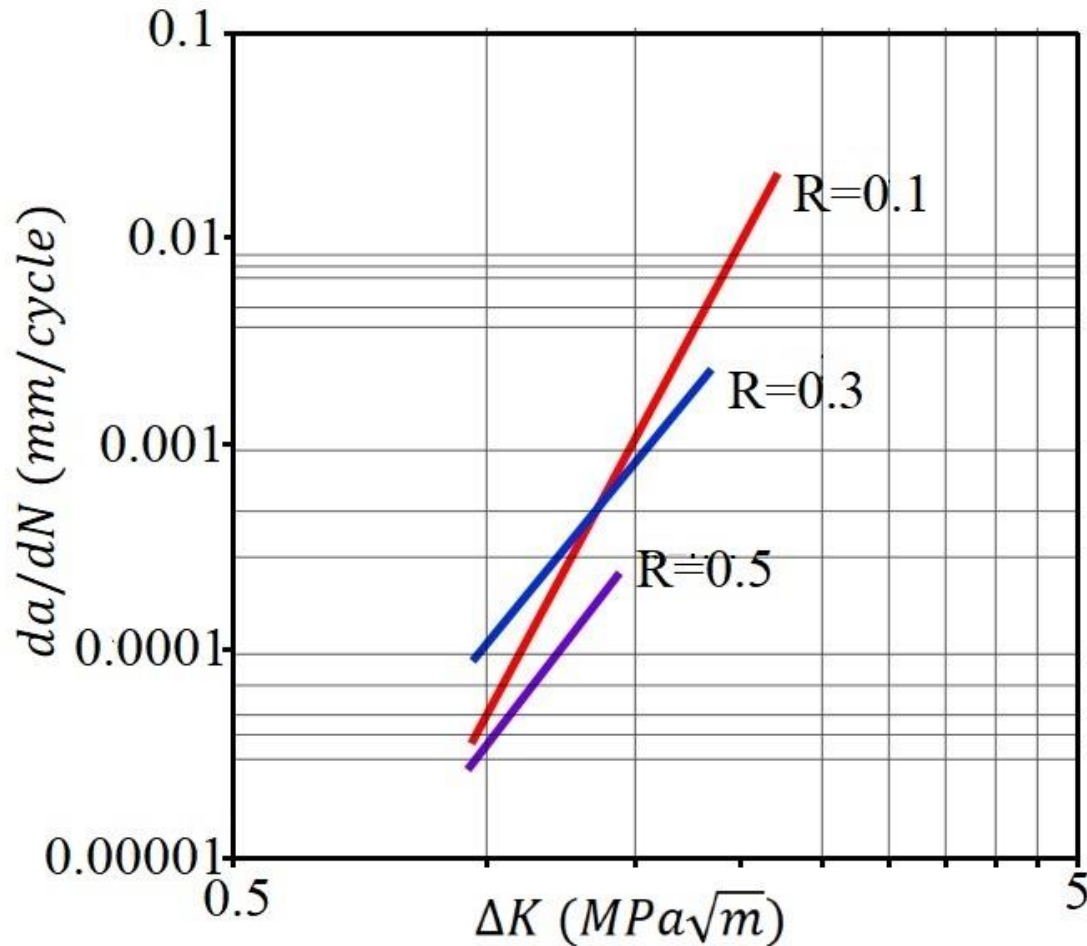
Figure 2-4 Effect of load ratio on fatigue crack behaviour of PE (replotted) (fully tensile cyclic loading with a constant amplitude of 630N and a constant loading frequency of 10 Hz) (Suyitno and Pujilaksono, 2017)

Li et al. carried out several related studies about the crack propagation in plastic alloys. They experimentally investigated the mixed-mode fracture toughness for PC and ABS alloy (Li et al., 2015). In another research, Fang, Li and Wang (Fang, Li and Wang, 2007) compared the FCG rate in PC and PC/ABS alloy experimentally. A 3Hz cyclic tensile load with a 0.1 load ratio was applied to a compact tension specimen. The test data demonstrated that PC/ABS alloy had a higher crack growth resistance than PC at the same SIF range. The crack growth rate in the PC specimen was three times that of PC/ABS alloy because

of the larger plastic zone near the crack tip in PC/ABS alloy compared with PC. The research also formulated the Paris' Law for PC/ABS alloy under 3Hz fatigue load as shown in Equation **(2-11)**,

$$\frac{da}{dN} = 9.5587 \times 10^{-5} (\varDelta K)^{2.88381} \tag{2-11}$$

However, in another research, they formulated another Paris Law (Equation **(2-12)**) for the FCG rate of PC/ABS alloy with 3Hz loads on account of the overload effects (Fang, Wang and Li, 2007).

$$\frac{da}{dN} = 1.166 \times 10^{-4} (\varDelta K)^{2.77} \tag{2-12}$$

The above empirical equations explain that the application of Paris law has to consider many parameters, including loading conditions. Its applicability is not as extensive as the analytical models.

Apart from crack propagation, the effects of some other crack properties are also investigated using the Paris Law. Okayasu et al. investigated the crack growth characteristics of a rCFRP from LEFM formulations (Okayasu et al., 2013). The work on effort proposed that the Paris Law relations for polymer, especially in slow growth rate regimes, were affected by severe crack closure. Same observations were reported for other polymeric materials (PVC, PMMA and PA) (Shirashi, Ogiyama and Tsukuda, 1997). Mazidi et al. used LEFM to investigated fracture properties of ABS. They evaluated the influence of crack scale and rubber amount on the microscopic failures and estimated macroscopic crack propagation behaviour of the specimens as given in Equation **(2-13)** (Mazidi, Aghjeh and Abbasi, 2012)(Mazidi, Aghjeh and Abbasi, 2013).

$$\frac{da}{dN} = 1.48 \times 10^{-8} \Delta K^{5.79} \tag{2-13}$$

Few amounts of research used a numerical approach to estimate crack growth. The lack of representative numerical models for crack growth in polymers causes difficulties in crack propagation prediction even under controlled stress

15

conditions. Critical phenomena such as crack closure and plastic zone influence crack growth with a too complicated mode, making it challenging to develop a perfect numerical model even with some appropriate assumptions (Khan, Cooper and Starr, 2009; Zai et al., 2019a, 2020b). Ding et al. (Ding, Karlsson and Santare, 2017) developed a numerical method to estimate the FCG rate for polymers. They assumed that the crack propagation is related to the 'dissipated energy in the plastic zone' surrounding the crack tip. They formulated the FCG rate as shown in Equation **(2-14)**.

$$\frac{da}{dN} = \frac{dW_p/dN}{\left(dW_p/da\right)_{cr}} \tag{2-14}$$

Where dW_p/dN is 'the accumulation rate of plastically dissipated energy, determined from numerical model'. $\left(dW_p/da\right)_{cr}$ is 'the critical value of plastically dissipated energy required per incremental increase in crack length' as a material property and represented Paris Law with a practical or physical meaning rather than an empirical model. The value of $\left(dW_p/da\right)_{cr}$ was determined through the experiment with Equation **(2-15)**,

$$\left(dW_p/da\right)_{cr} = \frac{\left(dW_p/dN\right)_{sim}}{(da/dN)_{exp}} \tag{2-15}$$

They simulated the crack growth rate for PC, PS and Nylon 66 under different loading frequencies and estimated the parameters of Paris law well in agreement with experimental results (Ding, Karlsson and Santare, 2017).

The above research all modelled the crack propagation in polymers according to Paris Law. However, a large amount of research just carried out the experimental work and explained the crack propagation in real polymeric applications without taking help from Paris law. A description of a few prominent investigations is provided below (Mars and Fatemi, 2002)(Marco et al., 2017).

Some research focused on applying PEEK polymer (Brillhart and Botsis, 1994; Sadeghi et al., 2009; Saib, Evans and Isaac, 1993). Koike et al. investigated the failure mechanism of polymeric bearings made with PEEK in an underwater

environment. They conducted the rolling contact fatigue test for studying and observing the crack propagation on the inner ring of the bearing, as shown in **Figure 2-5**. There were mainly three types of cracks, semi-circular, surface and subsurface cracks. The observation showed that the main surface and subsurface cracks propagation directions were the same as the bearing rolls. The rolling aluminium balls applied the shear stress and then led to the main subsurface cracks propagation from the artificial notch. As for the semi-circular cracks, the tensile stress resulted in it on the raceway surface, as shown in **Figure 2-6** (Koike et al., 2012).

Similarly, some research also focused on the rolling fatigue crack propagation in polymer bearings (Fan, Keer and Cheng, 1993; Itakura et al., 2013; Koike, Honda and Kida, 2011; Oyama et al., 2012, 2013). Shi, Kida and Kashima observed the surface crack of polyphenylene sulphide (PPS) polymer thrust bearings under water. The flaking from the defects occurred on the track surface (**Figure 2-7**). This observation indicated that the propagation and connections of the surface cracks caused flaking and final failure of the bearing (Shi et al., 2014)(Shi et al., 2016).

2.4 Crack Propagation of Polymers under Thermo-mechanical Loads

The polymeric structures in practical applications are worked under more complex load conditions (Odahara, 2012). A coupled thermo-mechanical load condition is usually observed in critical applications, which significantly affects the crack propagation in polymers quite differently than the single load condition, as discussed in Section 2.3 (Leigh et al., 2012). Couple loads such as cyclic strain with relatively high-temperature values allow a crack to propagate but makes its behaviour more dependent on properties like damping, viscoelasticity and thermal conductivity (Safai et al., 2019). An increase in temperature decreases the structural stiffness. The specimen deforms, and deflection occurs due to the stiffness loss. These mechanical properties change affects the fracture roughness and then change the FCG behaviour when applied the mechanical loads.

17
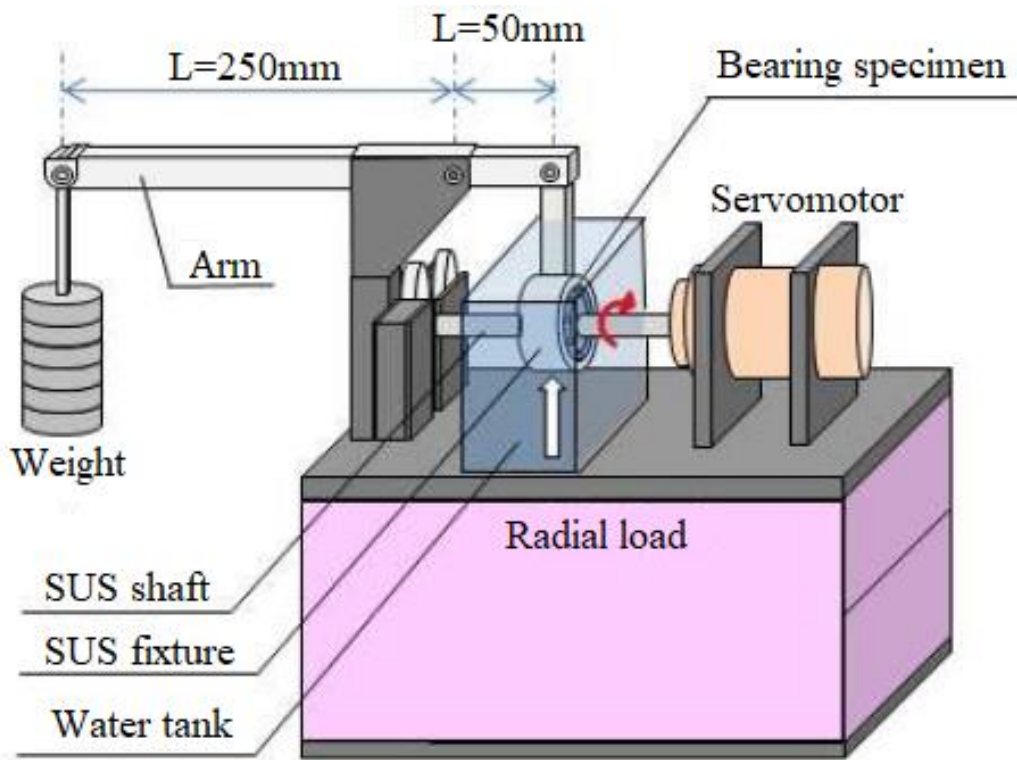
Figure 2-5 RCF test machine scheme (Koike et al., 2012)
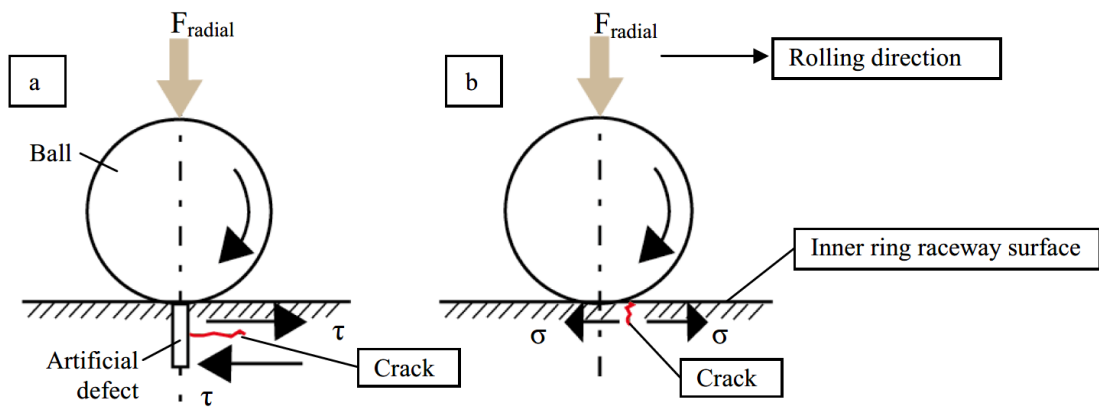
Figure 2-6 Two different crack types and associated growth directions: (a) subsurface cracks, (b) semi-circular cracks(Koike et al., 2012)
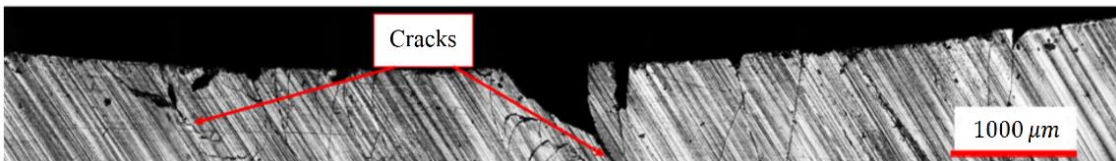
Figure 2-7 Crack observation in cross-section of the top race track (Shi et al., 2014)

Section 2.4 reviews the efforts related to crack propagation in polymers under different temperature conditions, different load frequencies and combination of temperature and mechanical loads. Moreover, some other influence parameters such as the overloaded condition and geometry of polymeric structures are also described.

2.4.1 Temperature Effect on Crack Propagation

Many investigations proposed that FCG rate can be affected by environmental temperature (Brillhart and Botsis, 1992; Irfan-ul-Haq and Merah, 2003; Iwamoto, Jinen and Suzuki, 1988; Khan et al., 2015, 2018; Merah, Irfan-Ul-Haq and Khan, 2004; Ruellan et al., 2019; Wann, Martin and Gerberich, 1976). Different polymeric materials have been tested at a range of temperatures, as shown in **Table 2-2**. The testing temperatures in most cases were set below 100°C because of the lower polymeric glass transition temperatures.

Waller et al. (Waller et al., 2011) investigated the crack onset strain (COS) for brittle coatings on polymer substrates considering temperature influence. The research proposed that the temperature significantly influenced the crack growth behaviour of the structure with tensile loads. However, various types of material played a more critical role in actual failure performance. The experiments showed that higher temperature decreased the COS below the glass transition temperature. However, it is more critical for the substrate softening effects and associated shrinkage behaviour over the glass transition temperature, which increased the COS at an elevated temperature.

Similarly, Zhang et al. tested the fracture behaviour for a glass fibre-reinforced polymeric joint. The research proposed that the temperature cannot influence the crack initiation loads when it was lower than the material glass transition temperature. However, another different conclusion is that lower temperature accelerated the FCG rate. The reason for it was that higher temperature increased the critical strain energy release rate required in the crack initiation and growth process (Zhang, Vassilopoulos and Keller, 2010).

Luo et al. proposed that temperature affected the crack growth behaviour in rubber polymer with the influence of the structural tear energy. They proposed the prediction model for FCG rate based on the critical tear energy, as shown in **Figure 2-8** (Luo et al., 2019). The model showed that higher temperature promoted crack propagation in rubber.

Martin and Gerberich investigated the FCG properties of PC with the consideration of environmental temperature. FCG behaviours were tested between a temperature range of 100 - 373 K. Then, it was further evaluated to build an empirical model according to fracture toughness. The model's parameters are shown in **Table 2-3**. PC was least tough at 223 K rather than 100 K. 223 K seems to be the transition point. Fatigue crack resistance increased with an increase in temperature of more than 223 K. Below 223 K, fatigue crack resistance increased with decreasing temperature, as shown in **Figure 2-9** (Martin and Gerberich, 1976).

Mai and Williams (1979) conducted fatigue tests on PS notched specimens at different mean stress conditions with a temperature range between -60 and 60 °C. Specimens were tested dipped in detergent and corn oil. The experimental results were plotted in **Figure 2-10**. The research calculated the Paris law parameters with these SIF range-FCG rate curves. They also investigated the effects of the environmental temperature and load range. The empirical parameter values in Paris law, as shown in **Table 2-4**, showed wide ranges of the parameters A and m. So it was challenging to give physical meanings to their values(Mai and Williams, 1979).

Kim and Mai (1993) investigated how temperature affected the FCG in an un-plasticised PVC (uPVC) pipe-grade polymer during the temperature ranges from -30 to 60 °C. They proposed that it is appropriate to use the Arrhenius relationship between FCG rate *da/dN,* and temperature T to model the FCG process with the independence of the SIF range ΔK. This developed model is shown in Equation **(2-16)**,

Table 2-2 FCG test for polymers under different temperatures

Testing Method	Material	Temperature Range	Authors/Year of study
Tension FCG Test	PC	-173°C to 127°C	Martin and Gerberich (1976)
Tension FCG Test	PS	-60°C to 60°C	Mai and Williams (1979)
Tension – Relax FCG Test	Polypropylene (PP)	-20°C to 20°C	Iwamoto, Jinen and Suzuki (1988)
Tension FCG Test	PEEK	39°C to 100°C	Brillhart and Botsis (1992)
Tension FCG Test	ABS	-50°C to 80°C	Kim, Wang and Abdullah (1994)
Tension FCG Test	Chlorinated polyvinyl chloride (CPVC)	-10°C to 70°C	Irfan-ul-Haq and Merah (2003)
Tension FCG Test	CPVC	-10°C to 70°C	Merah, Irfan-Ul-Haq and Khan (2004)
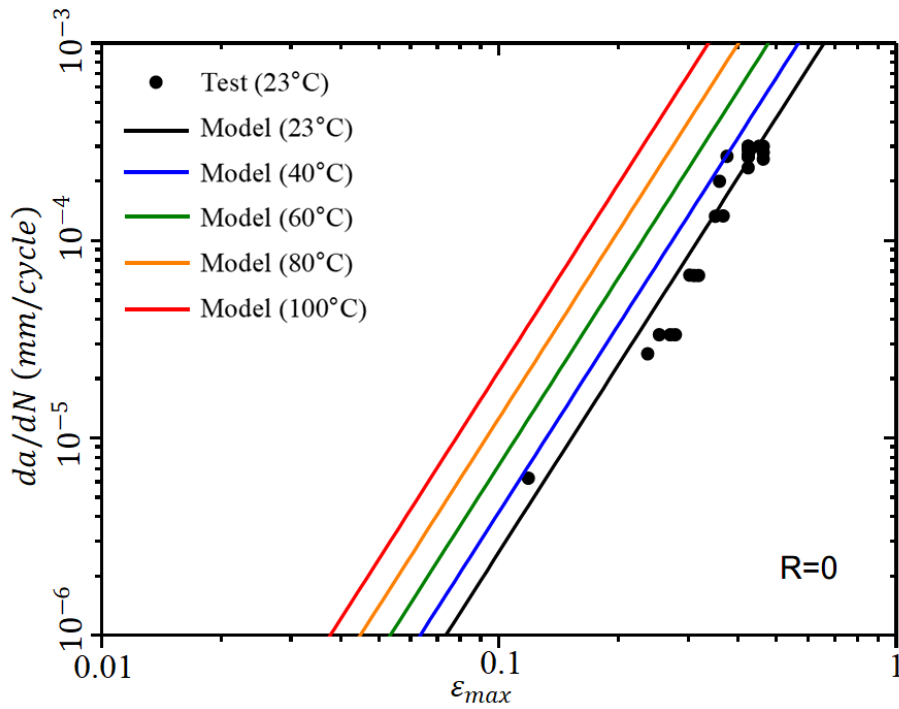
Figure 2-8 Modelling results of FCG rate at temperatures above 23 °C (Luo et al., 2019)

Table 2-3 Paris law parameters for PC (Martin and Gerberich, 1976)

Temperature (°C)	α (mm/cycle)	m
-172	$5.2*10^{-6}$	6.5
-150	$1.9*10^{-6}$	8.4
-125	$1.6*10^{-6}$	10.0
-100	$1.8*10^{-5}$	7.2
-75	$8.8*10^{-6}$	9.8
-50	$2.9*10^{-5}$	10.7
-21	$2.5*10^{-5}$	8.6
0	$9.4*10^{-6}$	7.5
25	$2.7*10^{-4}$	3.9
40	$2.4*10^{-4}$	3.2

50	1.1*10^{-4}	4.1
100	1.4*10^{-3}	1.2
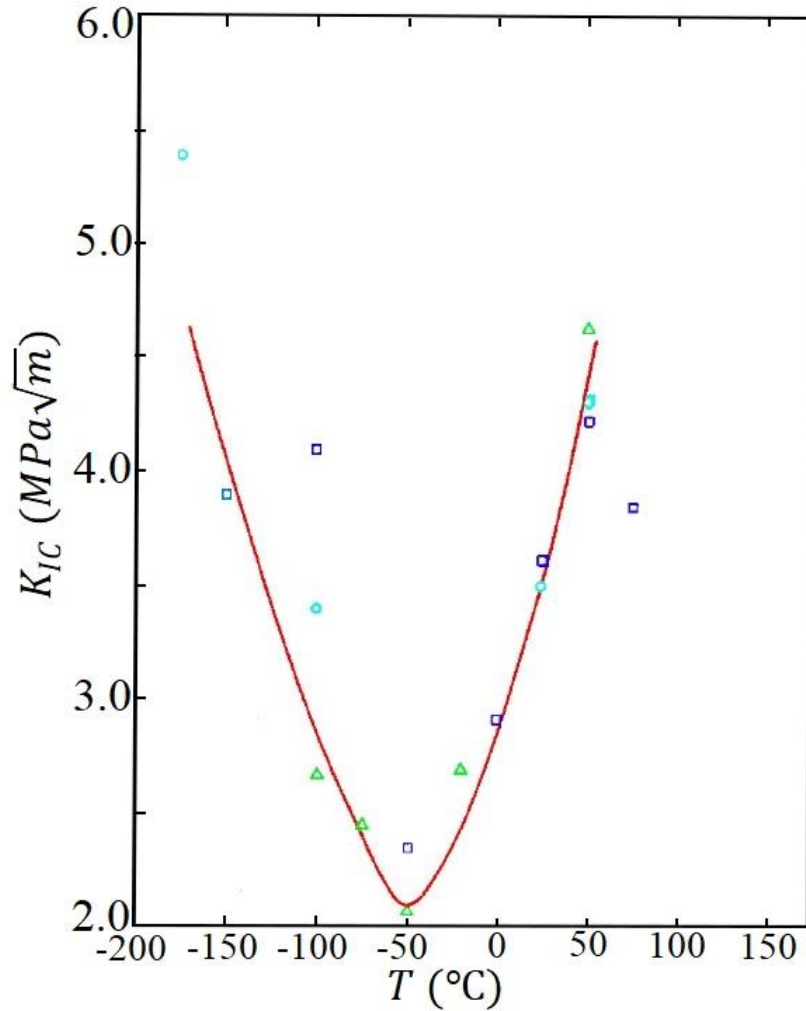
Figure 2-9 Fracture toughness variation with the temperature for PC (replotted) (run at 1 Hz in sinusoidal oscillation) (Martin and Gerberich, 1976)

Table 2-4 Paris law parameters for PS (Mai and Williams, 1979)

T (°C)	$log_{10} A$	m	da/dN $(\mu m/\text{cycle})$
60	0.91	3.1	0.3 to 20
40	0.76	3.7	0.2 to 10

30	0.74	3.8	0.1 to 10
20	0.39	4.3	0.1 to 7
0	0.07	3.6	0.1 to 2
-20	-0.26	2.6	0.1 to 1
-60	0.48	7.4	0.01 to 0.2
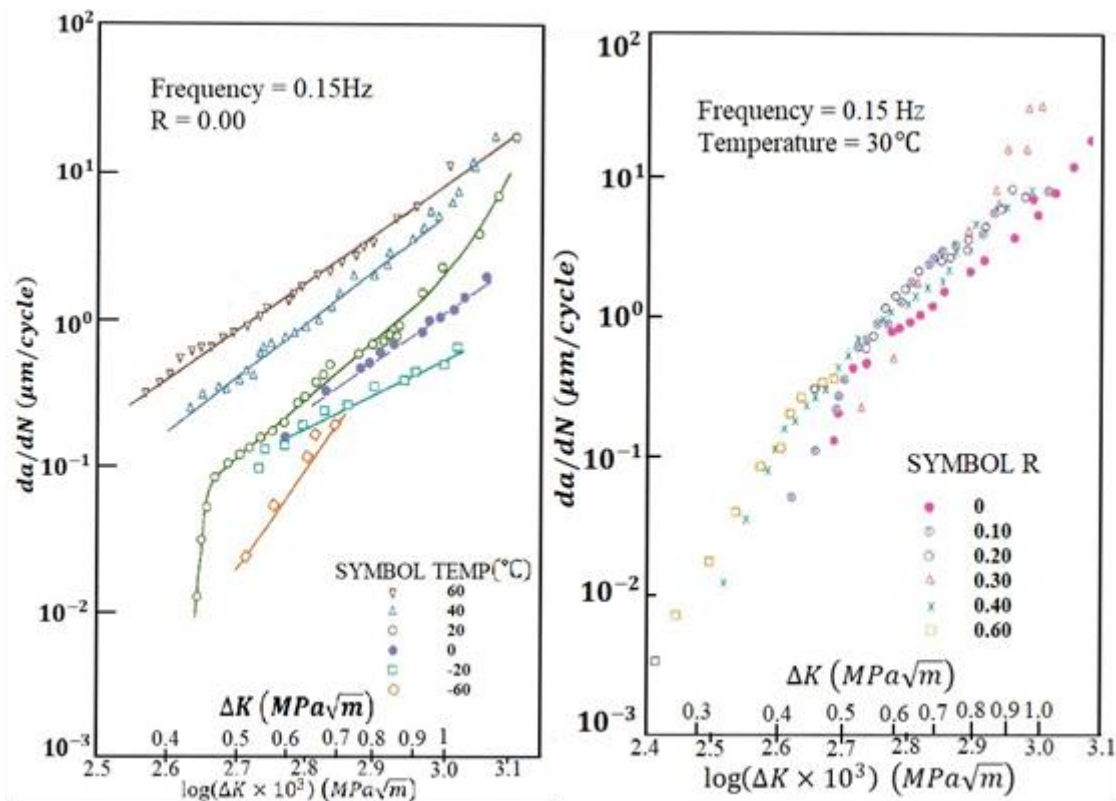
Figure 2-10 Influence of temperature and R Ratio to da/dN (replotted)(150mm*50mm SEN specimen with 9 mm initial crack depth, 0.15Hz test frequency) (Mai and Williams, 1979)

$$\frac{da}{dN} = Bexp\left[\frac{-(\Delta H_{th} - \gamma log\Delta K)}{RT}\right] \tag{2-16}$$

Where B is a constant, ΔH_{th} is 'the thermal activation energy independent of mechanical work' and $\gamma log\Delta K$ is a 'SIF biased term'. They proposed that different activation energies corresponded to two specific crack propagation

processes. Shear mechanism played a significant role under low temperature. However, multiple crazing mainly led to the final fatigue failure when the high temperature (Kim and Mai, 1993).

Furthermore, Kim, Wang and Abdullah (1994) studied the crack propagation in a commercial ABS with the temperature ranges -50°C - 80°C. They utilised the above Equation **(2-16)** to calculate the constants in Paris law and then compared the experimental values. The data are shown in **Figure 2-11**. They pointed out that the FCG rate increased more rapidly at temperatures from 19 °C to 80 °C than from -50 °C to 19 °C due to two modes of crack growth under these different temperature ranges (Lim, Jeong and Keum, 2003).

Lugo et al. experimentally investigated the structure-property relationships of ABS for crack propagation and extended the microstructure-based fatigue model from metal to ABS with appropriate parameter identification. They mentioned that the generated heat increased the surface temperature during fatigue tests, as **Figure 2-12** showed. Also, its reasons were the stretch and ordering of polymer chains(Lugo et al., 2014).

Kuronuma et al. (Kuronuma et al., 2011) presented the characterisation for crack propagation of the carbon nanotube (CNT)-based polymer applied with cyclic loads through a semi numerical semi-experimental approach. They performed the FCG test using cracked CNT/PC composites plate samples under room temperature/77 K, respectively. The experimental data were represented by FCG rates da/dN with a similar Paris law form relationship (Equation **(2-17)**),

$$\frac{da}{dN} = C(\Delta J)^m \qquad \text{(2-17)}$$

Where C and m are constant terms fitted according to the experimental data plot. J-integral (strain energy release rate) range ΔJ was determined by two-dimensional elastoplastic finite element analysis. da/dN curve is shown in **Figure 2-13**.
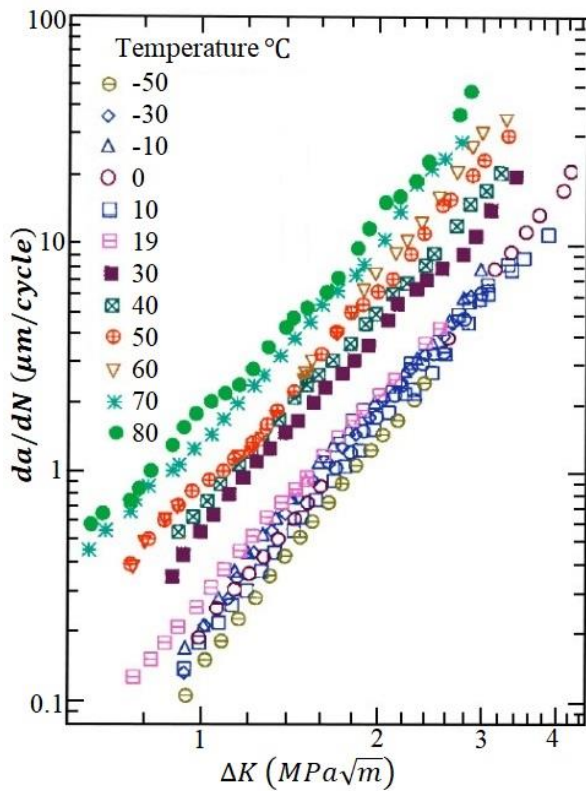
Figure 2-11 Effect of temperature to da/dN of ABS (replotted) (70mm*120mm SEN specimen, 5Hz loading frequency, stress ratio R=0.1)(Lim, Jeong and Keum, 2003)
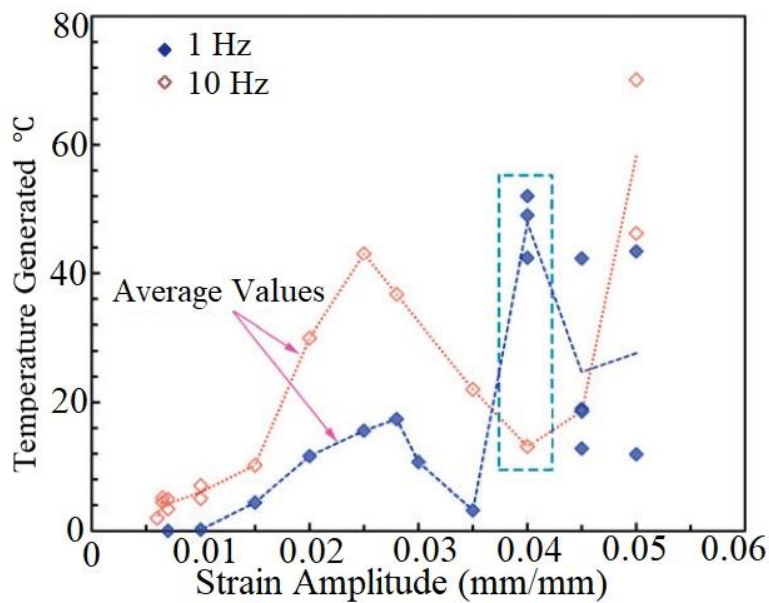
Figure 2-12 Self-heating effect in the test at 1 Hz and 10 Hz at corresponding strain amplitudes. (replotted) (Lugo et al., 2014)
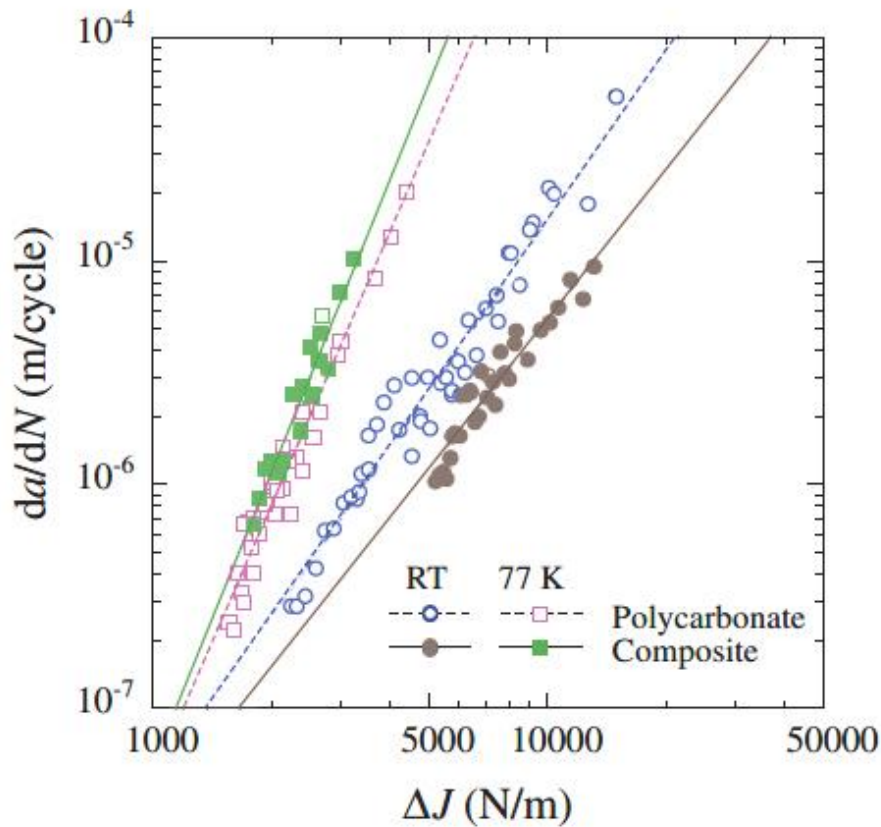
Figure 2-13 da/dN of PC at room temperature and 77K (replotted) (load ratio R=0.1, 3Hz load frequency) ((Kuronuma et al., 2011)

The crack growth relationships for a neat PC and a multi-walled nanotube /PC composite at room temperature were determined, as shown in Equation **(2-18)**:

$$\begin{cases} \dfrac{da}{dN} = 1.26 \times 10^{-15}(\Delta J)^{2.52} \quad (PC) \\ \dfrac{da}{dN} = 6.38 \times 10^{-15}(\Delta J)^{2.23} \quad (Composite) \end{cases} \qquad \text{(2-18)}$$

The Paris law relationships for the 77 K data were estimated, as shown in Equation **(2-19)**:

$$\begin{cases} \dfrac{da}{dN} = 3.22 \times 10^{-20}(\Delta J)^{4.06} \quad (PC) \\ \dfrac{da}{dN} = 4.73 \times 10^{-21}(\Delta J)^{4.35} \quad (Composite) \end{cases} \qquad \text{(2-19)}$$

Merah et al. investigated the crack growth in the weld zone of a CPVC pipe fitting considering the temperature effect. They observed that the crack initiated

27

on the knit line at one of the inner corners of the ring specimen. Following the initiation period, the crack grows first, in the axial (longitudinal) direction. As for the radial direction, small cracks were observed to initiate along the weld line before the main crack tip. These small cracks form in the craze zone that has a lighter (whitened) colour. They also evaluated the influence of temperature on FCG behaviours, as shown by **Figure 2-14**. The craze zone surrounding the crack tip was longer at higher temperatures. Fewer secondary small cracks have been observed to initiate ahead and around the main crack tip for both 50°C and 70°C when compared with room temperature. It explained that the FCG resistance decreased under higher temperature. (Merah et al., 2001)

Some other research also investigated the heat generated from the craze zone during crack propagation (Basu and Giessen, 2002; Bjerke and Lambros, 2002, 2003; Kotousov, 2002). Estevez et al. analysed the mode I crack of glassy polymers with the temperature influence. Their research proposed that the visco-plastic shear yielding and crazing generated the heat. It increased the temperature and affected the toughness of the material. Crazing was considered as the primary heat source, so the thermal effect due to high loading rates needs to be considered in future experiments.(Estevez, Basu and Giessen, 2005)

Chen and Liu also investigated the heat generation in the near-tip zone due to the crack growth for a PC film. They applied the thermal imaging infrared camera to record the temperature change in the moving crack tip, as shown in **Figure 2-15**. The experimental results indicated that the higher FCG rate increased the temperature at the crack tip. It might be a potential reason for the higher FCG rate in the specimen under high environmental temperature. (Chen and Liu, 2015)
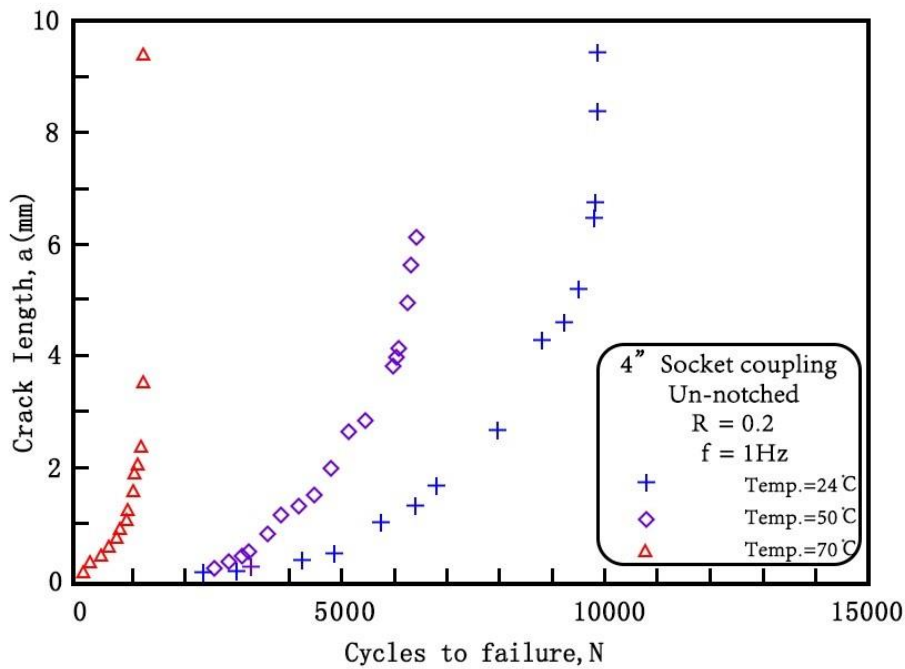
Figure 2-14 Temperature influence on FCG in CPVC fitting weld zone (replotted) (Merah et al., 2001)
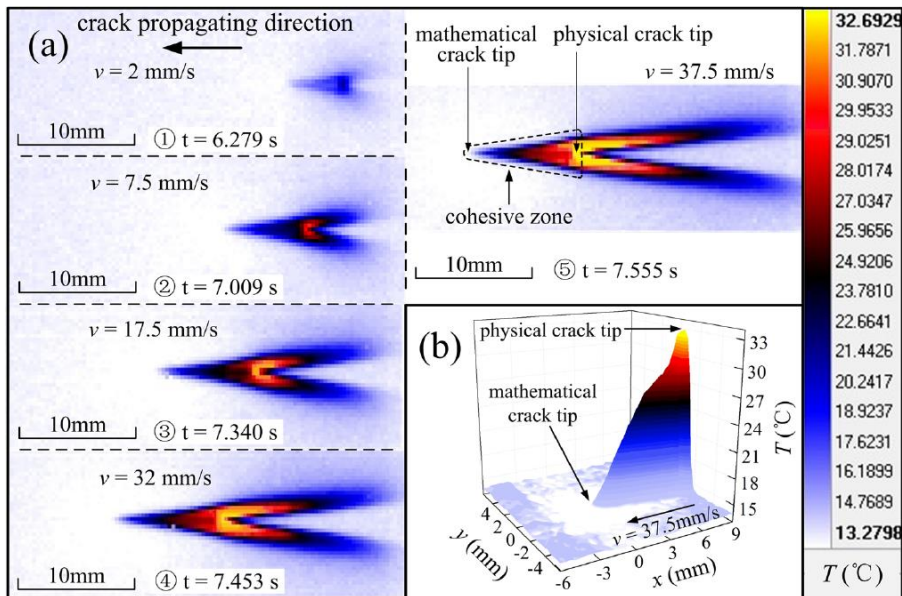
Figure 2-15 Contour map for the thermal distributions close to crack tip (Chen and Liu, 2015)

2.4.2 Effects of Frequency of Applied Load on Crack Propagation

Apart from the temperature influence, the load frequency also affects the FCG rate in polymers. A large amount of research investigated the relationship between them, as shown in **Table 2-5**.

Hertzberg, Manson and Skibo evaluated the frequency of applied load influence on the FCG rate of various polymers between a range from 0.1 to 100 Hz. They proposed that the FCG rate declined and fatigue resistance remarkably increased with higher load frequency for PMMA, PS and PVC. On the other hand, PC, poly bisphenol-A sulfone (PSF), Nylon-66, and polyvinylidene fluoride (PVF2) exhibited a slight increase in FCG rate with an increase in test frequency (Hertzberg et al., 1979; Hertzberg, Manson and Skibo, 1975; Manson et al., 1975). The reason for it was due to the different Young's Modulus-frequency sensitivity for different polymers.

Williams (1977) investigated the relationship between the FCG rate and the loading frequency based on semi-analytical methods. In their research, frequency effects in the crack growth were deduced from the viscoelastic mechanical properties of polymeric materials. Young's Modulus of polymers is time-dependent since the material is visco-elastic. Substituting the time-dependent E into the expression of SIF with the crack opening displacement (COD), they proposed potential relationships, as shown in Equation **(2-20)**,

$$\frac{da}{dN} \propto f^n \tag{2-20}$$

Where f is the load frequency, and n is the coefficient. With this relationship, research modelled the FCG rate for PMMA, as shown in Equation **(2-21)**.

$$\frac{da}{dN} \propto f^{-0.43} K_{mean}^{2.13} \Delta K^{2.39} \tag{2-21}$$

The relationship fitted well by regression analysis with the experimental results (Williams, 1977).

Table 2-5 FCG Previous research for Polymers with Different Load Frequencies

Testing Method	Material	Specimen Geometry	Frequency Range (Hz)	Authors/Year of study
Tension FCG Test	PMMA/PVC/PS/PC/Nylon 66	SEN Specimen	0.1 to 100	Hertzberg, Manson and Skibo (1975)
Tension FCG Test	PC & Nylon 66	SEN Specimen	0.3 to 10	(Manson et al., 1975)
Tension-Compression FCG Test	Poly Propene (PP) & Polybutylene terephthalate (PBT)	Dog Bone	0.063 to 20	Radon and Culver (1975)
Tension FCG Test	Nylon 66	CT Specimen	1 to 50	Hahn et al. (1982)
Tension FCG Test	PMMA	SEN Specimen	0.1 to 10	Chou and Sun (1983)
Tension & Compression FCG Test	high-density polyethylene (HDPE)	Centrally cracked tension (CCT) specimen	0 to 8	Dumpleton and Bucknall (1987)
Tension FCG Test	Nylon	CT Specimen	0.1 to 5	WYZGOSKI, NOVAK and SIMON (1990)

Tension & Compression FCG Test	HDPE	CT Specimen	0.01 to 1	Parsons et al. (2000)
Tension FCG Test & Tension-Compression FCG Test	PP Composite & PA Composite	Dog Bone	0.125 to 20	Eftekhari and Fatemi (2016)
Tension Fatigue Test	PEEK	Dog Bone	0.25 to 2	Shrestha et al. (2016)

Besides, some other research also carried out the experimental tests to investigate the frequency effect (Chou and Sun, 1983; Dumpleton and Bucknall, 1987; Eftekhari and Fatemi, 2016; Hahn et al., 1982; Mortazavian and Fatemi, 2015; Parsons et al., 2000b; Seichter et al., 2017; Wyzgoski, Novak and Simon, 1990; Zhou and Brown, 1992). Ford et al. investigated the FCG mechanisms in PC polyurethane (PU), which is a potential material for the orthopaedic joint replacement application, with respect to frequency effects. The research observed that primary crack propagated along the two-dimension plane when load frequency was 2 or 5 Hz without strong crack deflection. However, 10 Hz load frequency led to a large deflection in the crack tip, and specimens occurred multiple crack fronts (Ford et al., 2018)(Chandy et al., 2009).

Hartwig and Knaak proposed an interesting explanation about the frequency influence on the FCG rate in polymers. They conducted the fatigue test at 77K. This low temperature eliminated the viscoelastic influence, so the load history and frequency did not affect mechanical deformations. However, tensile-compression loads still showed a significant dependency on frequency. The thermal stresses may cause the phenomenon resulting from the samples' self-heating (Hartwig and Knaak, 1991).

2.4.3 Effects of Temperature and Frequency combination on Crack Growth

Numerous researchers (Merah et al., 2005, 2006; Saghir et al., 2005; Shrestha et al., 2016) investigated the dual influence of temperature and the frequency of applied load to FCG of structural polymers. Generally, the FCG rate increases at the higher temperature but decreases under a higher frequency load.

Radon and Culver (Radon and Culver, 1975b, 1975c) investigated the crack propagation in PMMA and PC under different temperatures from -60 to 21 °C at 0.1 to 100 Hz load frequency range. They concluded that the FCG rate was positively related to environmental temperature but negatively correlated with load frequency in the evaluated range. The FCG rates increased distinctly when the temperature rose from -60 °C to 27 °C. This increasing percentage was up

to 60% and 90% for PC and PMMA, respectively. The effect of load frequency on crack propagation was extremely slow at higher frequency values and reduced by one order of magnitude when increasing load frequency from 5 to 100 Hz.

Cheng et al. conducted experiments to evaluate the FCG in PMMA. They investigated how temperature and cyclic frequency affected FCG rate. The test was carried out with the frequencies of 1/10/50/100 Hz under the environmental temperature range between -30 °C and 100 °C. Compared with Radon and Culver's research, one exception was reported that the FCG rate increased with frequency increase at high temperature. The reason for the exception was that hysteretic heating at a higher temperature area softened the material and led to larger chain mobility, which accelerating the FCG rate(Cheng et al., 1990).

Kim and Wang (Kim and Wang, 1994) investigated the effect of temperature and load frequency on FCG rate. They developed an FCG rate model for estimating the function between FCG rate, temperature and frequency, as shown in Equation **(2-22)**,

$$\frac{da}{dN} = f^{-nm} C e^{-\frac{\Delta H_{th} - \gamma log \Delta K}{RT}} \tag{2-22}$$

Equation **(2-22)** represents the coupled influences of frequency and temperature on the FCG rate. They validated Equation **(2-22)** on un-plasticised polyvinyl chloride (uPVC) and calculated the FCG rate under various temperatures and frequencies.

Moreover, they (Kim and Wang, 1995) empirically modelled temperature and load frequency influence on crack growth in ABS. The FCG tests were conducted at 10°C to 70°C temperature range with 0.01 to 10 Hz frequency. Results are shown in **Table 2-6** and **Figure 2-16**. They indicated that higher frequency reduced FCG rates at all temperature ranges. Although either temperature or frequency can affect the crack propagation, the influence of frequency on FCG rate in 10 °C did not appear to be as critical as at elevated temperature.

Table 2-6 Paris law parameters A and m of ABS (da/dN in μm/cycle, ∆K in MPa√m) (Kim and Wang, 1995)

Frequency (Hz)	Temperature (°C)	A	m
0.01	50	2.301	2.94
0.1	30	0.934	3.13
	50	1.583	2.79
	70	2.280	2.79
1	30	0.552	3.05
	50	0.990	3.06
	70	1.422	3.01
10	30	0.390	3.14
	50	0.598	3.07
	70	0.890	2.98

Apart from the external environmental temperature, some research also mentioned that the temperature change due to high-frequency vibration might also affect the crack growth rate (Riddell, Koo and O'Toole, 1966). Qi et al. tested the crack propagation in HDPE, which was used in the automotive industry, with the different loading frequencies. Their research showed that temperature increased in the test. Higher loading frequency led to more significant temperature change, as shown in **Figure 2-17**. This increased temperature also affected the crack growth rate in HDPE. This research pointed out that the experimental tests for crack growth in polymers had to consider the non-independent interaction between the load frequency and temperature. (Qi et al., 2017)
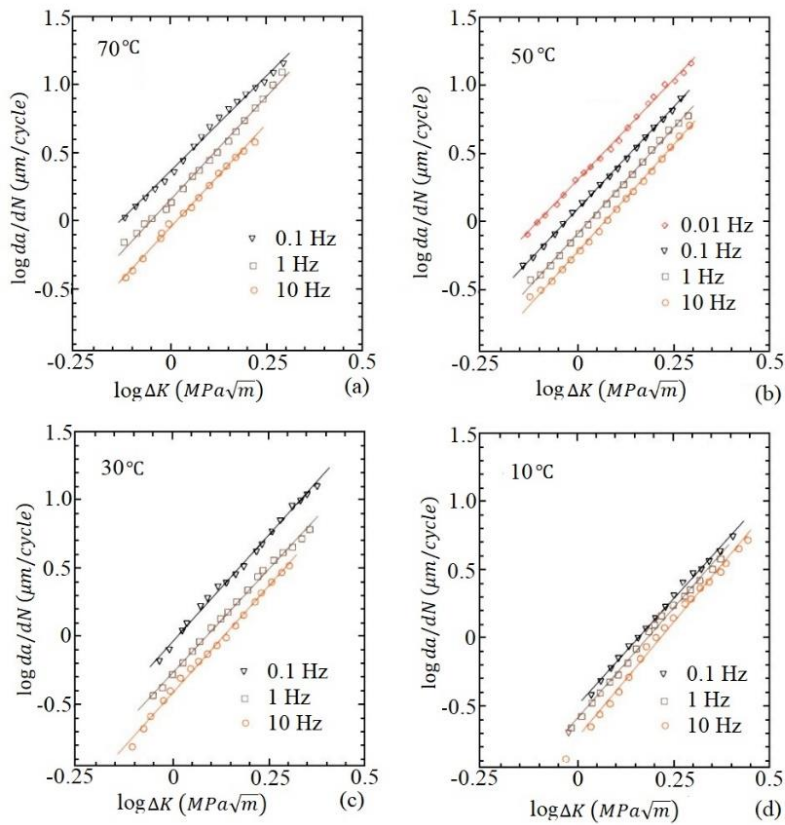
Figure 2-16 FCG rates of ABS at different frequencies and temperatures (replotted) (Kim and Wang, 1995)
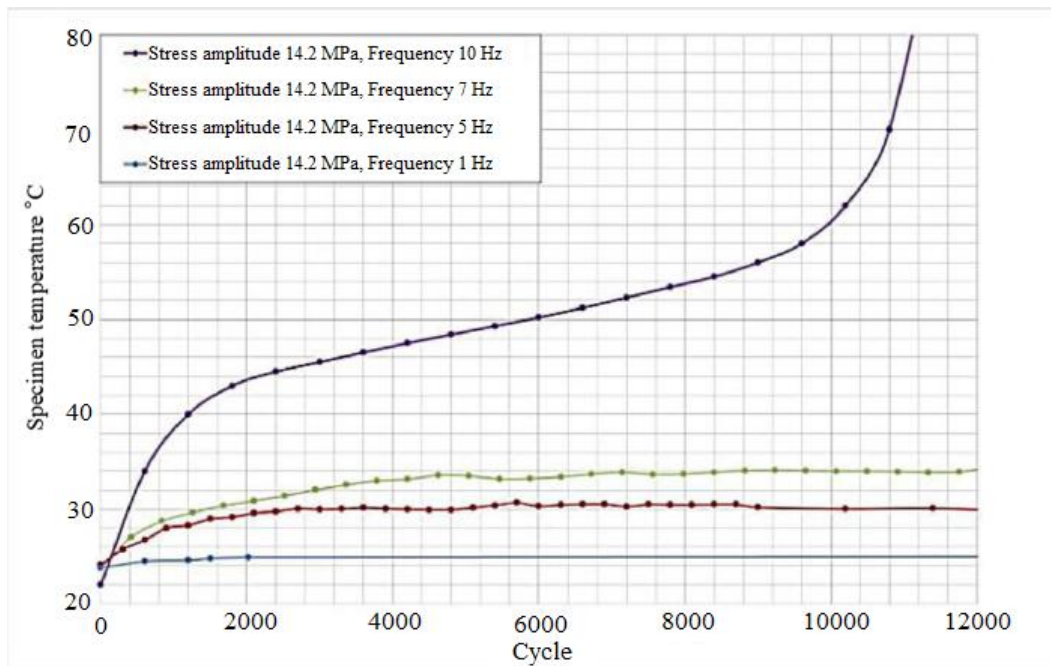
Figure 2-17 Frequency effect on the temperature of the specimen under the same stresses during whole fatigue life (Qi et al., 2017)

36

2.4.4 Critical Observations about Crack Propagation under Thermo-mechanical Loads

Most research concluded that higher temperature and lower load frequency increased the FCG rate. The micro molecular behaviour of polymers, including chain repetition and disentanglement, are easier and more frequent at higher temperatures (Kim and Wang, 1994). This chain slippage (Shown in **Figure 2-18**) is proposed to be the primary molecular motion that causes fatigue failure of the polymer. Therefore, a higher temperature reduced fatigue resistance. It is considered as the reason for the higher FCG rate at elevated temperature.
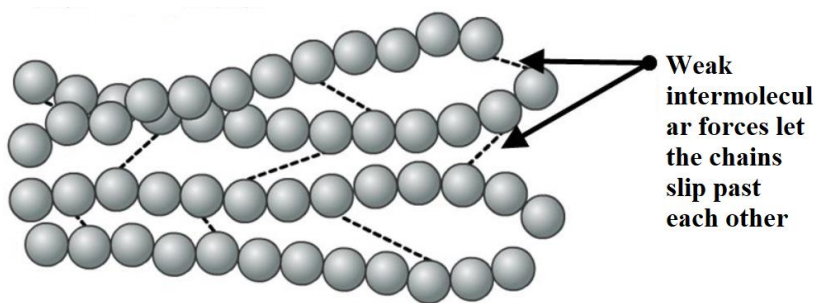
Figure 2-18 Chain slippage in thermoplastic polymers (He, Kumar and Khan, 2020)

On the contrary, higher load frequency leads to a stiffer physical state of polymeric structures. It lowers the trend of chain slippage. So FCG rate decreases when applied higher frequency load.

The above research all focused on the cyclic mechanical/thermo-mechanical loads and proposed some conclusions. However, their loads' conditions were all static/quasi-static. The investigation under dynamic loads is still missing. This dynamic load condition means the stress amplitude, environmental temperature and load frequency are time-dependent. The research effort needs further study focusing on these time-variable conditions.

2.5 Other Factors Affecting Crack Propagation

Apart from the temperature and load frequency, some other parameters may also influence the rate of crack growth (Ding et al., 2019; MARS and FATEMI, 2004; Poduška et al., 2017; Takei and Matter, 2018; Tee, Loo and Andriyana, 2018). As discussed above, Fang, Wang and Li researched overloading

conditions' effect on FCG rate (Fang, Wang and Li, 2007). Similarly, Zhang et al. (Zhang et al., 2008) investigated how compressive loads changed the stress condition at the crack tip and how it affected the FCG rate. Compared with the standard tensile test, the crack growth in the compression-tensile test was more complicated. They proposed that maximum stress intensity and compressive stress determined these local crack tip parameters. They presented the modified crack growth model with this conclusion, shown in Equation **(2-23)**. C, α, β and γ are material constants. σ_{maxcom} is maximum applied compressive stress, σ_{ys} is material's yield stress.

$$\frac{da}{dN} = C\left[1 - \gamma\left(\frac{\sigma_{maxcom}}{\sigma_{ys}}\right)\right]^{\beta} (K_{max})^{2(\alpha+\beta+1)} \tag{2-23}$$

On the other hand, polymeric structural properties can also affect the crack growth rate. Baker, Hastings and Pruitt experimentally investigated the effect of morphology, sterilisation, ageing and temperature in the polymer manufacturing process on the crack propagation behaviour of UHMWPE (Baker, Hastings and Pruitt, 2000). Shah et al. evaluated the effect of the structural geometry on crack initiation and growth in polymers (Parsons et al., 2000a; Shah et al., 1997, 1998). The research cut a non-standard specimen from the polyethene (PE) pipe and compared it with the standard CT specimen. Test results demonstrated that crack propagation behaviour in the non-standard specimen, which conserved the pipe geometry, could be well replicated using the standard compact tension specimen. Pruitt and Bailey evaluated the influence of manufacturing methods on the FCG rate of UHMWPE (Pruitt and Bailey, 1998). They considered two methods: compression moulding and ram extrusion. They concluded that the parts with a notch direction parallel to the extrusion had a lower fatigue threshold.

The above-described reviews are focused on conventional fabricated polymeric structures. The mechanics of crack propagation become more complicated if these structures are developed using additive manufacturing such as 3D printing because different manufacturing methods cause different micro-structures. Several parameters can influence the crack growth rate in printed

polymers. Therefore, Section 2.6 will discuss the crack propagation in printed polymeric structures.

2.6 Crack Propagation of 3D printed Polymers

A very few studies related to the crack growth under the mechanical loads are reported for printed polymeric structures. Authors have found no comprehensive research emphasised crack propagation, especially in fused deposition based printed polymers under thermo-mechanical loads. Most of the available literature discussed the fatigue test of FDM polymers, emphasising printing parameters and their influence on fatigue life. Therefore, the author has reviewed the studies related to fatigue life and the influence of printing parameters on it.

2.6.1 Effect of 3D Parameters to Mechanical Behaviours of FDM Polymer

Mechanical properties of the structure have a relationship to the FCG rate at the microstructure scale (Safai et al., 2019). The printing parameters directly affect the microstructural characteristics and thus change the mechanical properties in 3D printed polymers, and hence these parameters also influence the crack growth rate. Therefore, Comprehensive literature in the past has discussed the influence of 3D printing parameters on mechanical behaviours of polymeric materials, such as Young's Modulus and tensile strength (Ahn et al., 2002; Ang et al., 2006; Foyos et al., 2000; Lee, Abdullah and Khan, 2005; Ning et al., 2017; Shojib Hossain et al., 2014; Torrado et al., 2015; Türk et al., 2017). These researchers investigated the relation between printing parameters and static mechanical properties. They optimised the parameters to improve structural Tensile Modulus, thereby increase the fracture toughness of FDM polymers.

Popescu et al. presented a comprehensive and systematic review of how FDM process parameters affect the mechanical behaviours of structures. Most past studies focused on ABS, PLA and PEEK material (Popescu et al., 2018).

Rodriguez, Thomas and Renaud determined the mechanical behaviours of FD ABS plastic material through experimental study. The test results showed that

the modulus of the FD-ABS specimen was reduced by 11% to 37%, and the strength was reduced by 22% to 57% compared with ABS filament. The reason for it was 'the existing voids and loss of molecular orientation due to FD extrusion' (Rodriguez, Thomas and Renaud, 2001). Moreover, they proposed the analytical model for the mechanical behaviours of the resulting parts fabricated with ABS material. They proposed that the anisotropy of the structure affected the stiffness and strength. The research employed the mechanics of material and homogenisation approaches, respectively to build the constitutive model and then predict properties of unidirectional FD-ABS materials. However, the model tended to over-predict the modulus than the actual data because the mechanical properties of ABS thermoplastic changed during the FDM process. (Rodríguez, Thomas and Renaud, 2003).

Bellini and Güçeri proposed a method (Bertoldi et al., 1998) to calculate the stiffness matrix for a component fabricated with the FDM technique. ABS specimens were experimentally tested in their study. There were nine independent constants in the proposed semi-analytical model. It is essential to identify them to define the mechanical properties of an orthotropic part. Experimental tests were carried out for identification. So six different specimens with different orientations were tested. The research proposed that the mechanical properties of the final components were considerably related to two crucial modelling phases: the printing directions and path (Bellini and Güçeri, 2003). **Figure 2-19** shows two modes of building path.

(a)　　　　　　　　　　　　(b)

Figure 2-19 Different building paths (Bellini and Güçeri, 2003)

Schirmeister et al. modified several FDM parameters, including nozzle and support platform temperature, nozzle diameter, extrusion rate, and support platform material for improving the comprehensive mechanical behaviours and the surface quality of HDPE. They proposed that either nozzle diameter or printing speed is related to the surface quality without affecting mechanical behaviours due to the outstanding fusion of the polymer filament (Schirmeister et al., 2019).

2.6.2 Effect of 3D Printing Parameters to Crack Propagation of FDM Polymer

Although research in Section 2.6.1 has shown that various 3D printing parameters lead to different mechanical properties. However, only a handful amount of investigations have discussed the relationships between these parameters and crack propagation. Zhang et al. (Zhang et al., 2018) evaluated the creep-fatigue behaviours of ABS specimens through experiments. They systematically characterised the modulus of FDM ABS specimens with specifically considering building orientation. Results showed that the 0° building orientation had the most excellent mechanical behaviours. Young's modulus was improved to 1.81 GPa while ultimate strength reached 224 MPa.

Aliheidari et al. (Aliheidari et al., 2017) applied the fracture mechanics to characterise the fracture toughness of FDM ABS specimens considering nozzle and support plate temperatures. A numerical model determined the J-integral as a measure of fracture toughness. Their results showed that both higher nozzle and plate temperature led to the larger actual fracture surface area and improved the fracture toughness.

Isaac and Tippur (Isaac and Tippur, 2019) applied the quasi-static and impact fracture tests for FDM ABS specimens with the specific interest to the role of two different print architectures orientations. The test results showed that crack propagated and grew along the printing orientations. Rabbi and Chalivendra (Rabbi, Chalivendra and Li, 2019) did similar work. They carried out the impact test to evaluate the time-dependent fracture of an AM ABS specimen considering building orientations. Specimens were printed horizontally or

vertically. It meant that the printing layer was parallel or perpendicular to the initiated crack, respectively. There were also two raster orientations, ±45° and 0/90°. With the test data, accurate fracture initiation load was determined and derived the dynamic crack initiation resistance. They concluded that dynamic crack initiation resistance was improved by 138% for a vertical printed specimen compared with a horizontal printed one with 0/90° raster orientation. They also presented a dynamic SIF Equation **(2-24)**, which is suitable for all linear elastic specimens if their crack initiation times are long enough.

$$K_{ID} = \frac{F(t)}{B\sqrt{H}} f\left(\frac{a}{H}\right)$$

(2-24)

Where F(t) is the applied load, while *B*, *H* and *a* are the specimen width, height, and pre-crack length, respectively.

The above research developed the relation between printing orientations and fracture resistance. However, some other research had different conclusions. One research proposed that 0° raster orientation has the highest fracture toughness. However, another research pointed out that the printing orientation, which is perpendicular to the pre-crack, can increase the fracture toughness because of the anisotropic mechanical properties of polymeric materials.

2.6.3 Effect of 3D Parameters to Fatigue Life of FDM Polymer

Few numbers of research focused on the FCG rate of 3D printed polymers, as shown in Section 2.6.2. However, comprehensive research is available on how 3D printing parameters affect fatigue behaviour. Section 2.6.3 provides a critical review of the previous efforts investigating the relation between the 3D printing parameters and fatigue life of the polymeric structure, as shown in **Table 2-7**.

Jap et al. investigated the fatigue strength for dog-bone specimens of FDM ABS using the cyclic tensile test. They listed the potential factors in **Figure 2-20** that may affect fatigue strength and proposed that raster orientation was a critical parameter related to the tensile strength. Because 'the strength of the bonds between adjacent raster and layers' significantly influenced the mechanical behaviours of the components manufactured by FDM at the micro-molecular

level. The structural density also strongly affected its mechanical behaviours, while voids in components critically reduced the effective cross-section area where the stress was taken (Jap et al., 2019).
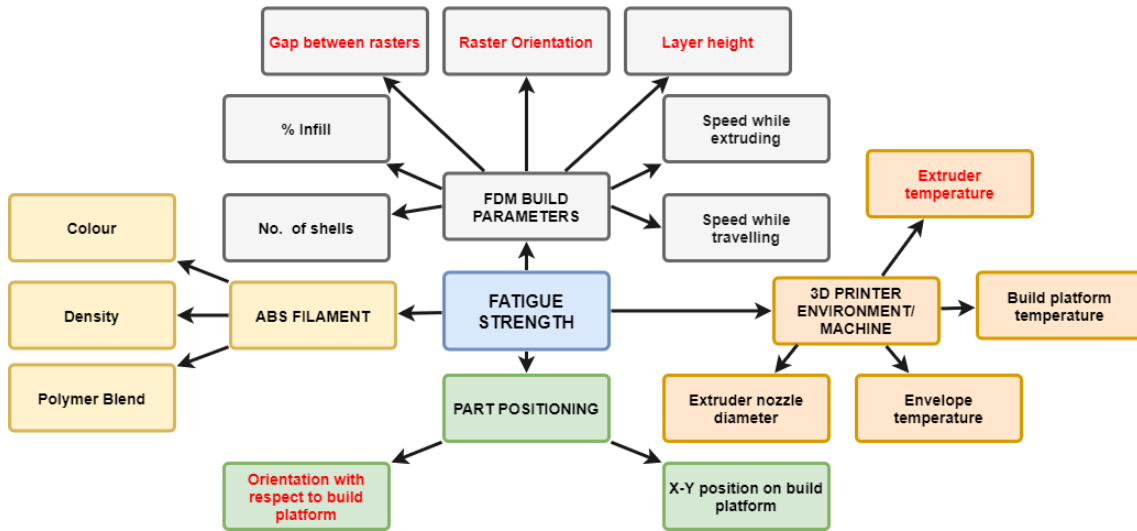
Figure 2-20 Influence parameters to fatigue strength (Jap et al., 2019)(He and Khan, 2021)

Imeri et al. (Imeri et al., 2018) investigated the fatigue performance of fibre-reinforced AM nylon structures through tensile tests. They analysed how fibre orientations, infill types, and fibre materials (carbon fibre, Kevlar and Fiberglass) affected fatigue. They concluded that the configurations including "isotropic" infill carbon fibre provided the specimen with the highest fracture resistance. Rybachuk et al. (Rybachuk et al., 2017) researched the anisotropic mechanical behaviours of FDM ABS specimens. They also evaluated the influence of infill orientations on the modulus/strength of structure under tensile and compression loads. They pointed out that infill orientation aligning to the vertical axis gave the specimen the best mechanical properties compared with other configurations. The reason for it was that the direction of the infill layers was perpendicular to the applied load. It allowed layers to unravel individually when applied the load.

Table 2-7 Research about the Effect of 3D Printing Parameters on Fatigue Life

Test Method	Material	3D Printing Parameters	Authors/Year of study	Key Findings
Tension Fatigue	ABS	Build Orientation	Ziemian, Sharma and Ziemian (2012)	The ±45° fiber orientation provided the longest fatigue life
Tension – Zero Fatigue	ABS	Build Orientation	Lee and Huang (2013)	The vertical 45° printing orientation had the best ultimate stress
Tension Fatigue	Polylactic acid (PLA)	Build Orientation	Afrose et al. (2014)	X-build orientation had the highest tensile stress
Tension-Compression Fatigue	PLA	Build Orientation	Letcher and Waytashek (2014)	90° raster orientation had the worst fatigue life
Tension Fatigue	ABS	Build Orientation	Ziemian, Okwara and Ziemian (2015)	Both 0°and +45°/-45° raster orientations had better fatigue life
Tension Fatigue	PLA	Build Orientation	Afrose et al. (2015)	45° build orientation showed the highest fatigue life

Tension Fatigue	ABS	Build Orientation	Ziemian, Ziemian and Haile (2016)	0° fiber orientation had the best fatigue life
Tension Fatigue	Ultem 9085	Build Orientation	Fischer and Schöppner (2017)	Z build orientation had the best fatigue life
Bending Fracture	ABS	Crack-tip/laminae Orientations	Hart and Wetzel (2017)	90° laminae orientation had the highest fracture toughness
Rotation Fatigue	PLA	Layer Height Fill Density Extruder Diameter Printing Speed	Jerez-Mesa et al. (2017) Gomez-gras et al. (2018)	75% infill, 0.5 mm nozzle diameter, 0.3 mm layer height provided optimal resistance to fatigue
Tension – Zero Fatigue	Polycarbonate urethane (PCUs)	Printing Speeds Extrusion Multipliers	Miller et al. (2017)	Increased PCU hard segment content leads to higher fatigue life
Tension Fatigue	PCUs	Printed Architecture	Miller et al. (2017)	Solid architecture had the best fatigue life

Tension Fatigue	ABS	Build Orientation Extruder Temperature Printing Speed Layer Height	Abbott et al. (2018)	XY building orientation provided the highest tensile strength Increasing print speed decreased the tensile strength The increasing temperature increased tensile strength
Compact Tension	PLA	Build Orientation	Arbeiter et al. (2018)	Three orientations were almost identical
Flexural Fatigue	PC	Build Orientation	Puigoriol-forcada et al. (2018)	YZ orientation provided the longest fatigue life

Suresh et al. modelled the relations between the build orientations and fatigue life. They used Veroclear polymer components with an inherent anisotropy by controlling the printing build orientation parameter (Suresh et al., 2018). They performed tensile and tensile-tensile fatigue cycle tests to evaluate the difference between parallel and perpendicular building orientations. The results showed that parallel building orientation provided higher strength and longer fatigue life, as shown in **Figure 2-21**. This is because the crack direction and applied stress in the parallel printed specimen can accelerate the FCG rate more than the perpendicular printed specimen. Perpendicular printed specimens showed the crack branching and fibre pull out, which led to the slower crack propagation.
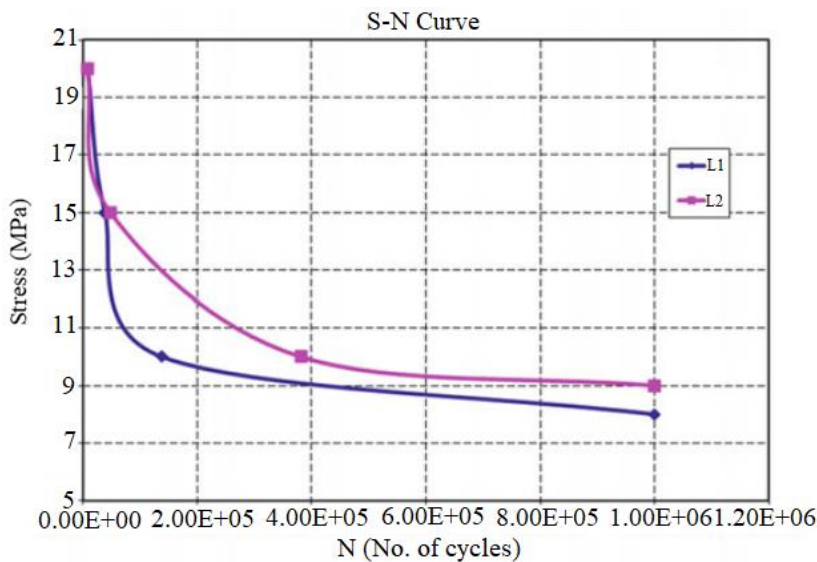
Figure 2-21 Fatigue life of the structures with different build orientation (L1: parallel oriented; L2: perpendicular orientation) (Suresh et al., 2018)

Afrose et al. (Afrose et al., 2016) analysed the relations between the structural building orientations and the fatigue life of the FDM PLA specimen. The dog-bone parts were fabricated with the consideration of three (0°, 90° and 45°) different building orientations and tested under 50 to 80 % nominal values of cyclic ultimate tensile stress. They concluded that the specimen with 0° build orientation had the highest tensile stress and 45° build orientation had the longest fatigue life.

47

2.7 Significance of Dynamic Response for Estimating Crack Growth in Structures

The coupled thermo-mechanical loads acting on the structure produces a corresponding specific dynamic response, such as fundamental frequency, mode shapes and displacement amplitude (Hoshyar et al., 2020; Jassim et al., 2013; Khan et al., 2015; Nahvi and Jabbari, 2005; Nguyen, 2014; Patil and Maiti, 2003; Revi and V.S., 2015; Zai et al., 2019b, 2020a). The value of the dynamic response is of course load-dependent. Different thermal loads can affect the structural fundamental frequency due to the global stiffness change. Meanwhile, the mechanical loads affect the displacement amplitude due to the different mechanical energy input to the structure (Gillich et al., 2019; Gupta et al., 2017; Khan et al., 2015; Zai et al., 2020a).

The structural dynamic response is also changed with the crack propagation in a structure due to the reduced local stiffness. These dynamic responses contain information about the locations and sizes of the crack(s) (Zai et al., 2020b).

Therefore, the dynamic response can not only present the thermo-mechanical loading conditions but also reflect the structural crack propagation. The modelling for the interaction between thermo-mechanical loads, dynamic response and crack propagation is critical.

Although a few studies have made an effort on the relationships between the dynamic response and crack growth in FDM structures (Zai et al., 2020b) (Baqasah et al., 2019). However, current research still lacks the analytical relationships between dynamic response and damage severity. The following chapters of the thesis will fill in these gaps.

2.8 Conclusion

Comprehensive reviews are reported with a focus on research efforts for crack propagation of polymers under thermo-mechanical loads. During the review, the author summarised that higher temperature and slower load frequency could increase the FCG rates in most of the polymeric structures. However, there are still some research gaps and potential research topics.

Most research efforts have ignored a fundamental problem with SIF. SIF is a parameter based on static stress derivation, so it is suitable as a criterion to judge the fracture of the structure under static failure stress. However, most studies used the maximum and minimum value difference in cyclic stress to represent the continuous state of stress change in the cycle. The SIF range ΔK applied in Paris Law even though loads were varied with time. Realistically, the loads are even far from being cyclic in actual load conditions, i.e. dynamic and/or stochastic. It is essential for overcoming this problem to convert the dynamic stress to cyclic conditions if one has to use SIF in future research. However, the conversion from the dynamic load history to a cyclic load sequence also significantly modifies the real load impact. This conversion affects the calculation of the FCG rate and concludes that the existing formulation is far from accurate due to their quasi-static remote stress assumption. Therefore, future work can focus on a real-time derivative crack growth equation rather than Paris Law for accurate calculations.

A large amount of research proposes the empirical relations between the FCG rate and stresses for some polymers. However, the academic domain still needs an analytical investigation that can truly represent the crack growth behaviour of polymers under thermo-mechanical loads. A few efforts reported their empirical findings of the crack growth rate under different temperature values on a range of frequencies of the applied load. However, they all have tested the structures under tension. Therefore, future research can consider experimental conditions under bending loads, which is also a very common and practical working condition.

There is a considerable research gap in crack growth in FD printed polymers even though FDM is developed rapidly. Existing research on these polymers are mostly empirical. They evaluated the mechanical performance of FD printed polymer under quasi-static loads and concluded the factors which can affect mechanical properties. So future research can carry out various fatigue tests to analyse how 3D printing parameters can affect the fatigue life of printed polymeric structures. Furthermore, no one has provided a comprehensive

discussion to introduce the exact crack propagation or growth in such structures. No one has reported the work about the influence of the parameters on the FCG rate in printed polymers. In the future, comprehensive research will be required to investigate the effects of coupled thermo-mechanical loads on crack propagation in 3D printing polymeric structures.

Most of the above-mentioned literature suggests that the crack propagation in FDM polymeric structures under thermo-mechanical loads needs further comprehensive investigations. However, to investigate this crack propagation more realistically or closer to the real applications, it is really important to perform the investigation in an in-situ manner. This can be possible if the structural dynamic response can be used to estimate the crack propagation due to its relationship with crack growth and location. However, current research still lacks the analytical relationships between dynamic response and structural damage severity.

3 ANALYTICAL MODEL FOR NATURAL FREQUENCY DURING CRACK PROPAGATION

The structural dynamic response can be expressed in terms of the fundamental frequency, displacement amplitude and mode shapes. The first two are discussed in this thesis. After all, it is simpler and more convenient to measure the fundamental frequency and structural displacement amplitude than monitoring the mode shapes in practical application scenarios. Most of the practical applications exhibit first mode shape, and due to its high energy content, it is mainly responsible for any change in structural properties.

3.1 Abstraction of Actual Working Conditions

There are different FDM structures in practical application scenarios. The cantilever beam structure was studied in this thesis like most prior research (Ellyson et al., 2017; Shinde and Katekar, 2014; Zai et al., 2020a) because the cantilever beam is a significant element in real engineering applications. It can

withstand high levels of mechanical loadings (Das, Saha and Patro, 2016)(Jassim et al., 2013). Structure such as wing and wind blade can be considered simply as a cantilever beam. On the other hand, the dynamic response of the cantilever beam is also most violent when it is excited.

The cantilever beam specimen's geometry is shown in **Figure 3-1**. The vibrated motion can excite the beam from the left fixed end. An initial seeded crack is on the top surface and near the fixed end of the beam to simulate the crack damage in practical structures. There are three crack locations. The distance from them to the fixed end of the beam is 5, 15 and 25 mm, respectively, to represent the different damage locations in real. Furthermore, unlike the practical application, an extra end mass on the beam free end represents an accelerometer used in subsequent experiments in the research.
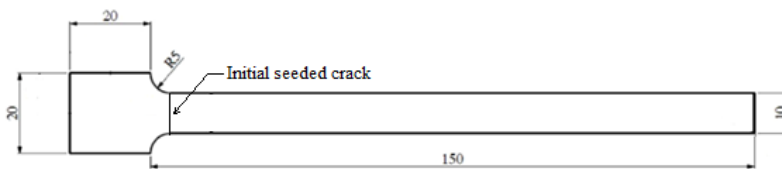
Figure 3-1 Geometry of specimen (Unit: mm)

3.2 Crack Size Modelling

The existence of cracks changes the local stiffness of the structure. A large crack depth decreases the local stiffness appreciably. Consequently, the crack in the beam can be represented by a torsional spring, as shown in **Figure 3-2** (Ostachowicz and Krawczuk, 1991). Ostachowicz & Krawczuk (1991) modelled the torsion spring stiffness corresponding to an open single-sided crack on a beam, as indicated in Equations (**3-1)** and (**3-2)**.
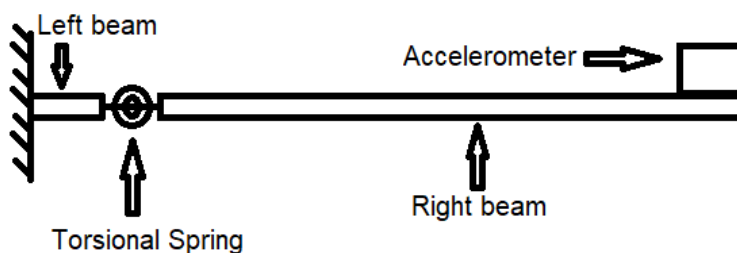
Figure 3-2 Cantilever beams - torsional spring - accelerometer system

$$k = \frac{EbH^2}{72\pi f_r\left(\frac{a}{H}\right)} \tag{3-1}$$

$$f_r\left(\frac{a}{H}\right) = 0.6384\left(\frac{a}{H}\right)^2 - 1.035\left(\frac{a}{H}\right)^3 + 3.7201\left(\frac{a}{H}\right)^4 - 5.1773\left(\frac{a}{H}\right)^5 \tag{3-2}$$
$$+ 7.553\left(\frac{a}{H}\right)^6 - 7.3324\left(\frac{a}{H}\right)^7 + 2.4909\left(\frac{a}{H}\right)^8$$

A large amount of research investigated the dynamic response of a cracked beam with the same spring stiffness model derived by fracture mechanics (Akbarzadeh Khorshidi and Soltani, 2013; Boltezar, Strancar and Kuhelj, 1998; Dastjerdi and Abbasi, 2019; Hu and Liang, 1993; Moradi et al., 2019; Nahvi and Jabbari, 2005; Nandwana and Maiti, 1997; Patil and Maiti, 2003)(Agarwalla and Parhi, 2013)(Barad, Sharma and Vyas, 2013)(Douka and Hadjileontiadis, 2005)(Ghadimi and Kourehli, 2017). They directly used Equations (**3-1)** and (**3-2)** as the relationship between the spring stiffness and crack depth. Their study assumed that the stress on the crack equals the bending stress on the beam surface owing to the constant moment. Notably, such approximate stiffness equations are suitable only for cracks near the surface. Such assumptions may lead to increasing errors in the spring stiffness with larger crack propagation depths. Therefore, a mathematical modification is introduced in Equation **(3-1)**, as shown in Equation (**3-3)**,

$$k = \left(\frac{H-a}{H}\right) \times \frac{E_T bH^2}{72\pi f_r\left(\frac{a}{H}\right)} \tag{3-3}$$

The additional term $(H-a)/H$ ensures that the spring stiffness tends to zero as the crack depth approaches the thickness of the beam, consistent with the actual situation. The difference in the modified stiffness and originally modelled stiffness is illustrated in **Figure 3-3**. As for the elastic modulus E_T, the increased temperature caused a reduction in it and eventually resulted in a drop in natural frequency (Baqasah et al., 2019), so it is a temperature-dependent value in Equation (**3-3)**.
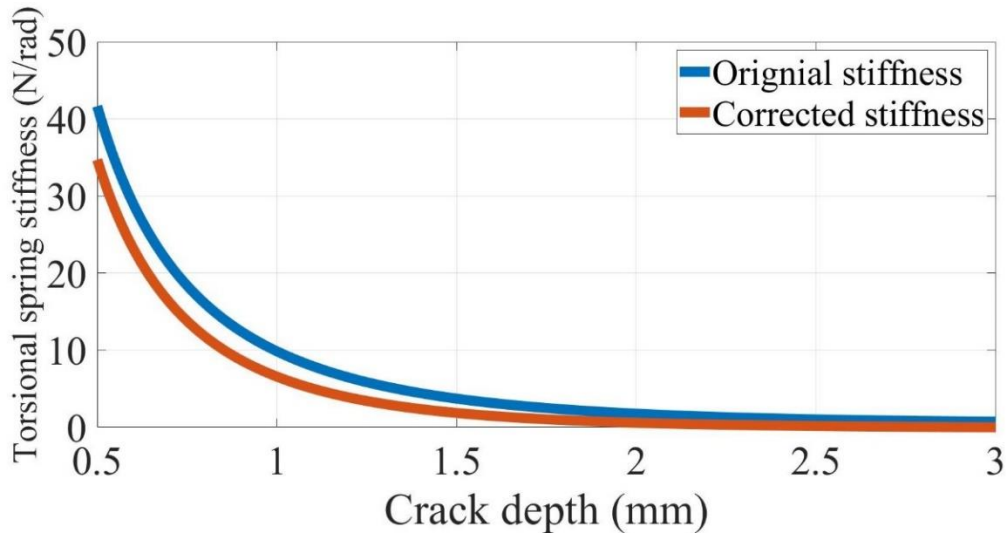
Figure 3-3 Torsional spring stiffness change as crack propagation for FDM ABS beam with 3 mm thickness, 10 mm width and 1600 MPa elastic modulus

3.3 Natural Frequency of the System

With the modified torsional spring model of Equation **(3-3)**, the cracked beam is represented by two separated full beams, as shown in **Figure 3-2**. Similar to the existing studies (Agarwalla and Parhi, 2013; Altunışık, Okur and Kahya, 2017; Baqasah et al., 2019; Barad, Sharma and Vyas, 2013; Boltezar, Strancar and Kuhelj, 1998; Chati, Rand and Mukherjee, 1997; Das, Saha and Patro, 2016; Douka and Hadjileontiadis, 2005; Fleet et al., 2020; Ghadimi and Kourehli, 2017; Gillich et al., 2014, 2015, 2019; Gillich and Praisach, 2014; Gupta et al., 2017; Hoshyar et al., 2020; Hu, n.d.; Hu and Liang, 1993; Jassim et al., 2013; Khan et al., 2015; Khiem and Huyen, 2017; Khiem and Tran, 2014; Loya, Rubio and Fernández-Sáez, 2006; Mazanoglu, Yesilyurt and Sabuncu, 2009; Mazanoglu and Sabuncu, 2012; Nahvi and Jabbari, 2005; Nandwana and Maiti, 1997; Nguyen, 2014; Nitesh A. and Vaibhav S., 2015; Pandey, Biswas and Samman, 1991; Patil and Maiti, 2003; Priyadarshini, 2013; Qian, Gu and Jiang, 1990; Revi and V.S., 2015; Rizos, Aspragathos and Dimarogonas, 1990; Shinde and Katekar, 2014; Zai et al., 2019b, 2020b, 2020a; Zhang and Yan, 2017), the classical Euler–Bernoulli beam theory is applied separately for the left and right beams. Because there is only one fixed end on the left of the beam, the thermal expansion owing to thermal loads (elevated ambient

53

temperature) does not introduce a force and moment. Only the fundamental frequency of the beam is calculated, and thus, the damping effect of the beam is neglected. The governing differential equation for the two beams can be expressed as Equation **(3-4)** and **(3-5)**.

$$E_T I \frac{\partial^4 y_L(x,t)}{\partial x^4} + \rho A \frac{\partial^2 y_L(x,t)}{\partial t^2} = 0 \qquad \text{(3-4)}$$

$$E_T I \frac{\partial^4 y_R(x,t)}{\partial x^4} + \rho A \frac{\partial^2 y_R(x,t)}{\partial t^2} = 0 \qquad \text{(3-5)}$$

$$I = \frac{bH^3}{12} \qquad A = bH$$

The effect of the thermal loads changes the value of the material elastic modulus E_T. The boundary conditions of the two beams can be expressed as follows:

1. No rotation occurs at the beam fixed end, and thus, $\partial y_L(0,t)/\partial x = 0$.

2. No displacement occurs at the beam fixed end, and thus, $y_L(0,t) = 0$.

3. Deflection occurs at the spring location, and thus, $y_L(l,t) = y_R(l,t)$.

4. The angular difference owing to spring rotation occurs, and thus, $\partial y_R(l,t)/\partial x - \partial y_L(l,t)/\partial x = (E_T I/k)[\partial^2 y_R(l,t)/\partial x^2]$.

Figure 3-4 shows the free body diagram of the beam section. According to this diagram,

5. The bending moment occurs at the spring location, and thus, $\partial^2 y_L(l,t)/\partial x^2 = \partial^2 y_R(l,t)/\partial x^2$.

6. The shearing force occurs at the spring location, and thus, $\partial^3 y_L(l,t)/\partial x^3 = \partial^3 y_R(l,t)/\partial x^3$.

7. No bending moment occurs at the free tip of the beam, and thus, $E_T I[\partial^2 y_R(L,t)/\partial x^2] + J_z[\partial^3 y_R(L,t)/\partial t^2 \partial x] = 0$. J_z is neglected because it is excessively small.

8. No shearing force occurs at the free tip of the beam, and thus, $E_T I[\partial^3 y_R(L,t)/\partial x^3] - m[\partial^2 y_R(L,t)/\partial t^2] = 0$.

The general solution of Equation **(3-4)** is

$$y(x,t) = Y(x)\sin(\omega t) \tag{3-6}$$

Substituting Equation **(3-6)** into Equation **(3-4)** yields Equation **(3-7)**.

$$\frac{d^4 Y(x)}{dx^4} - \beta^4 Y(x) = 0 \tag{3-7}$$

$$\beta^4 = \frac{\omega^2 \rho A}{E_T I}$$

The general solutions of Equation **(3-7)** for the left and right beams are presented as Equation **(3-8)**.

$$Y_L(x) = A_L \sin(\beta x) + B_L \cos(\beta x) + C_L \sinh(\beta x) + D_L \cosh(\beta x) \tag{3-8}$$

$$Y_R(x) = A_R \sin(\beta x) + B_R \cos(\beta x) + C_R \sinh(\beta x) + D_R \cosh(\beta x)$$

The general solution indicated in Equation **(3-8)** is introduced into the boundary conditions. Because at least one constant from A_L to D_R has non-zero solutions, according to Cramer's rule, the characteristic Equation **(3-9)** is obtained,

The value of β is obtained by solving Equation **(3-9)**. Next, Equation **(3-7)** calculates the natural frequencies of different orders for the cracked beam with an end mass.
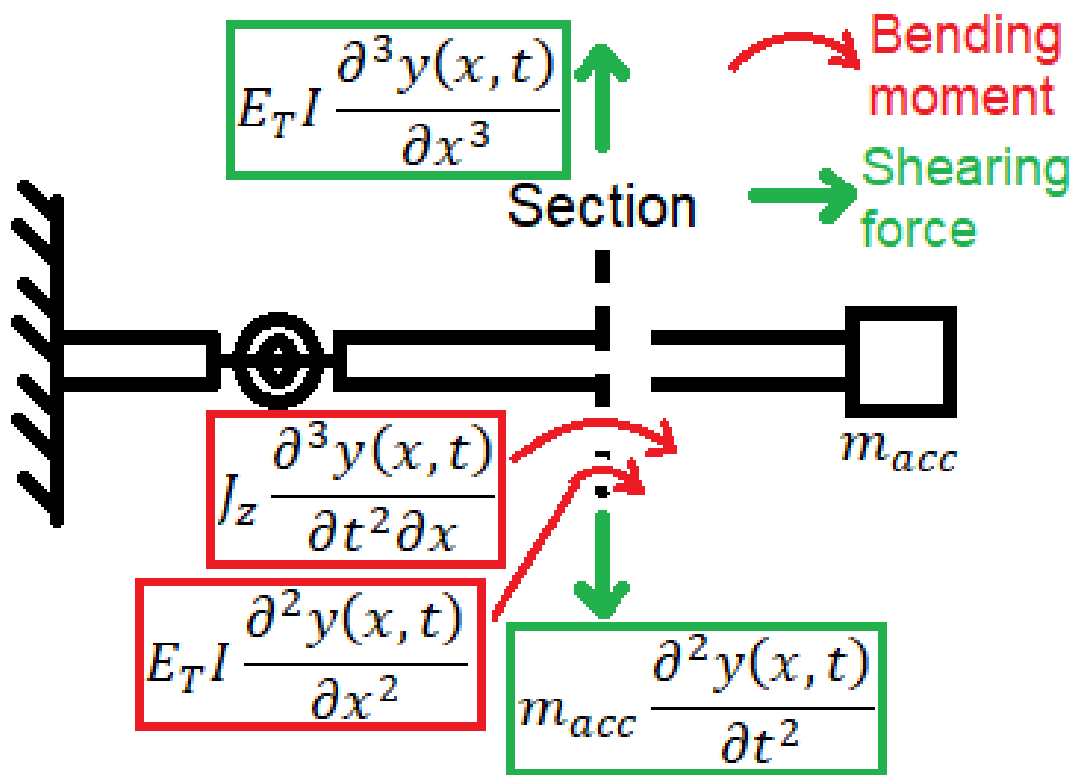
Figure 3-4 Free body diagram of a beam cross-section

$$\begin{vmatrix} 1 & 0 & 1 & 0 & 0 & 0 & 0 & 0 \\ 0 & 1 & 0 & 1 & 0 & 0 & 0 & 0 \\ \sin(\beta l) & \cos(\beta l) & \sinh(\beta l) & \cosh(\beta l) & -\sin(\beta l) & -\cos(\beta l) & -\sinh(\beta l) & -\cosh(\beta l) \\ -\cos(\beta l) & \sin(\beta l) & -\cosh(\beta l) & -\sinh(\beta l) & \cos(\beta l)+\dfrac{E_T I}{k}\beta\sin(\beta l) & -\sin(\beta l)+\dfrac{E_T I}{k}\beta\cos(\beta l) & \cosh(\beta l_L)-\dfrac{E_T I}{k}\beta\sinh(\beta l_L) & \sinh(\beta l_L)-\dfrac{E_T I}{k}\beta\cosh(\beta l) \\ -\sin(\beta l) & -\cos(\beta l) & \sinh(\beta l) & \cosh(\beta l) & \sin(\beta l) & \cos(\beta l) & -\sinh(\beta l_L) & -\cosh(\beta l) \\ -\cos(\beta l) & \sin(\beta l) & \cosh(\beta l) & \sinh(\beta l) & \cos(\beta l) & -\sin(\beta l) & -\cosh(\beta l) & -\sinh(\beta l) \\ 0 & 0 & 0 & 0 & -\sin(\beta L) & -\cos(\beta L) & \sinh(\beta L) & \cosh(\beta L) \\ 0 & 0 & 0 & 0 & -\cos(\beta L)+\dfrac{m_{acc}\beta}{\rho A}\sin(\beta L) & \sin(\beta L)+\dfrac{m_{acc}\beta}{\rho A}\cos(\beta L) & \cosh(\beta L)+\dfrac{m_{acc}\beta}{\rho A}\sinh(\beta L) & \sinh(\beta L)+\dfrac{m_{acc}\beta}{\rho A}\cosh(\beta L) \end{vmatrix}$$

$$= 0$$

(3-9)

4 ANALYTICAL MODEL FOR DISPLACEMENT RESPONSE DURING CRACK PROPAGATION

A cracked beam with different crack locations and depths exhibits different dynamic responses under forced resonance. Chapter 3 describes the establishment of the relationship between the fundamental frequency response of the beam and crack location and depth. Moreover, the displacement amplitude under the fundamental frequency is calculated in this chapter.

4.1 Beam Governing Equation of Motion

Firstly, the thesis derived the beam governing equation of motion of this system. Unlike the case of free vibrations considered in the calculation of natural frequencies, as described in Chapter 3.3, the damping effect of the beam must be considered when the beam is subjected to forced vibration. The external damping owing to the air is neglected. The equation of motion of the beam, which is derived considering the internal damping stress because of the deformation along the beam, the presence of the end mass and torsional spring, is presented as Equation **(4-1)**.

$$E_T I \frac{\partial^4 y(x,t)}{\partial x^4} + cI \frac{\partial^5 y(x,t)}{\partial x^4 \partial t} + \rho A \frac{\partial^2 y(x,t)}{\partial t^2} + m \frac{\partial^2 y(x,t)}{\partial t^2} \delta(x-L) \qquad \textbf{(4-1)}$$

$$-\frac{\partial}{\partial x}\left[k\left(\frac{\partial y_R(x,t)}{\partial x} - \frac{\partial y_L(x,t)}{\partial x} \right) \right]\delta(x-l)$$

$$-\frac{\partial}{\partial x}\left[cI\left(\frac{\partial^3 y(x,t)}{\partial x^2 \partial t} \right) \right]\delta(x-l) = 0$$

The external excitation source for the forced vibrations is represented by the displacement excitation, and thus, the force on the right-hand side of Equation **(4-1)** is 0. δ represents the Dirac delta function. To simplify the calculation, the internal damping is expressed as $c = \alpha_T E_T$ (Meirovitch, 2001).

4.2 Orthogonality of Mode Shapes for the System

The most significant element of the modelling is determining the specific orthogonality of mode shape for this system. The damping effect of the beam is

neglected in the calculation due to the free vibration. Therefore, Equation **(4-1)** can be transformed as

$$E_T I \frac{\partial^4 y(x,t)}{\partial x^4} + \rho A \frac{\partial^2 y(x,t)}{\partial t^2} + m \frac{\partial^2 y(x,t)}{\partial t^2} \delta(x-L) \tag{4-2}$$

$$+ \left[k \left(\frac{\partial y_R(x,t)}{\partial x} - \frac{\partial y_L(x,t)}{\partial x} \right) \right] \delta'(x-l) = 0$$

Based on the method of separation of variables, we can assume that the solution for Equation **(4-2)** is $y(x,t) = Y(x)q(t)$, $d^2 T(t)/dt^2 = -\omega^2 T(t)$. Substituting this solution into Equation **(4-2)** yields Equation **(4-3)** for mode i.

$$\omega_i^2 \left[\rho A Y_i(x) + m Y_{R,i}(L) \delta(x-L) \right] \tag{4-3}$$

$$= E_T I Y_i''''(x) + k \left(Y_{R,i}'(l) - Y_{L,i}'(l) \right) \delta'(x-l)$$

Equation **(4-4)** for mode j can be derived as

$$\omega_j^2 \left[\rho A Y_j(x) + m Y_{R,j}(L) \delta(x-L) \right] \tag{4-4}$$

$$= E_T I Y_j''''(x) + k \left(Y_{R,j}'(l) - Y_{L,j}'(l) \right) \delta'(x-l)$$

By multiplying Equations **(4-3)** and **(4-4)** by $Y_j(x)$ and $Y_i(x)$, respectively, and integrating each equation over the entire length of the beam, Equations **(4-5)** and **(4-6)** can be obtained:

$$\omega_i^2 \left[\rho A \int_0^L Y_i(x) Y_j(x) dx + m Y_{R,i}(L) \int_0^L Y_j(x) \delta(x-L) dx \right] \tag{4-5}$$

$$= E_T I \int_0^L Y_i''''(x) Y_j(x) dx$$

$$+ k \left(Y_{R,i}'(l) - Y_{L,i}'(l) \right) \int_0^L Y_j(x) \delta'(x-l) dx$$

$$\omega_j{}^2 \left[\rho A \int_0^l Y_i(x)Y_j(x)dx + mY_{R,j}(L) \int_0^l Y_i(x)\delta(x-L)dx \right] \qquad \text{(4-6)}$$

$$= E_T I \int_0^l Y_j{}''''(x)Y_i(x)dx$$

$$+ k\left(Y_{R,j}{}'(l) - Y_{L,j}{}'(l)\right) \int_0^l Y_i(x)\delta'(x-l)dx$$

For two arbitrary mode shapes, Y_a and Y_b, Equation **(4-7)** holds for any beam (Hassanpour et al., 2010):

$$\int_0^L Y_a{}''''(x)Y_b(x)dx \qquad \text{(4-7)}$$

$$= [Y_a{}'''(x)Y_b(x)]_0^L - [Y_a{}''(x)Y_b{}'(x)]_0^L + \int_0^L Y_a{}''(x)Y_b{}''(x)dx$$

For the considered system, Equation **(4-8)** can be derived:

$$\int_0^L Y_i{}''''(x)Y_j(x)dx = \frac{EI}{k}Y_i{}''(l)Y_j{}''(l) + \int_0^L Y_i{}''(x)Y_j{}''(x)dx \qquad \text{(4-8)}$$

By substituting Equation **(4-8)** into Equation **(4-5)** and simplifying, Equation **(4-9)** can be obtained:

$$\omega_i{}^2 \left[\rho A \int_0^L Y_i(x)Y_j(x)dx + mY_i(L)Y_j(L) \right] \qquad \text{(4-9)}$$

$$= \frac{(E_T I)^2}{k}Y_i{}''(l)Y_j{}''(l) + E_T I \int_0^L Y_i{}''(x)Y_j{}''(x)dx$$

$$+ k[Y_{R,i}{}'(l) - Y_{L,i}{}'(l)][Y_{R,j}{}'(l) - Y_{L,j}{}'(l)]$$

By performing the same treatment for Equation **(4-6)** and subtracting the results from Equation **(4-9)**, Equation **(4-10)** is obtained.

$$\left(\omega_i{}^2 - \omega_j{}^2\right)\left[\rho A \int_0^L Y_i(x)Y_j(x)dx + mY_i(L)Y_j(L) \right] = 0 \qquad \text{(4-10)}$$

Because the natural frequencies are distinct, $\left(\omega_i^2 - \omega_j^2\right)$ does not equal zero when $i \neq j$. Therefore, the mass orthogonality condition for the system is obtained, as shown in Equation **(4-11)**:

$$\rho A \int_0^L Y_i(x)Y_j(x)dx + mY_i(L)Y_j(L) = 0 \ when \ i \neq j \tag{4-11}$$

Substituting Equation **(4-11)** into Equation **(4-9)** yields the stiffness orthogonality condition for the system, as shown in Equation **(4-12)**.

$$\frac{2(E_T I)^2}{k}Y_i''(l)Y_j''(l) + E_T I \int_0^L Y_i''(x)Y_j''(x)dx = 0 \ when \ i \neq j \tag{4-12}$$

4.3 Displacement Response and Amplitude under Fundamental Frequency

As indicated in Section 3.1, one end of the cantilever beam is fixed to the excitation source, which outputs the quasi-static sinusoidal motion. This excitation drives the cantilever beam in a sinusoidal displacement under the fundamental frequency. Because the driving force varies with the displacement of the beam during vibration, the displacement of the loading source, as a form of external force, is expressed in Equation **(4-13)**,

$$u(t) = U_0 \sin(\omega_s t) \tag{4-13}$$

Therefore, the total displacement of the beam is the displacement related to the bending of the beam described in terms of the sum of the series and shaker displacement, as indicated in Equation **(4-14)** (Romaszko, Sapiński and Sioma, 2015).

$$U(x,t) = y(x,t) + u(t) \tag{4-14}$$

$$y(x,t) = \sum_{n=1}^{\infty} Y_n(x)q_n(t)$$

For ease of calculation, let $c = \alpha_T E_T$. Substituting Equation **(4-14)** into Equation **(4-1)** yields Equation **(4-15)**.

$$\sum_{n=1}^{\infty}[E_TIY_n''''(x)q_n(t)] + \sum_{n=1}^{\infty}[\alpha_T E_TIY_n''''(x)q_n'(t)] + \rho A\sum_{n=1}^{\infty}[Y_n(x)q_n''(t)]$$

$$+ \rho Au''(t) + \sum_{n=1}^{\infty}[mY_n(L)q_n''(t)\delta(x-L)] + mu''(t)$$

$$- k\left\{\sum_{n=1}^{\infty}[Y_{R,n}'(x) - Y_{L,n}'(x)]q_n(t)\right\}\delta(x-l)$$

$$- \alpha_T k\left\{\sum_{n=1}^{\infty}[Y_{R,n}'(x) - Y_{L,n}'(x)]\,q_n'(t)\right\}\delta(x-l) = 0$$

(4-15)

By multiplying Equation **(4-15)** by $Y_i(x)$ and integrating over the entire length of the beam, according to the orthogonality conditions of the system, as described in Section 4.2, Equation **(4-16)** can be obtained:

$$C_1 q_i''(t) + C_2 q_i'(t) + C_3 q_i(t) = C_4 \omega_s^2 \sin(\omega_s t) \qquad \textbf{(4-16)}$$

$$C_1 = \rho A\int_0^L Y_i^2(x)dx + mY_i^2(L)$$

$$C_2 = \alpha_T\left\{\int_0^L E_TI[Y_i''(x)]^2 dx + \frac{2(E_TI)^2}{k}[Y_i''(l)]^2\right\}$$

$$C_3 = E_TI\int_0^L [Y_i''(x)]^2 dx + \frac{2(E_TI)^2}{k}[Y_i''(l)]^2$$

$$C_4 = (\rho A + m)U_0\left[\int_0^L Y_i(x)dx\right]$$

Equation **(4-16)** is a differential equation in terms of $q_n(t)$ and a unique homogeneous solution exists for it. This solution is calculated because the cracked cantilever beam vibrates in a steady state during the test. The solution of Equation **(4-16)** can be expressed as Equation **(4-17)**:

$$q_i(t) = C_5\sin(\omega_s t) + C_6\cos(\omega_s t) \qquad \textbf{(4-17)}$$

Substituting Equation **(4-17)** into Equation **(4-16)** yields Equation **(4-18)**.

$$\left[(\omega_s{}^2 C_1 - C_3)C_5 + C_2\omega_s C_6 + C_4\omega_s{}^2 \right] \sin(\omega_s t) \tag{4-18}$$
$$= \left[(\omega_s{}^2 C_1 - C_3)C_6 - C_2\omega_s C_5 \right] \cos(\omega_s t)$$

Considering the arbitrariness of time, the joint cubic equation, Equation **(4-19)**, can be obtained for parameters C_5 and C_6:

$$\begin{cases} (C_3 - \omega_s{}^2 C_1)C_5 - C_2\omega_s C_6 = C_4\omega_s{}^2 \\ \quad C_2\omega_s C_5 + (C_3 - \omega_s{}^2 C_1)C_6 = 0 \end{cases} \tag{4-19}$$

The solutions are presented as Equation **(4-20)**.

$$C_5 = \frac{(C_3 - \omega_s{}^2 C_1)C_4\omega_s{}^2}{(\omega_s{}^2 C_1 - C_3)^2 + (C_2\omega_s)^2} \tag{4-20}$$

$$C_6 = \frac{-C_2 C_4 \omega_s{}^3}{(\omega_s{}^2 C_1 - C_3)^2 + (C_2\omega_s)^2}$$

By substituting Equations **(4-17)** and **(4-20)** into Equation **(4-14)**, the displacement response of the cracked cantilever beam can be determined.

Because the displacement amplitude of the beam is measured under the forced vibration of the fundamental frequency, the response of the higher-order modes at the fundamental frequency is omitted, and only the first-order mode is considered. The displacement amplitude at the beam tip is expressed as in Equation **(4-21)**.

$$U_{max} = \sqrt{Y_i(L)^2\left(C_5{}^2 + C_6{}^2\right) + U_0{}^2} \quad (i = 1) \tag{4-21}$$

4.4 Mathematical Approximation of the Displacement Amplitude

The analytical solution for the beam tip displacement amplitude at first-order resonance, as described in Section 4.3, involves certain limitations.

The torsion spring model is used to represent the crack depth, as described in Section 3.2. In this model, the spring stiffness is a fixed value for a specific crack depth. The crack is always fully opened, regardless of the position and the movement of the beam. However, in practice, the constantly vibrating beam

subjects the crack tip to cyclic tensile and compressive loads, as shown in **Figure 4-1**. Therefore, the actual crack depth of the beam constantly varies. The crack is fully opened when the crack tip is subjected to tensile stress for half a cycle, and at this point, the torsion spring model can represent the crack. However, the beam can be considered as an intact beam, and the crack is fully closed when the crack tip is subjected to compressive stresses for another half cycle.
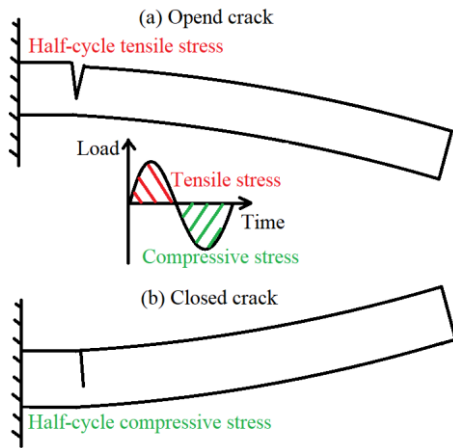
Figure 4-1 Load conditions at the crack tip in one cycle. (a) The crack, subjected to tensile stress, is opened in half a cycle, and the crack grows. (b) The crack, subjected to compressive stress, is closed in the other half cycle, and the crack propagation is terminated.

This time-dependent actual effective crack depth affects the structural response of the beam. In particular, the displacement amplitude of the actual beam lies between those of an intact beam and a fully opened crack beam. However, this phenomenon cannot be represented by the time-independent torsion spring model. Therefore, the analytical model presented in Section 4.3 is bound to be inaccurate compared to the actual situation. In Section 4.4, a modified mathematical model, as shown in Equation **(4-22)**, is considered to reduce this error.

$$U_{max,modified} = \sqrt{\frac{4\left(U_{max,a=0}{}^2 - U_0{}^2\right)\left(U_{max}{}^2 - U_0{}^2\right)}{\left(\sqrt{U_{max,a=0}{}^2 - U_0{}^2} + \sqrt{U_{max}{}^2 - U_0{}^2}\right)^2} + U_0{}^2}$$

(4-22)

The term $4\left(U_{max,a=0}{}^2 - U_0{}^2\right)\left(U_{max}{}^2 - U_0{}^2\right)/\left(\sqrt{U_{max,a=0}{}^2 - U_0{}^2} + \right.$

$\left.\sqrt{U_{max}{}^2 - U_0{}^2}\right)^2$ represents the displacement amplitude related to the bending

of the beam. The form of the term is similar to the bilinear natural frequency of a breathing crack (Douka & Hadjileontiadis, 2005). In the previous paper, the bilinear frequency can be approximated by combining the fundamental frequency of the intact beam and the fully open cracked beam with the representation $2\frac{\omega_0\omega_c}{\omega_0+\omega_c}$. So similarly, Equation **(4-22)** attempts to represent the actual displacement amplitude of a cracked beam by combining displacement amplitudes for the two extreme states of the beam.

The effect of the term is shown in **Figure 4-2**, assuming a displacement amplitude ranging from 2 mm to 32 mm for the original analytical model. The red curve shows the corrected mathematical model value. The minimum and maximum analytical displacement amplitude are 2 mm, occurring with long crack and 32 mm with initial micro crack, respectively. Equation **(4-22)** allows the value of 2 mm to dominate the corrected displacement amplitude when the actual displacement amplitude approaches 2 mm, and vice versa.

After the analytical modelling between dynamic response and crack propagation, Chapter 5 proposes a method to approximate the relationship between the dynamic response and corresponding stress conditions at the crack tip.
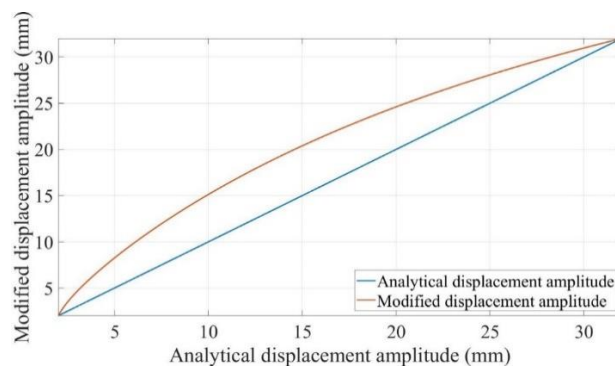
Figure 4-2 Analytical displacement amplitude and corresponding modified mathematical displacement amplitude for a range of 2 mm to 32 mm

5 RELATIONSHIPS BETWEEN THERMO-MECHANICAL LOADS AND DYNAMIC RESPONSE

5.1 Calculation of Stress at Crack Tip by Dynamic Response

This research has considered the dynamic thermo-mechanical loads as a working condition for this structure. The effect of thermal loads on crack tip stress can be directly represented by the temperature-dependent elastic modulus E_T, which is the same as crack propagation modelling in Chapters 3 and 4. As for the dynamic mechanical loads, it results in different structural displacement amplitude. Therefore, the stress conditions at the crack tip can be calculated by displacement amplitude at the beam tip for the cantilever beam.

The SIF can be calculated by Equation **(5-1)** for mode I fracture (Ostachowicz and Krawczuk, 1991). It is worth noting how to calculate the stress range $\Delta\sigma$ here. Unlike conventional quasi-static loading conditions, the stress range is time-variable due to the dynamic loads. An approximate calculation is essential. An approximate stress range should be calculated and substituted in Equation **(5-1)**.

$$\Delta K = \Delta\sigma\sqrt{\pi a}\, f\left(\frac{a}{H}\right) \tag{5-1}$$

$$f\left(\frac{a}{H}\right) = 1.13 - 1.374\left(\frac{a}{H}\right) + 5.749\left(\frac{a}{H}\right)^2 - 4.464\left(\frac{a}{H}\right)^3$$

The mean stress amplitude at the crack location can be calculated for each loading cycle by Equation **(5-2)** to Equation **(5-4)** step by step. The displacement amplitude $y_{max}(l)$ can be calculated by the analytical modelling in Chapter 4. Then, the curvature and bending moment at the crack location can be calculated by Equation **(5-2)** and Equation **(5-3)**,

$$\frac{d^2 y_{max}(l)}{dx^2} = -A_R\beta^2 \sin(\beta l) \tag{5-2}$$

$$-B_R\beta^2 \cos(\beta l) + C_R\beta^2 \sinh(\beta l) + D_R\beta^2 \cosh(\beta l)$$

$$M(l) = \left| E_T I \frac{d^2 y_{max}(l)}{dx^2} \right| ; I = \frac{bH^3}{12} \qquad \text{(5-3)}$$

Assuming the bending stress at the crack tip is constant and equal to the stress on the beam surface, so

$$\sigma(l) = \frac{6M(l)}{bH^2} \qquad \text{(5-4)}$$

The single side crack was subjected to cyclic loading of tensile and compressive stresses if the beam vibrated up and down in the fatigue test. And only tensile stress contributed to the crack propagation. Therefore, The stress range per cycle was introduced by the stress amplitude rather than the difference between peak and trough.

5.2 Summary of Analytical Modelling

The analytical interactions between thermo-mechanical loads, crack propagation, and dynamic response have been built. Following Equations are proposed,

Equation **(5-5)** represents the modified stiffness used to calculate the fundamental frequency and displacement amplitude.

The fundamental frequency can be calculated by solving Equation **(5-6)**

Equation **(5-7)** calculates the displacement amplitude at the beam tip under forced excitation.

Equation **(5-8)** calculates the stress range at crack tip dased on the beam displacement amplitude.

The MATLAB code for analytical models is shown in Appendix A.

$$k = \left(\frac{H-a}{H}\right) \times \frac{E_T b H^2}{72\pi f_r\left(\frac{a}{H}\right)}$$

(5-5)

$$\begin{vmatrix} 1 & 0 & 1 & 0 & 0 & 0 & 0 & 0 \\ 0 & 1 & 0 & 1 & 0 & 0 & 0 & 0 \\ \sin(\beta l) & \cos(\beta l) & \sinh(\beta l) & \cosh(\beta l) & -\sin(\beta l) & -\cos(\beta l) & -\sinh(\beta l) & -\cosh(\beta l) \\ -\cos(\beta l) & \sin(\beta l) & -\cosh(\beta l) & -\sinh(\beta l) & \cos(\beta l)+\frac{E_T I}{k}\beta\sin(\beta l) & -\sin(\beta l)+\frac{E_T I}{k}\beta\cos(\beta l) & \cosh(\beta l_L)-\frac{E_T I}{k}\beta\sinh(\beta l_L) & \sinh(\beta l_L)-\frac{E_T I}{k}\beta\cosh(\beta l) \\ -\sin(\beta l) & -\cos(\beta l) & \sinh(\beta l) & \cosh(\beta l) & \sin(\beta l) & \cos(\beta l) & -\sinh(\beta l_L) & -\cosh(\beta l) \\ -\cos(\beta l) & \sin(\beta l) & \cosh(\beta l) & \sinh(\beta l) & \cos(\beta l) & -\sin(\beta l) & -\cosh(\beta l) & -\sinh(\beta l) \\ 0 & 0 & 0 & 0 & -\sin(\beta L) & -\cos(\beta L) & \sinh(\beta L) & \cosh(\beta L) \\ 0 & 0 & 0 & 0 & -\cos(\beta L)+\frac{m_{acc}\beta}{\rho A}\sin(\beta L) & \sin(\beta L)+\frac{m_{acc}\beta}{\rho A}\cos(\beta L) & \cosh(\beta L)+\frac{m_{acc}\beta}{\rho A}\sinh(\beta L) & \sinh(\beta L)+\frac{m_{acc}\beta}{\rho A}\cosh(\beta L) \end{vmatrix} = 0$$

(5-6)

$$U_{max,modified} = \sqrt{\frac{4\left(U_{max,a=0}{}^2 - U_0{}^2\right)\left(U_{max}{}^2 - U_0{}^2\right)}{\left(\sqrt{U_{max,a=0}{}^2 - U_0{}^2} + \sqrt{U_{max}{}^2 - U_0{}^2}\right)^2} + U_0{}^2}$$

(5-7)

$$\sigma(l) = \frac{6M(l)}{bH^2}$$

(5-8)

6 DESIGN OF EXPERIMENTS

The analytical models proposed from Chapter 3 to Chapter 5 should be validated appropriately. The temperature-dependent elastic modulus value in analytical models was also measured. The experimental method was used for the model validation. Hence, a series of suitable experiments were designed with the consideration of dynamic thermo-mechanical load. The specific specimen geometry, selected test parameters and creative experimental setup were determined for monitoring the structural integrity and dynamic response during the dynamic fatigue crack growth test procedures.

The optimal printing parameter combination was first determined to ensure the strength and durability of the specimens used in the fatigue test. Because parameter optimization is not the main objective of this research, the related experimental work is presented in this chapter after the analytical modelling.

6.1 Geometry Design of Specimen

The geometry of one specimen which simulates the practical applications has been shown in **Figure 3-1**. Because this research evaluated both dynamic response and crack propagation, a cantilever beam structure was used in experiments rather than SEN or CT specimen as a standard. The dynamic response of the structure can be very different along with the dimensional changes. Therefore, two aspects were considered in this study to determine the size of the specimen. Firstly, the study considered the size of many actual structures in which FDM polymers were applied, including UAV and satellite antenna frames. Secondly, the size of the experimental equipment was taken into account.

ASTM D7774 is the standard test method for flexural fatigue properties of plastics. Following the standard, the specimen should be cyclically loaded equally in the positive and negative directions to specific stress or strain level at a uniform frequency until the specimen ruptures or yields. This means the quasi-static loads are applied in the test. However, high temperature values and dynamic mechanical loads were required and applied during the tests as per the

setup objectives. This means the current standard that focuses on the bending fatigue test of polymers are not suitable for the considered research problem.

6.2 Material of Specimen

ABS is the most commonly used thermoplastic polymer in FDM (Peterson, 2019). A red ABS filament fabricated by Ultimaker® was chosen for manufacturing the test specimens. More details of FDM ABS are presented in **Table 6-1**.

Table 6-1 Ultimaker® acrylonitrile butadiene styrene (ABS) filament specifications (Ultimaker, 2018)

Filament Specification	Value
Diameter	2.85 ± 0.10 mm
Tensile modulus	1618.5 MPa (ISO 527) (Anon, n.d.)
Elongation at yield	3.5% (ISO 527)
Flexural modulus	2070 MPa (ISO 178) (Anon, n.d.)
Vicat softening temperature	97 °C
Melting temperature	225–245 °C

6.3 Printing Parameters and Environmental Temperature Determination

Three significant printing parameters (i.e. raster orientation, nozzle size and layer thickness) are investigated in this research at different temperatures because prior research proposed that these parameters had the most critical effect on structural fatigue life (He and Khan, 2021). These parameters also affect the other aspects of the FDM process, such as the manufacturing time and cost.

Raster orientation: this can be defined as the path on which the nozzle moves on each layer of the FDM part. It can be set in the 3D printer's software.

Nozzle size: this determines the diameter of the filament extruded from the printer's nozzle. Different diameter nozzles can be replaced to print different specimens.

Layer thickness: this defines the height of each layer and the number of layers each part has. It can be set in the 3D printer's software.

Three values, typically used as the default setting in Cura® software, were evaluated for each parameter to cover the typical range of printing parameters. This facilitated a comprehensive evaluation of the experimental results. The raster orientation choices cover two extreme cases, where the external load and the fibre direction are parallel or perpendicular, respectively. In addition, the nozzle size and layer thickness were derived from the default profile. These values provided excellent printing quality and covered the typical setting range of the selected 3D printer. The selected values for each parameter are listed in **Table 6-2** and depicted from **Figure 6-1** to **Figure 6-3**.

Table 6-2 Printing parameters

Building Orientations	Nozzle Size (mm)	Layer Thickness (mm)
0° (X)	0.4	0.05
±45° (XY)	0.6	0.10
90° (Y)	0.8	0.15
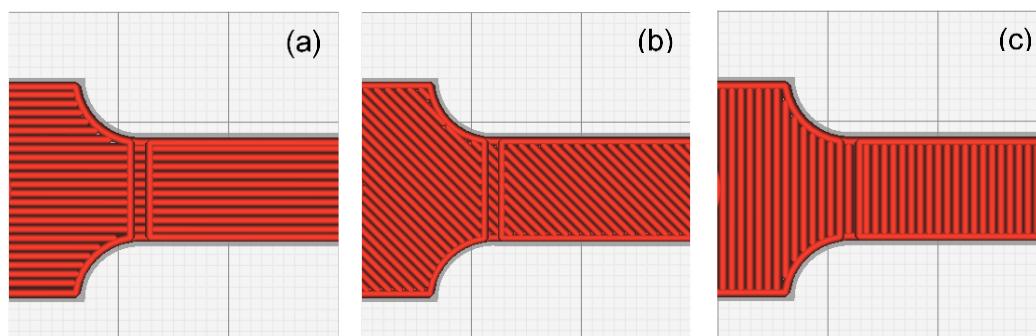
Figure 6-1 Printing directions: (a) X direction; (b) XY direction; (c) Y direction (Top-view of the beam)
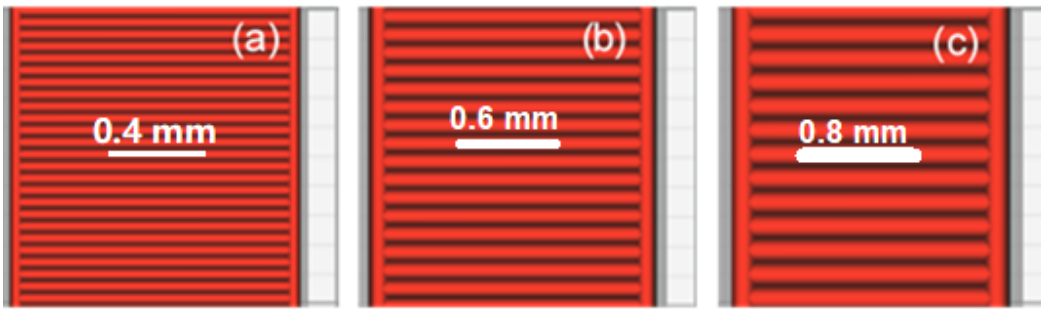
Figure 6-2 Nozzle size: (a) 0.4 mm; (b) 0.6 mm; (c) 0.8 mm. (Top-view of the beam)
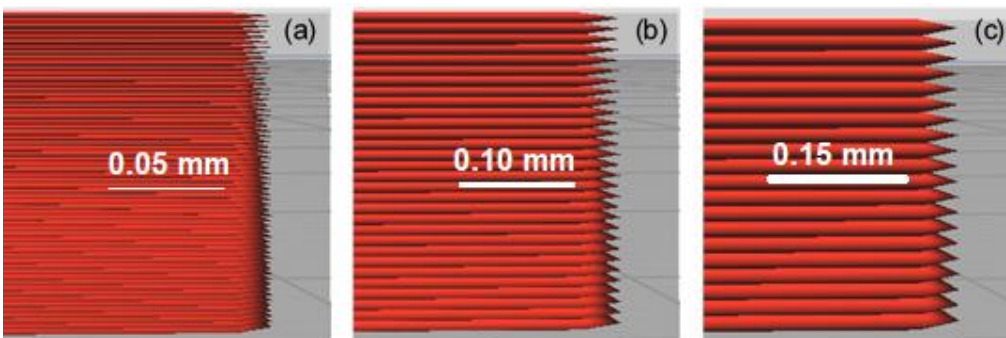
Figure 6-3 Layer thickness: (a) 0.05 mm (b) 0.10 mm (c) 0.15 mm (Side-view of the beam)

The thermal environment affects the crack propagation as the mechanical properties of ABS change a lot when the temperature changes. Therefore, three different environmental temperatures, 50, 60 and 70 °C, were selected for this purpose. 70 °C was chosen as the upper-temperature limit because ABS is sensitive to the temperature. The mechanical strength decreases when the temperature increases (Zhang, Han and Kang, 2017). The structural strength is not strong enough to support the experiment when the environmental temperature exceeds 70 °C due to softening (Baqasah et al., 2019).

6.4 Specimen Preparation and Manufacturing

The specimen geometry was designed using the CATIA v5 CAD software. An initial seeded crack with a 0.5 mm depth and 0.2 mm width was crafted close to the fixed end of the beam to ensure that the maximum stress concentration occurred at the same locations for all the specimens. Therefore, crack

72

propagation in all the experiments was the same and closely resembled fatigue failures of an actual scenario.

The CAD model was then converted to an STL file and imported to the Ultimaker CURA® 4.6 software. Apart from the selected parameters presented in **Table 6-2**, there were a series of parameters in CURA®. Because these parameters in CURA were not the focus of the thesis, all these settings were held at recommended or default values during the printing process. Further, an infill density of 100% was selected. The appropriate set nozzle temperature was selected as 245 °C based on the recommendation of the printer setup. The bed temperature was set to 90 °C, which was the default value of the printer. Finally, the Ultimaker 2+ printer printed all the specimens, as shown in **Figure 6-4** and **Figure 6-5**.
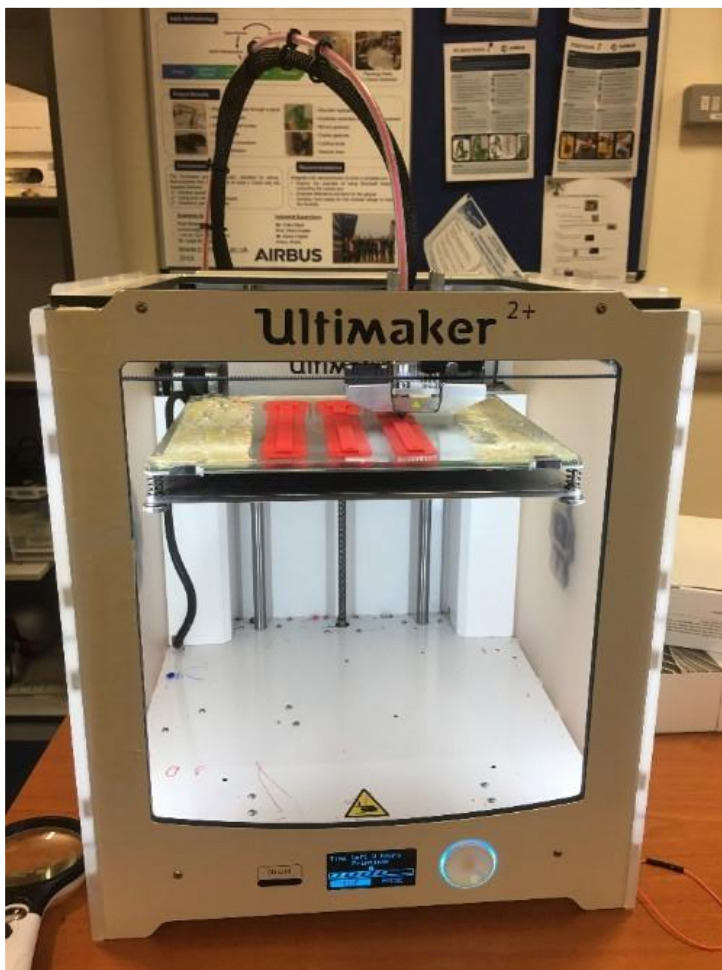
Figure 6-4 3D printing by Ultimaker 2+ printer
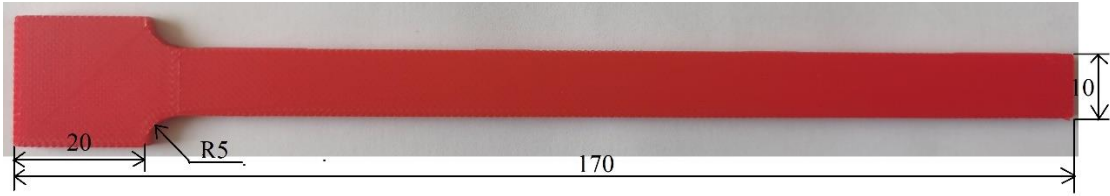
Figure 6-5 One sample printed with 0.4 mm nozzle size, XY raster orientation and 0.1 mm layer thickness (Unit: mm)

6.5 Experimental Setup

The cantilever beam structure was investigated under dynamic thermo-mechanical loads in the thesis. The bending load was considered to fill the gap proposed in Section 2.8. So the research specially developed experimental setup, which is provided in this section.

The whole experimental setup is illustrated in **Figure 6-6**. The signal generator was used to produce a sinusoidal output for the power amplifier, which transmitted the signal to a V55 shaker manufactured by Data Physics. The specimen was fixed on the shaker. The shaker can provide the excitations to the specimen with the constant displacement amplitude. It means the load on the beam was variable with the crack propagation during the test. A mica band heater was used to apply a constant thermal load on the specimens throughout the experiments. The band temperature and chamber temperature correlation was built first before the experiment. The heater band temperature was increased from 50 to 150 °C per °C/min rate. A thermocouple thermometer measured the corresponding air temperature in the band. So the correlation between the air temperature and band temperature was built.

The accelerometer was fixed on the beam's free end to measure the acceleration in real-time. The acceleration and time data acquired by the accelerometer were imported into the Signal Express software via the NI 9234 DAQ card and NI 9174 DAQ chassis and recorded. The crack depth was measured by a Dino-Lite digital microscope. The experimental flow chart is shown in **Figure 6-7**.
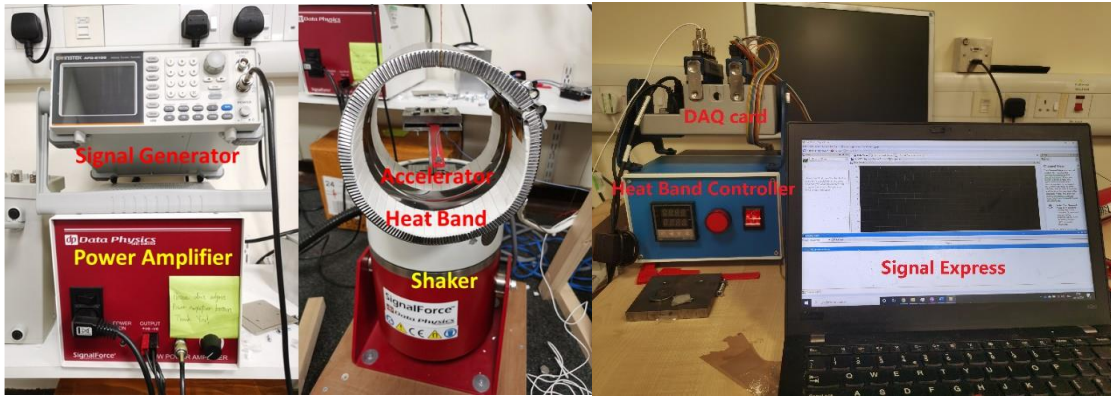
Figure 6-6 Experimental setup
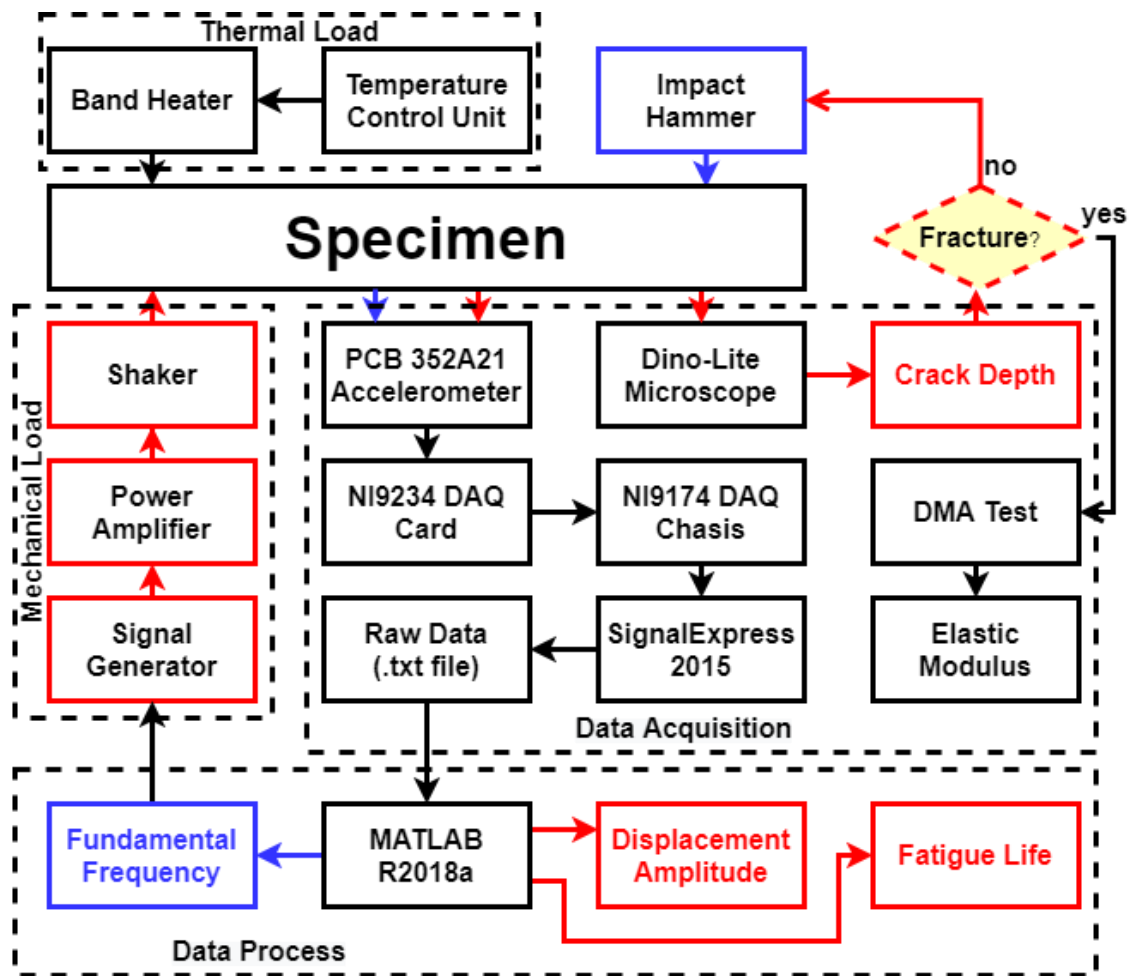
Figure 6-7 Experimental Flow Chart (Blue boxes and arrows represent the procedure for fundamental frequency measurement. Red boxes and arrows represent the procedure for fatigue crack growth test)

6.6 Experimental Scheme and Procedure

6.6.1 Optimal Printing Parameter Determination

In the experimental study, this research determined the optimal printing parameter combination. There are three printing parameters with three options, respectively, as shown in **Table 6-2**. It makes 27 combinations to print the specimens. Each combination was tested under three different temperatures, as discussed in Section 6.3. Consequently, 81 different types of specimens were tested with these parameters and the selected temperature values. Three similar specimens were manufactured for each combination and tested under the same conditions to confirm experimental repeatability. The experimental procedures are as follow.

The specimen with the pre-seeded 0.5 mm depth crack at 5 mm crack location was fixed on the shaker. Firstly, the specimen's fundamental frequency was measured three times with impact tests. The accelerometer recorded the acceleration at the beam tip with a 25600 Hz sampling rate. Then, the shaker was vibrated at 2 mm amplitude under the measured fundamental frequency. It provided the initial maximum amplitude for the beam. This implied that the beam was under resonation initially, following which the pre-seeded crack growth started. The shaker was running continuously until the beam's final fracture occurred. The accelerometer recorded the acceleration and time data during fatigue crack growth tests with a 2048 Hz sampling rate.

Compared with the typical fatigue failure criteria, which is defined as the number of cycles at which the stiffness of the material reduces by 50% (N_{f50}) (Ghuzlan and Carpenter, 2000), this experiment directly registered the number of cycles from the beginning of the run to the occurrence of fracture for the specimens because it was difficult to measure the stiffness for the cracked specimen. The results were recorded and then compared with each other. The 3D printing parameter combination corresponding to most cycles was determined as the optimal choice. The beam section after the fracture was captured using a 200× Dino-Lite microscope.

6.6.2 Dynamic Response of Cracked Beam under Selected Temperature Values

This research investigated the dynamic response for the cracked beam at different temperatures. So, It can be compared with the analytical modelling results.

The specimens tested here were manufactured with the optimal printing parameters. However, three different crack locations were tested in order to evaluate the crack location effect on dynamic response. Their distance to the fixed end of the beam was 5, 15 25 mm, respectively. The locations of the initial crack were all near the fixed end of the beam. The reason is that the bending stress increases near the fixed end, as shown in Figure 6-8. This increased bending stress makes it easier for cracks to initiate and propagate in practical situations. The initial-seeded crack led to a stress concentration, thus ensuring a consistent location of crack growth.
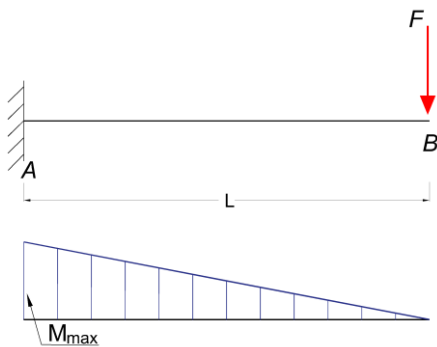
Figure 6-8 Bending moment diagram for a cantilever beam with single load at the crack tip

The experimental procedure was modified from Section 6.6.1 as follows: First, the fundamental natural frequency of the specimen was measured three times through impact tests. The mean value of the fundamental frequency was recorded. Next, the beam was driven by the shaker and vibrated at the fundamental frequency, thereby generating the initial maximum displacement amplitude of the beam. This displacement amplitude was recorded and used to examine the crack position and initial crack depth. The continuously applied

forced vibration led to crack propagation, which reduced the crack area's local stiffness and changed the complete system's dynamic response characteristics.

The experiment was paused when the displacement amplitude decreased as observed in real-time through the Signal Express software. The system's fundamental frequency was re-measured and re-recorded in addition to the new crack depth acquired from the Dino-Lite digital microscope. Subsequently, the test was restarted. The procedure was repeated until the beam reached the catastrophic failure.

6.6.3 Elastic Modulus Measurement

In order to measure the elastic modulus for different printing parameter combinations, the DMA test was conducted using the Q800 device of TA Instruments. The device measured the storage and loss moduli under different temperatures through a single-clamped cantilever beam flexural test.

The test setup is shown in **Figure 6-9**. A 50-mm-long specimen was cut from the free end of the fractured beam. The part was fixed at one end in the chamber of the DMA test machine. The temperature in the chamber gradually increased from 30 °C to 70 °C at a rate of 3 °C per minute. The free end of the specimen moved at a frequency of 1 Hz and an amplitude of 10 μm. The storage and loss moduli values, which varied with the temperatures, were automatically calculated and recorded. The phase lag between stress and strain represents the material viscosity and can be measured directly. The related formula is shown in Equation **(6-1)**. The complex modulus is calculated by the measured bending stress and corresponding beam deflection. These values were then used in analytical models and discussed in Chapter 7.1.

$$E^* = \frac{2\sigma}{\frac{d^2y}{dx^2}H} \qquad\qquad \textbf{(6-1)}$$
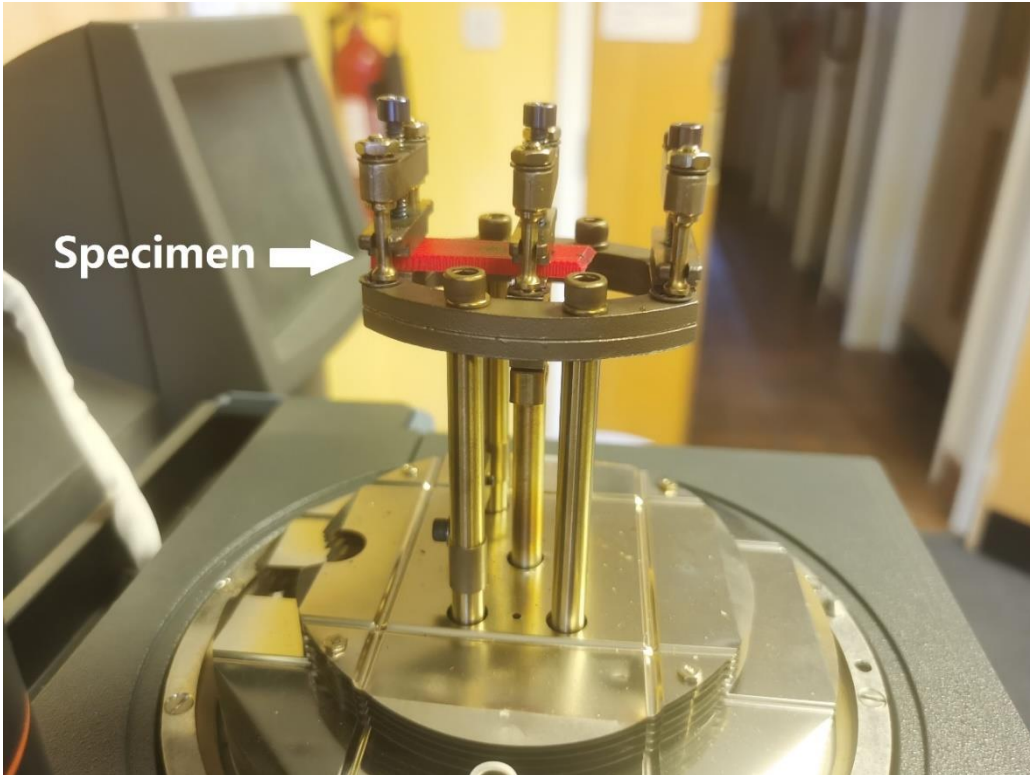
Figure 6-9 Single-clamped DMA test setup

6.6.4 Signal Processing and Raw Data Analysis

The data measured by the accelerometer were recorded in SignalExpress 2015 and saved as the .txt files. The text files, including the time and acceleration data, were imported into MATLAB R2018a for further processing. The fundamental frequency f of the specimen was calculated using Equation **(6-2)**:

$$f = \frac{i - j}{t_i - t_j}$$
(6-2)

where t_i and t_j denote the time of the i th and j th peak amplitude, respectively.

The displacement amplitude at beam free end was calculated using Equation **(6-3)**.

$$U = \frac{a_{max}}{(2\pi f)^2}$$
(6-3)

Where a_{max} is the acceleration amplitude. The MATLAB codes are shown in Appendix B.

7 DYNAMIC RESPONSE OF THE CANTILEVER BEAM– END MASS SYSTEM

7.1 DMA DATA ANALYSIS FOR ANALYTICAL MODELLING

7.1.1 Tensile Modulus of FDM ABS

The DMA of two randomly selected samples cut from the fracture beams was evaluated. The recorded data, including the storage modulus E' and loss modulus E'' are shown in **Figure 7-1**. The poly2 curve fitting method was used to model the correlation between the entities and temperature, with R-square values of 76.11% and 70.61%, respectively.
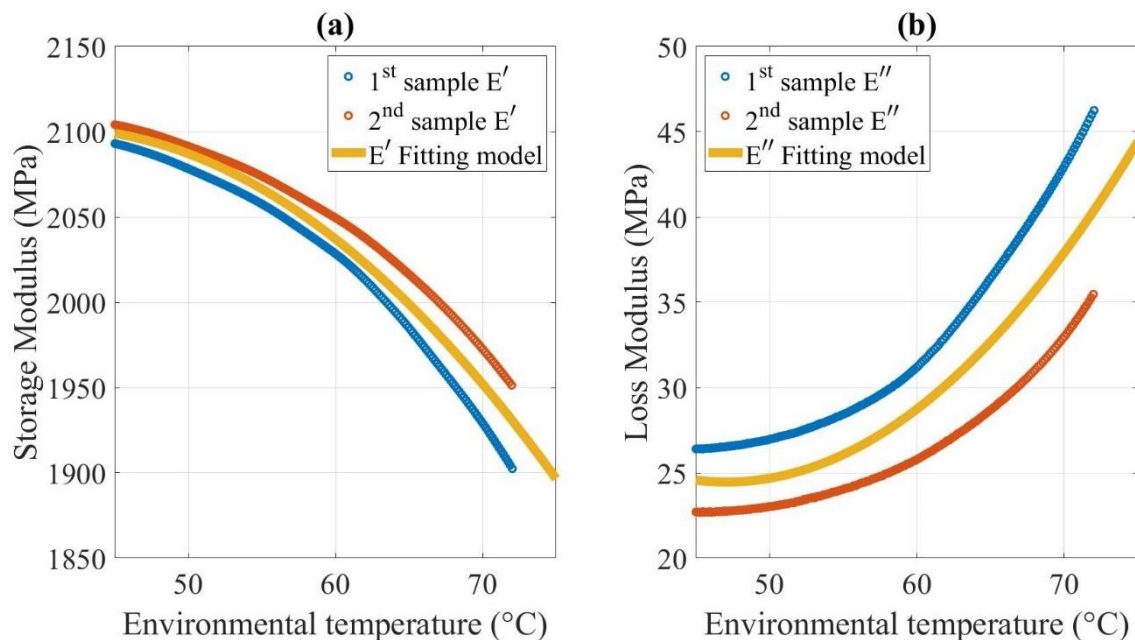
Figure 7-1 (a) Storage modulus and (b) loss modulus of FDM ABS

As illustrated in **Figure 7-1**, because thermal expansion occurs when the temperature rises, the storage modulus of FDM ABS, which represents its elastic behaviour, decreases from 2104 MPa at 50 °C to 1976 MPa at 70 °C. The decrease is more rapid as the temperature increases. This trend is similar to those exhibited by most materials (Khan et al., 2015)(Zai et al., 2020a).

The loss modulus of FDM ABS, which represents its material viscosity behaviour, exhibits an opposite trend with the temperature. Specifically, the loss

modulus increases from 24 MPa at 50 °C to 36 MPa at 70 °C. The viscosity of the FDM ABS leads to energy dissipation caused by friction and rearrangement. A higher amount of energy is lost when the temperature is higher. The tensile modulus E^* of FDM ABS, as a viscoelastic material under a thermal environment, is a complex physical entity, as shown in Equation **(7-1)** (Henriques et al., 2018).

$$E^* = E' + iE''$$ **(7-1)**

However, the loss modulus is two orders of magnitude smaller compared to the storage modulus. It is also worth noting that the loss modulus is measured at a load frequency of 1 Hz, and the beam has a fundamental frequency of over 20 Hz. Several previous studies (Akil and Zamri, 2013)(Böhning et al., 2019) proposed that the increased loading frequency increased the storage modulus. It indicates that elastic behaviour becomes dominant, whereas the influence of the viscous behaviour is diminished, indicated by the concomitant decrease in dynamic viscosity. Therefore, the effect of viscosity can be neglected in this research. In other words, the FDM ABS can be treated as an elastic material in the considered temperature range. The value of the storage modulus is equal to the tensile modulus of FDM ABS. The trend of the tensile modulus with temperature is consistent with the empirical model shown in Equation **(7-2)** (Liu and Liu, 2014).

$$E = E_0 - BTe^{-\frac{T_0}{T}}$$ **(7-2)**

7.1.2 Damping of the FDM ABS Cantilever Beam

Damping reduces oscillation amplitude due to the dissipated energy to overcome friction or other resistance forms (Meirovitch, 2001). Generally, two types of viscous damping occur for beams: resistance of the external medium (e.g. air, water) to the motion of the beam, known as external damping; and the distributed damping stresses that occur along with the height of the beam section owing to the repeated deformation of the beam fibres, known as internal damping (Xu and Ma, 2007). This thesis ignored the effect of external damping and considered only the internal damping owing to the fibre friction of the beam

in the considered conditions. As described in Section 4.1, the internal damping is numerically equal to the loss modulus.

Furthermore, the damping behaviour of FDM ABS can be represented using the structural damping coefficient or loss factor $\tan \delta$, which equals E''/E'. Because the loss modulus increases with the temperature and the storage modulus exhibit the opposite trend, $\tan \delta$ always increases as the temperature rises. Specifically, $\tan \delta$ increases from 0.01143 at 50 °C to 0.0183 at 70 °C, as shown in **Figure 7-2**. In terms of the microstructure, the energy dissipation in the viscoelastic layers generated by their shear deformation causes internal damping. Molecular chain slippage occurs easily among the layers, and thus, a larger amount of energy is dissipated as heat by the friction when the temperature rises.
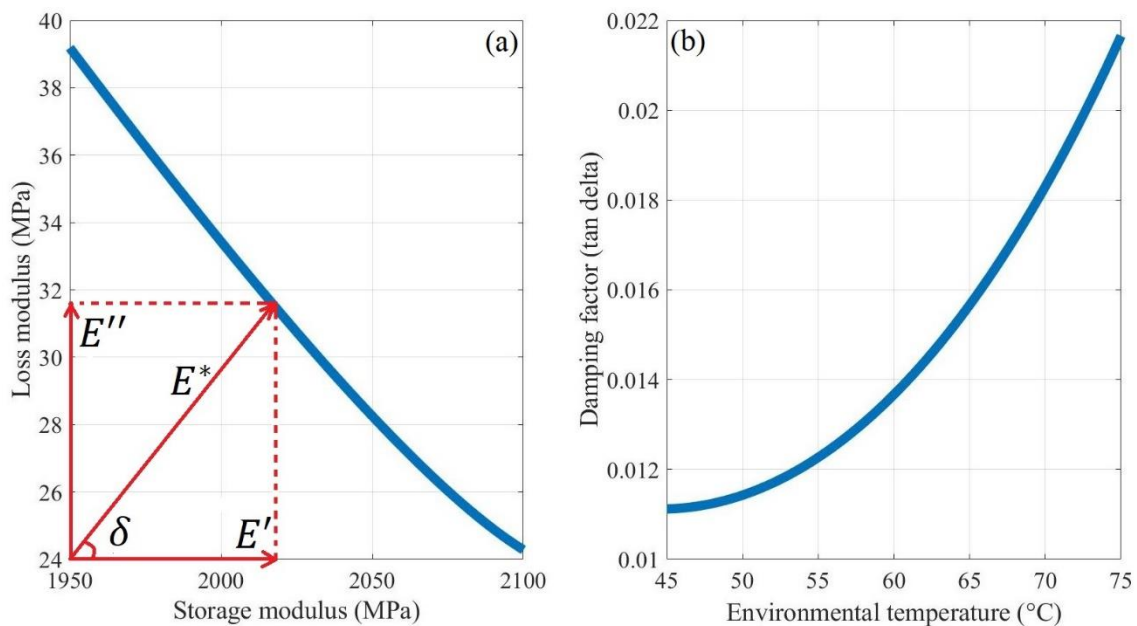
Figure 7-2 (a) Visualised relationship among the storage modulus, loss modulus, and damping factor. (b) Change in the damping factor with temperature

Owing to the increased damping factor at higher temperatures, the FDM ABS cantilever beam stores less kinetic and elastic potential energy under forced vibration when subjected to the same external force, resulting in a smaller displacement amplitude. This phenomenon was also observed in the experiments.

7.2 Comparison of Analytical Models with Differently Modelled Torsional Spring Stiffness Values

Crack propagation tests were conducted for beams with different crack locations and temperatures, as described in Section 6.6.2. The analytical models for the dynamic response were developed with the original and modified stiffness values. The DMA results shown in **Figure 7-1** were considered as the elastic modulus values in the analytical model under different temperatures. The fundamental frequency of the beam is plotted in **Figure 7-3**. **Figure 7-4** shows the analytical displacement amplitude at the beam tip during crack propagation. The pictures of crack propagation until the fracture is shown in **Figure 7-5**. The Dino-Lite digital microscope accurately captured the crack and automatically calculated the crack length based on the known thickness of the beam (3mm). Furthermore, the alternating light and dark printing layers can also be used to calibrate crack length measurements.
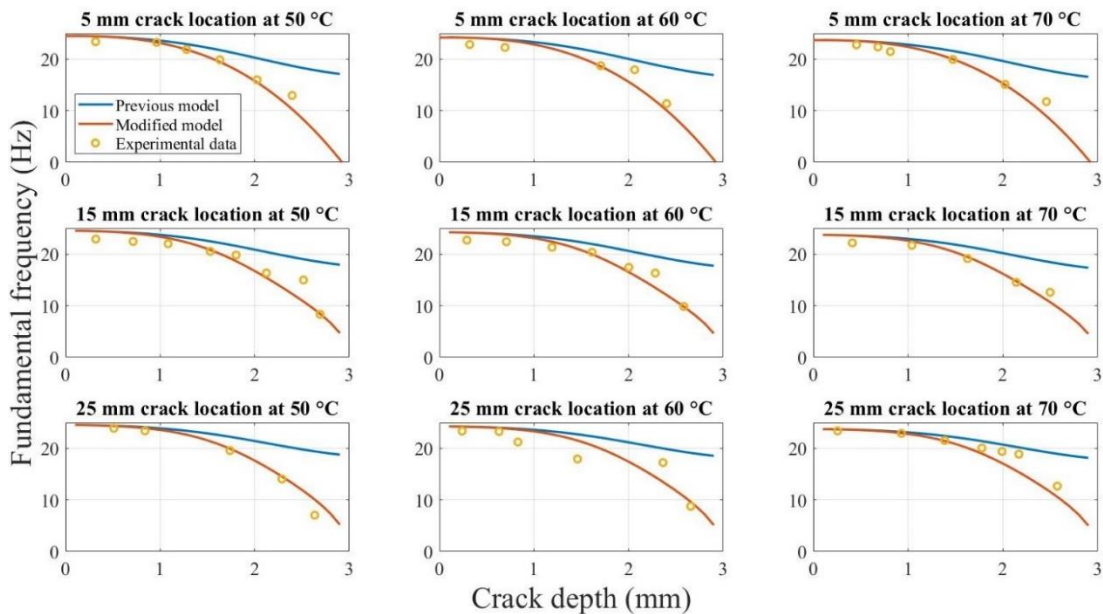
Figure 7-3 Fundamental frequencies obtained experimentally and calculated using two analytical models during crack propagation
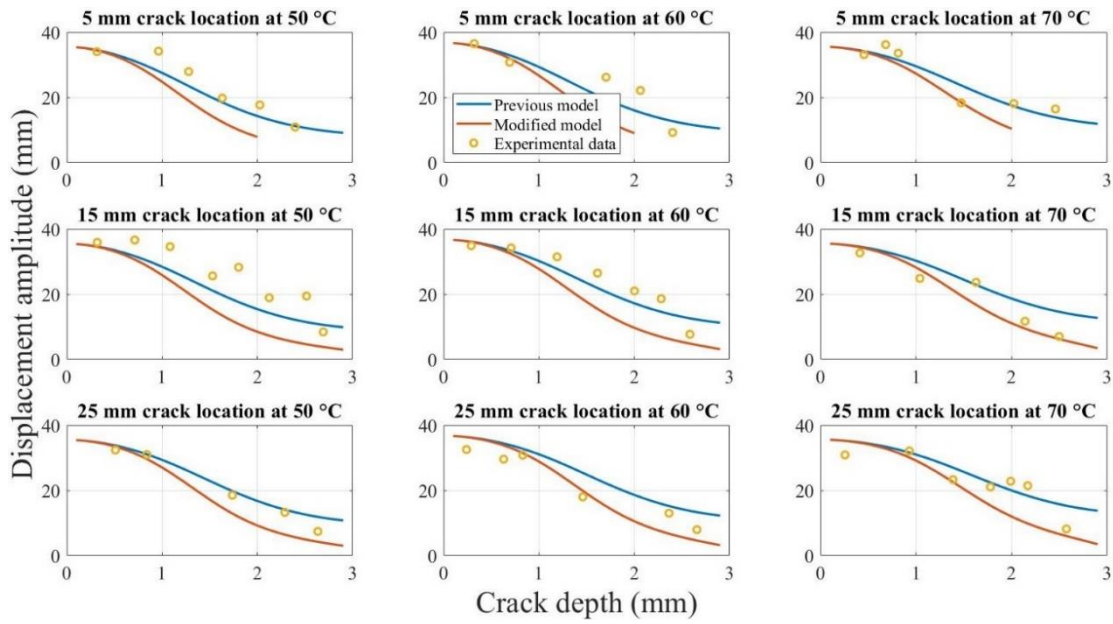
Figure 7-4 Analytical displacement amplitudes obtained experimentally and calculated using two analytical models during crack propagation
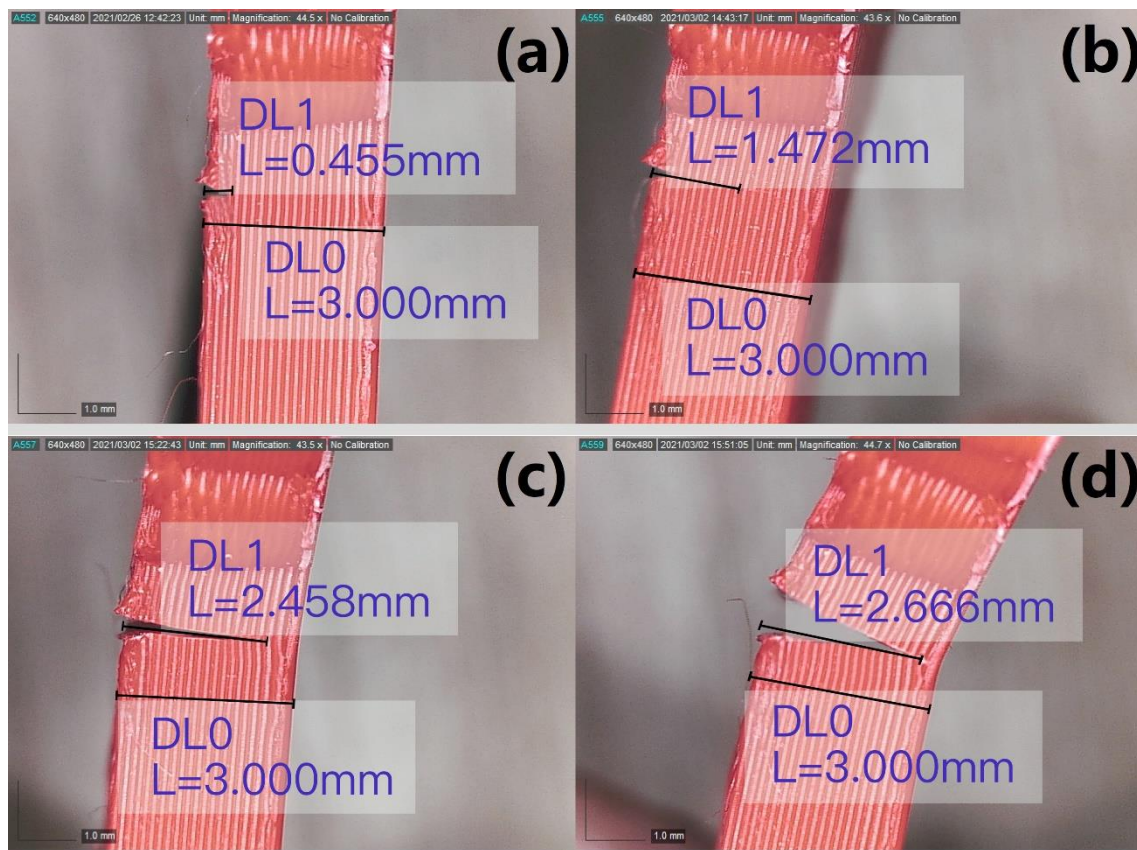
Figure 7-5 Crack depth at 5 mm crack location at 70°C during dynamic fatigue crack growth test (a) 0.455 mm. (b) 1.472 mm. (c) 2.458 mm. (d) 2.666 mm

The approximate calculated values could not attain the target accuracy because MATLAB R2018a reached the set maximum number of intervals in some cases when the crack depth exceeded 2 mm at the 5 mm crack location. It is due to the existence of high frequency and amplitude functions in solutions. The integral() function in MATLAB, which works at double-precision accuracy, cannot follow the rate of change during the integration process, resulting in an inaccurate value. Therefore, in order to avoid these wrong values, based on the analytical results for the crack depth ranging from 0 to 2 mm, the fitted curves were plotted for the fundamental frequency when the crack depth ranged between 2 mm and 3 mm.

7.2.1 Comparison and Analysis of Differences in the Fundamental Frequency

Figure 7-3 shows the experimental data and fundamental frequency calculation results of the two analytical models during crack propagation at different crack locations under different temperatures. The experimental data and calculations of the two analytical models highlight a continuous decrease in the fundamental frequency with the initial crack propagation until specimen fracture. This result is similar to that reported previously (Baqasah et al., 2019).

However, the comparison of the results of the fundamental frequency calculations based on the two analytical models indicates that when the crack depth approaches the beam top surface (less than one-third of the total thickness of the beam), the fundamental frequency calculated using both models is identical. Notably, as the crack depth continues to increase, the fundamental frequency curve for the original spring stiffness model tends to level off, whereas that for the modified spring stiffness model decreases rapidly and tends to decrease more rapidly with the increase in the crack depth. For example, in the case of the crack growth at an ambient temperature of 50 °C and crack location of 5 mm, the difference in the fundamental frequency obtained using the two models changes from 0.00036 Hz at a 0 mm crack depth to 0.44 Hz at a 1 mm crack depth and finally to 14.61 Hz for a 2.8 mm crack depth. In terms of the percentage, relative to the original stiffness model, the

difference between the two models increases rapidly from 0.001% to 84% as the crack depth increases from 0.1 mm to 2.8 mm, corresponding to nearly five orders of magnitude.

This difference in the fundamental frequency as the crack growth can be attributed to the use of the spring model of the crack size, as described in Section 3.2. In the original modelling process of the spring stiffness, it was assumed that the stresses at the surface of the bending beam crack location and stress field at the crack tip were of the same magnitude. This estimation is applicable only for shallow cracks close to the surface of the beam. As the crack depth increases, the error in the stresses increases larger. Even when the beam is completely fractured, the original spring stiffness model still estimates a non-zero value, whereas, in reality, the spring stiffness model must yield a value of zero. In the proposed spring stiffness model, the additional term $(H - a)/H$ is introduced, which ensures that the stiffness coefficient of the spring tends to zero when the beam is completely fractured. Therefore, the fundamental frequency of the fractured beam is 0 Hz, consistent with the actual scenario.

The comparison of the results of the analytical models with the experimental data indicates a significant difference in the accuracy of the predicted values of the two models, especially at large crack depths. As shown in **Figure 7-3**, the experimental data are further distributed along the curves of the fundamental frequency value obtained using the modified model.

To examine the difference quantitatively, **Figure 7-6** shows the relative differences of the two spring stiffness models against the experimental data. In terms of the fundamental frequencies for different crack locations at different temperatures, the overall difference between the values obtained using the original model and experimental data is considerably greater than pertaining to the modified model.
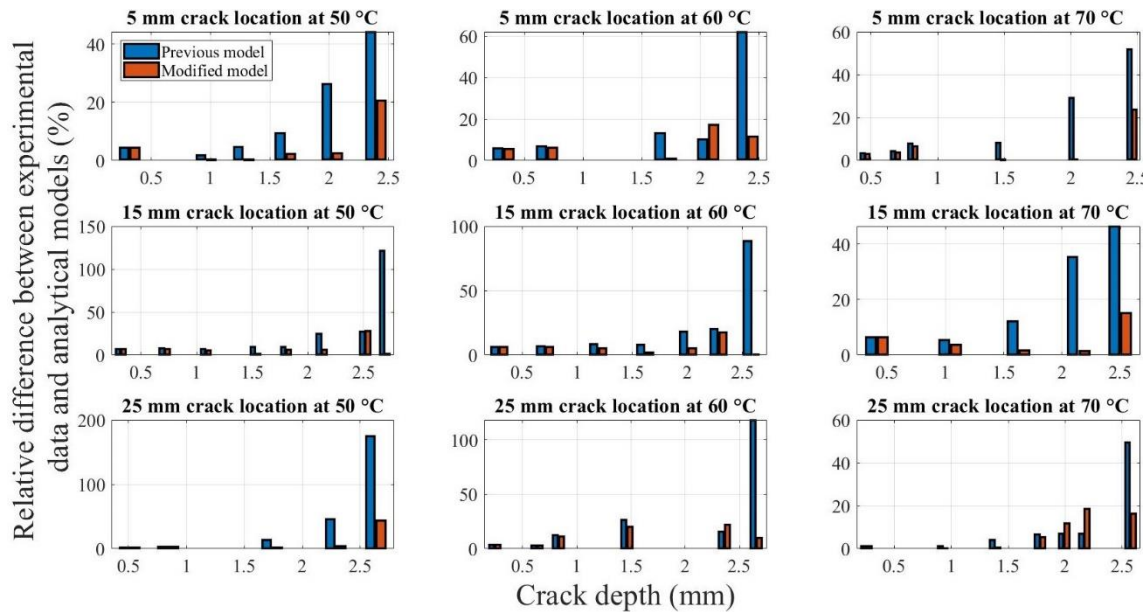
Figure 7-6 Relative difference in the results obtained using analytical models and experimental results

Moreover, the difference in the fundamental frequency with crack growth is similar in the conditions corresponding to each subplot. An example of crack propagation under 50 °C at the 5 mm crack location is considered. **Table 7-1** summarizes the experimental data, corresponding analytical model calculation results, and differences associated with the crack depth measured during the crack propagation test. **Figure 7-7** shows the relative difference between the results obtained using the two analytical models and experimental results. **Table 7-1** and **Figure 7-7** highlight the increasing difference between the fundamental frequencies calculated using the original model and the experimental data during the crack propagation. The difference reaches nearly 40% when the crack depth is 2.396 mm.

In contrast, the fundamental frequencies determined using the modified model are in agreement with the experimental data, with a difference of less than 5% when the crack propagates from the initial depth of 0.317 mm to 2.026 mm. The difference in the fundamental frequency corresponding to crack depths of 0.963 mm and 1.279 mm is only 0.08% and 0.07%, respectively. Note that in order to determine the analytical model fundamental frequency at a crack depth of 2.396 mm, a second-order polynomial fit was used as the accuracy yielded by the

MATLAB approach was inadequate; the use of this approach likely led to the slightly higher discrepancy (20.55%) between the value and the experimental data.

Overall, the modified model yielded fundamental frequency values that were similar to the experimental data. Compared to the original model, accurate estimates of the fundamental frequency response of the beam could be obtained for specific crack locations and depths. However, the limitations of the actual structure in the experiment led to the insufficient validation of the model. Since the fragile cracked area is not sufficient to support the self-weight of the beam as it approaches fracture, the fractured part of the beam has almost no dynamic response. It resulted in the acceleration sensor at the tip of the beam not collecting valid experimental data and, therefore, cannot be compared with our analytical model. This limitation on model validation is also reflected in the displacement amplitude. Experimental validation is not feasible when a/H exceeds approximately 85%.

In the following discussion of the frequency response of the cracked beam, only the fundamental frequency determined using the modified model is considered.

Table 7-1 Fundamental frequency obtained from experiments and analytical models, along with the difference in the values

Crack depth (mm)	0.317	0.963	1.279	1.632	2.026	2.396
Experimentally obtained fundamental frequency f_{test} (Hz)	23.39	23.26	21.88	19.88	15.99	12.96
Fundamental frequency f_1 (Hz) obtained using the original model	24.44	23.66	22.91	21.76	20.19	18.7
Fundamental frequency f_2 (Hz) obtained using the modified model	24.42	23.27	21.9	19.42	15.59	10.3

Difference between f_{test} and f_1 (Hz)	1.04	0.4	1.03	1.88	4.2	5.74
Difference between f_{test} and f_2 (Hz)	1.03	0.018	0.014	0.46	0.4	2.66
Difference between f_{test} and f_1 (%)	4.47	1.72	4.72	9.46	26.27	44.26
Difference between f_{test} and f_2 (%)	4.42	0.08	0.07	2.33	2.49	20.55
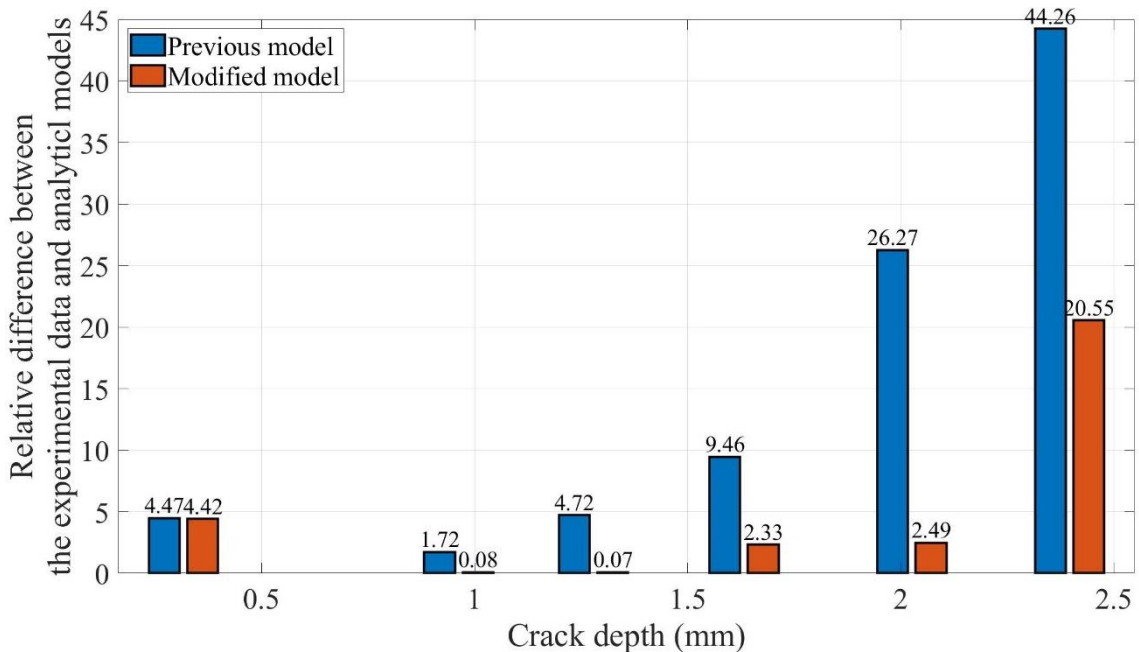
Figure 7-7 Relative difference between the fundamental frequency obtained using the two analytical models and experimental data for crack propagation at the 5 mm crack location at 50 °C

7.2.2 Comparison and Analysis of the Differences in the Displacement Amplitude

Figure 7-4 shows the analytical and experimental relationships between the beam tip displacement amplitude and crack depth at first-order resonance. As in the case of **Figure 7-3**, both the analytical model results and experimental data indicate that the displacement amplitude decreases as the crack grows.

The difference in the results obtained using the two analytical models is not significant when the crack is close to the surface of the beam. However, as the crack propagates, the difference between the two values becomes progressively larger, and the displacement amplitude determined using the modified model decreases more rapidly than that obtained using the original model. Eventually, the value of the modified model is significantly smaller than the displacement amplitude of the original model when the beam is completely fractured. The results are similar to those of the fundamental frequency during crack propagation for similar reasons. The additional term $(H - a)/H$ in the proposed model ensures that the local stiffness at the crack location is smaller than that pertaining to the original model. Therefore, the beam oscillates similarly to the shaker vibration without displacement due to resonated bending when the beam approaches fracture. Therefore, the displacement amplitude is similar to 2 mm, as in the case of the shaker, when the crack depth increases to 3 mm. Consequently, the proposed model with the modified torsional spring stiffness is superior to the original model.

However, the results of the proposed analytical model are significantly different compared to the experimental data. The experimental data are consistent with the theory described in Section 4.4. The torsion spring model is not an ideal representation of the actual effective crack depth, which varies with time during the same cycle. Therefore, a new mathematical model was proposed in Section 4.4. **Figure 7-8** shows the displacement amplitudes obtained using the analytical methods and experiments at different crack depths.

As the crack approaches the beam surface, the displacement amplitude obtained using the analytical and modified model is similar. The difference between the two models gradually increases as the crack depth approaches the half beam thickness. Furthermore, the displacement amplitudes obtained using both models gradually converge to the same value, which equals the shaker's vibration amplitude of 2 mm, when the beam is about to fracture. This difference can be attributed to the form of Equation **(4-22)**. The nature of this equation causes the displacement amplitude of the modified model to be greater than

that of the analytical model when the crack depth approaches the middle of the beam.
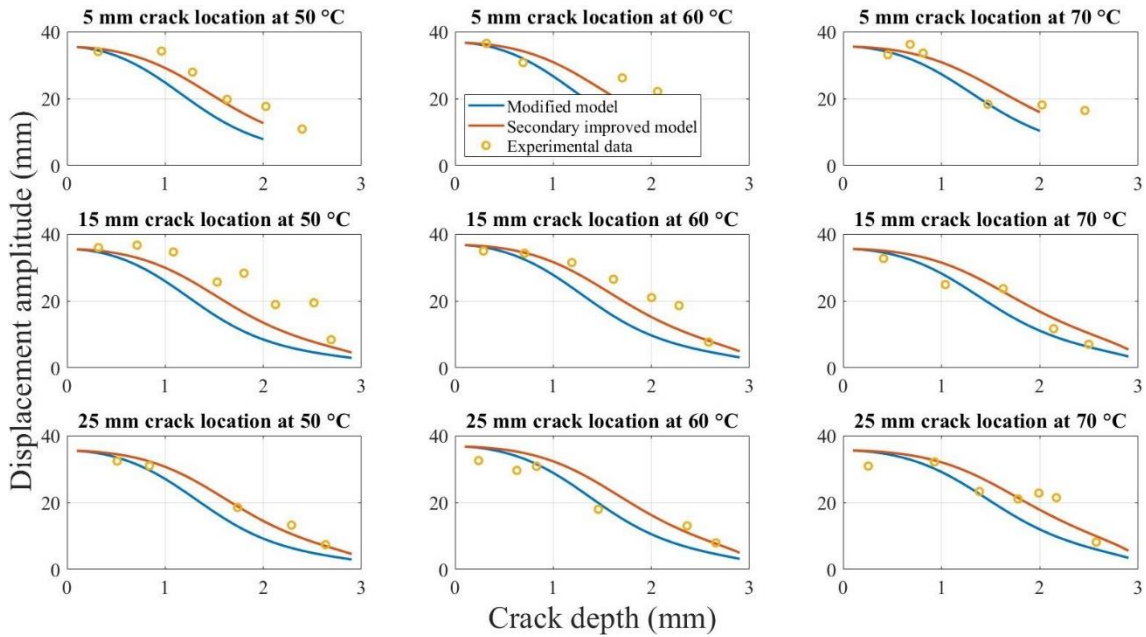
Figure 7-8 Displacement amplitudes obtained using the analytical methods and experiment during crack propagation

Figure 7-9 shows the average relative difference between the modified and secondary improved models compared to the experimental data for different combinations of the crack location and temperatures. The difference between the results of the secondary improved model and experiment is smaller than that for the modified model. **Figure 7-10** illustrates the difference between the results obtained using the two models and the measured values corresponding to the crack depth during crack propagation tests. The modified model calculation is closer to the actual experimental values for most crack depths at different crack locations under different temperatures.

However, both **Figure 7-8** and **Figure 7-10** show that the experimental values are higher than the displacement amplitude obtained using the modified model at specific crack depths, especially when the crack depth is between the half and total thickness of the beam (for instance, in conditions of 15 mm 50 °C and 5 mm 60 °C). This observation can be attributed to the crack closure phenomenon. To ensure that the displacement amplitude of the shaker output

to the fixed end of the beam is a constant value of 2 mm during the experiment, the load amplitude on the beam varies with time. The load applied to the beam to make it resonate decreases as the crack grows. The reduced load reduces the stress amplitude on the crack location, resulting in a lower stress ratio. This low stress ratio leads to more significant crack closure during beam vibration. Although the vibrated cracked beam can be assumed as a superposition of the intact and fully open cracked beam states, a larger crack closure renders the structural properties of the cracked beam to be more biased towards the intact beam. Therefore, expectedly, the displacement amplitude response of the beam tends to increase owing to the larger influence of the intact beam.
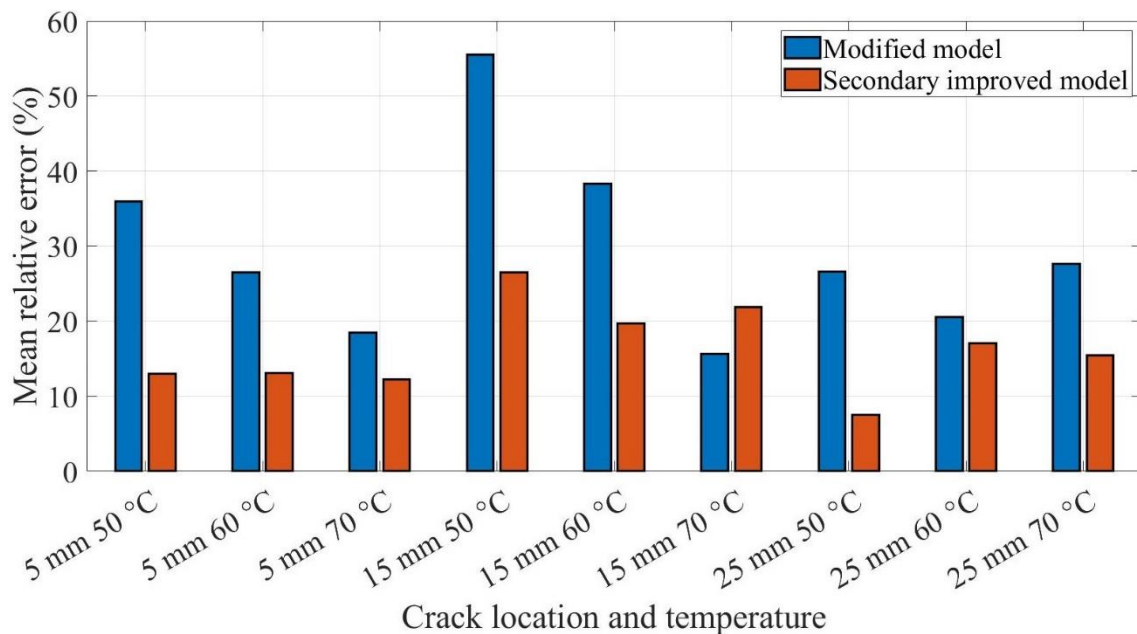
Figure 7-9 Mean relative difference for different combinations of the crack locations and temperatures

Nevertheless, the difference in the fundamental frequency obtained using the analytical model and the experimental data is considerably smaller than that for the displacement amplitude, as shown in **Figure 7-6** and **Figure 7-10**. This phenomenon can be attributed to two aspects. First, different experimental methods were used to measure the fundamental frequency and displacement amplitude. The beam was at rest when the fundamental frequency was measured. The impact test only applied a slight disturbance to the beam.

However, the beam was required to be in resonance with a 2 mm excitation to measure the displacement amplitude. This considerable resonance likely affected the crack growth and changed the displacement amplitude. Moreover, the fluctuating displacement amplitudes during beam vibration led to an increased measurement error. Second, the heating band was unlike an environmental chamber and was relatively exposed. The vibration of the beam caused air to flow, leading to fluctuations in the ambient temperature of the specimen, thereby affecting the displacement amplitude.
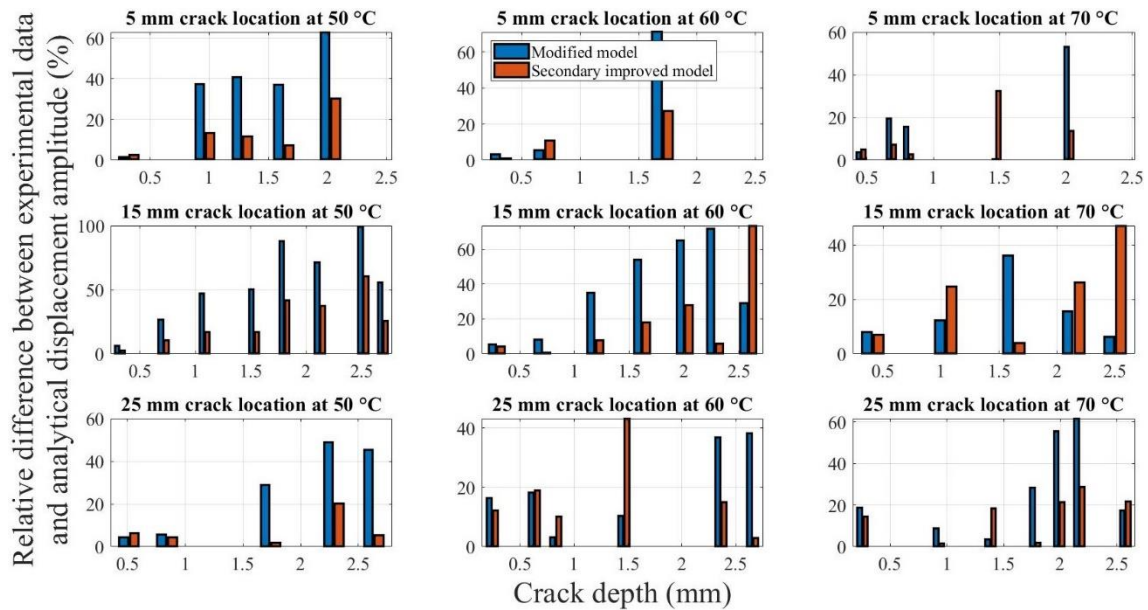
Figure 7-10 Relative difference between models and experimental data during crack propagation

7.3 Fundamental Frequency for the Cracked Beam

7.3.1 Influence of the Crack Depth on Natural Frequencies

The variation in the beam fundamental frequency during crack propagation is shown in **Figure 7-3**. The two analytical models and experimental data yield similar trends for the change in the fundamental frequency with the crack depth. The relationship between the crack growth and change in fundamental frequency at an ambient temperature of 50 °C at a 5 mm crack location is considered for analysis. **Figure 7-11** illustrates the fundamental frequency and drop percentage change during crack growth, as determined using the

analytical model and experimental data. As described in Section 7.2.1, the experimental data and analytical model indicate the reduction in the fundamental frequencies as the crack grows. Compared to an intact 3-mm-thick beam, the fundamental frequency at a crack depth of 2.8 mm drops from approximately 24.5 Hz to 2.5 Hz, which is only approximately 10% of the initial fundamental frequency. The beam's cross-sectional area at the crack location decreases, and the local stiffness decreases as the crack length increases. As reflected in the analytical model, the local reduction in the stiffness due to crack growth reduces the stiffness matrix, although the beam mass does not change; therefore, the calculation yields a gradual reduction in the fundamental frequency.
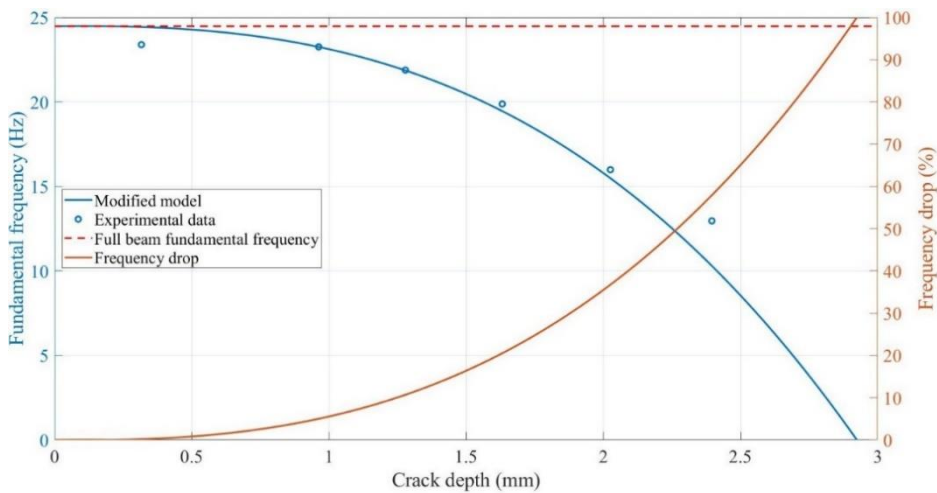
Figure 7-11 Change in frequency during crack propagation at the 5 mm crack location at 50 °C

Notably, the change in the fundamental frequency is insignificant when the crack is close to the surface. However, as the beam approaches fracture, the change in the fundamental frequency becomes more rapid as the crack grows. The frequency decreases only by approximately 0.3 Hz (1% relative change) when a crack of 0.5 mm (one-sixth of the beam thickness) is present in the intact beam; in contrast, the frequency decreases by approximately 6 Hz (25% relative change) from the 2.5 mm crack depth to fracture. The initial monitoring of small cracks is crucial in actual working conditions. In other words, highly

sensitive sensors are required to predict the crack depth when using the fundamental frequency.

7.3.2 Influence of the Crack Location on the Fundamental Frequency

Figure 7-12 shows the change in the fundamental frequency during crack propagation for a beam with different crack locations at different temperatures. A crack located farther from the fixed end of the beam corresponds to a higher fundamental frequency of the beam. Moreover, the difference in the fundamental frequencies increases. However, as the crack depth approaches the thickness of the specimen (from approximately 2.3 mm, as shown in **Figure 7-12**), the fundamental frequencies of the beams with different crack locations rapidly converge to 0 Hz. The effect of the crack location on the fundamental frequency is not significant. The maximum difference in the fundamental frequencies for the 15 mm and 25 mm crack locations is only approximately 0.95 Hz.
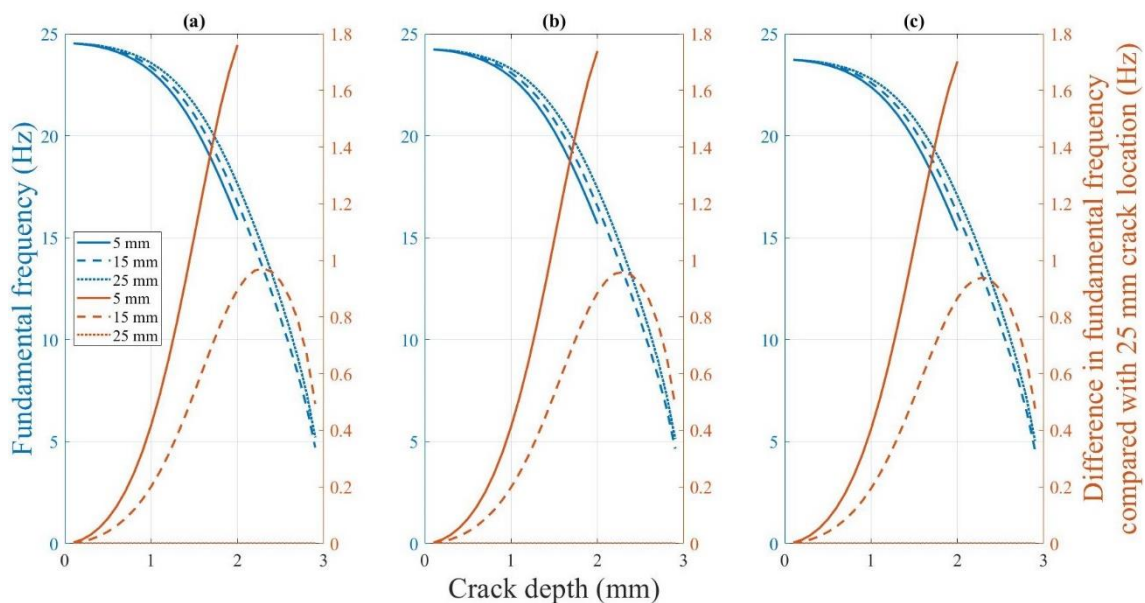
Figure 7-12 Difference in the fundamental frequency with crack locations: Crack propagation at (a) 50 °C (b) 60 °C (c) 70 °C.

7.3.3 Influence of the Temperature on the Fundamental Frequency

Figure 7-13 shows the fundamental frequency of the cracked beam at different temperatures. The fundamental frequency of a specimen with a fixed crack

depth and location decreases gradually as the temperature increases. However, the difference in the fundamental frequency at different temperatures decreases as the crack depth increases. Similar to the crack location, the effect of the temperature on the fundamental frequency is not significant. Regardless of the crack location, the fundamental frequency of specimens with a 0.1 mm crack depth differs only by 0.8 Hz in the experimental temperature range. This difference decreases further with crack propagation to a theoretical value of 0 Hz at the final fracture state.
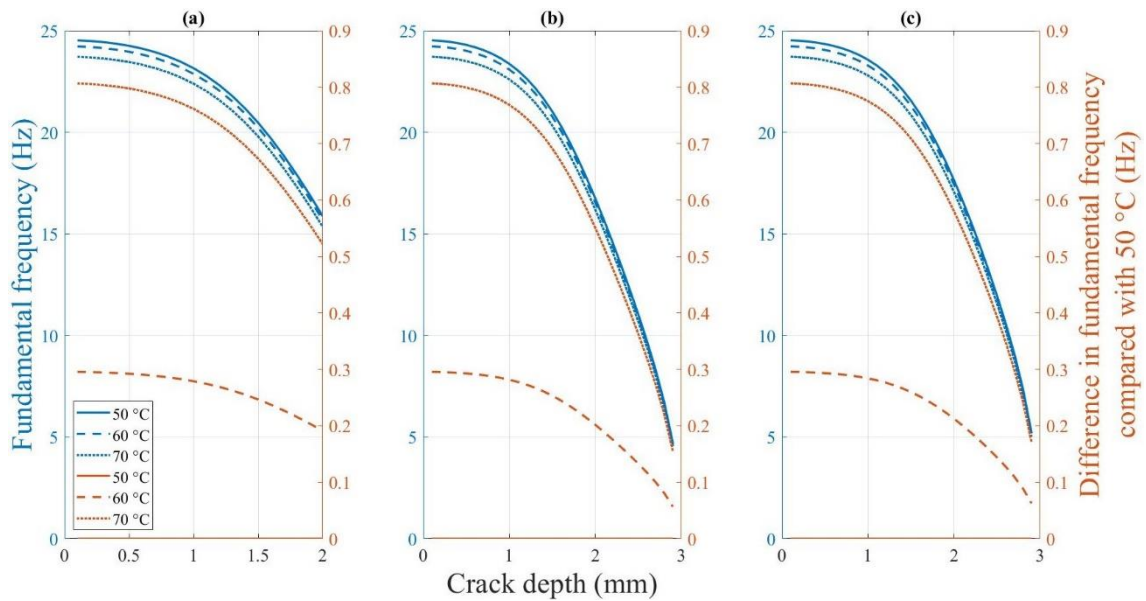
Figure 7-13 Difference in the fundamental frequency of the beams under different temperatures at a crack location of (a) 5 mm (b) 15 mm (c) 25 mm

7.4 Displacement Amplitude for the Cracked Beam under Resonance

7.4.1 Influence of the Crack Depth on the Displacement Amplitude

As the trends of the displacement amplitude of the specimens at different crack locations during crack propagation are similar, as shown in **Figure 7-8**, the displacement amplitude of the beam with a 15 mm crack location at 60 °C is discussed only.

Figure 7-14 shows the change in the displacement amplitude with crack growth. The displacement amplitude decreases from approximately 36 mm for

the initial intact specimen to 5 mm at the final near-fracture state. The change in the displacement amplitude is smooth as the crack depth approaches the beam top surface or when the beam is close to fracture. However, the displacement amplitude decreases rapidly when the crack depth approaches half the thickness of the beam.
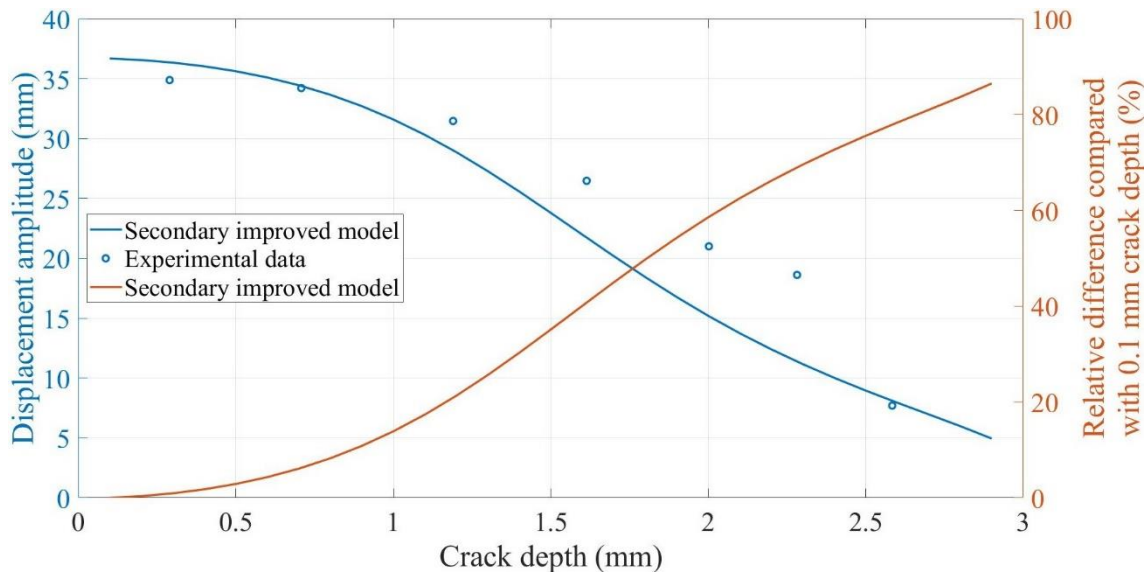
Figure 7-14 Change in the displacement amplitude for crack growth at a 15 mm crack location at 60 °C

The decrease in the displacement amplitude of the beam with the crack growth can be attributed to two reasons: First, the load to maintain the 2 mm displacement amplitude excitation gradually decreases as the crack propagates. In other words, the force acting on the beam gradually decreases. The decreased excitation results in smaller displacement amplitudes. Second, the increased crack depth increases the damping of the beam (Kharazan, Irani and Noorian, 2020). Consequently, the energy dissipated by damping increases during vibration, and the displacement amplitude decreases, too.

7.4.2 Influence of the Crack Location on the Displacement Amplitude

Figure 7-15 shows the change in the amplitude with crack growth for beams with different crack locations. Similar to the frequency trend shown in Section 7.3.2, a crack located farther from the fixed end of the beam corresponds to a smaller displacement amplitude. The displacement amplitude of the beam is the

same for different crack locations when the crack is close to the surface of the beam and propagation is initiated. Moreover, the displacement amplitudes tend to be 2 mm when the beam fractures.
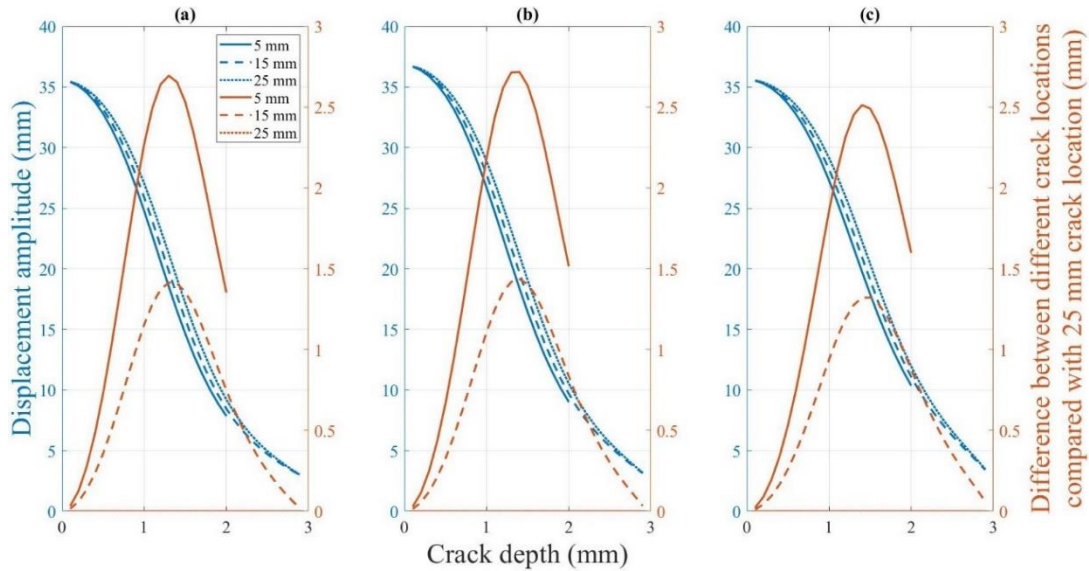
Figure 7-15 Difference in the displacement amplitude for a beam with different crack locations, with crack propagation at (a) 50 °C (b) 60 °C (c) 70 °C.

However, unlike the fundamental frequency change, the displacement amplitude difference corresponding to different crack locations increases as the crack depth closes to half the beam thickness (approximately 1.4 mm).

7.4.3 Influence of the Temperature on the Displacement Amplitude

Figure 7-16 shows the effect of the temperature on the displacement amplitude of the cracked beam. Unlike all previous response trends, the effect of different temperatures on the displacement amplitude of cracked beams is extremely complex. As shown in **Figure 7-16**, the beam has the smallest displacement amplitude from the intact to fractured state at 50 °C. The intact beam exhibits the largest displacement amplitude at 60 °C. However, when the crack depth reaches and exceeds approximately 0.8 mm, the beam at 70 °C exhibits the largest displacement amplitude.

This seemingly random phenomenon validates the experimental results of the existing research (Baqasah et al., 2019). Specifically, this phenomenon can be

attributed to the combined effect of the varied elastic modulus and excitation loads under various temperatures. The overall flexibility of the beam decreases, and the displacement amplitude naturally increases when the beam is subjected to the same external excitation when the temperature rises. However, the fundamental frequency pertaining to the rise in temperature decreases. To maintain the 2 mm amplitude resonance, both the amplitude and frequency of the external forces loaded on the beam decrease, thereby reducing the displacement amplitude of the beam. These two opposing influences cause the final displacement amplitude response of the beam to lose its monotonicity and become more complex.
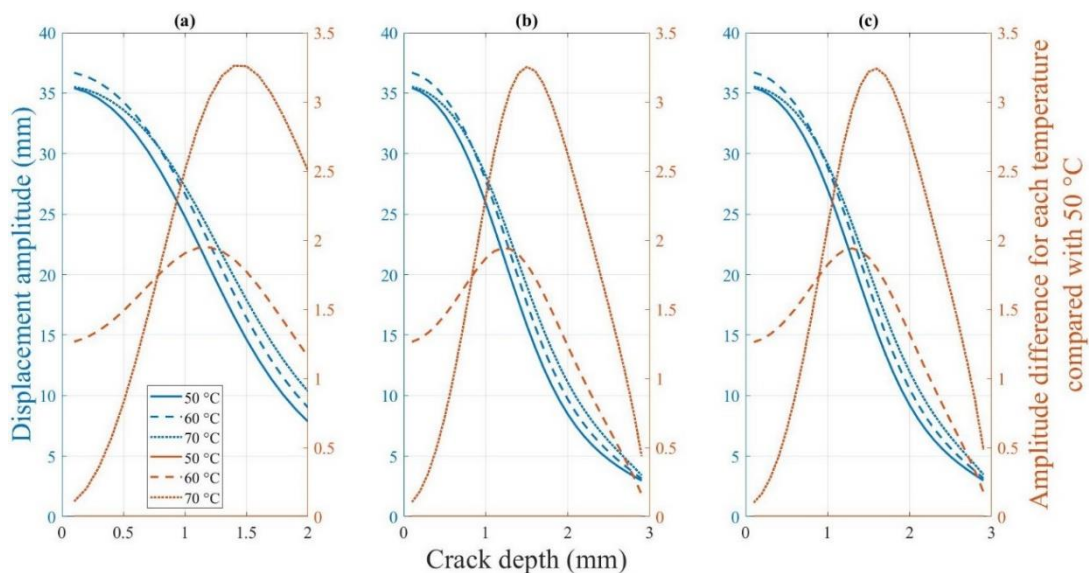
Figure 7-16 Difference in the displacement amplitude for the cracked beam under different temperatures at crack locations of (a) 5 mm (b) 15 mm (c) 25 mm

7.5 Sensitivity of the Dynamic Response

Section 7.3 and 7.4 discussed the response characteristics of the fundamental frequency and displacement amplitude. This section describes the characteristics and sensitivity of the dynamic response to the crack depth and location. Notably, the response of the displacement amplitude to different temperatures, as described in Section 7.4.3, is too complex to comprehend.

7.5.1 Sensitivity of the Dynamic Response to the Crack Depth

Because the structural dynamic response trends at different crack locations and temperatures during crack propagation are similar, as shown in **Figure 7-3** and **Figure 7-8**, the dynamic response of the beam with a 15 mm crack location at 60 °C is discussed.

Figure 7-17 shows the fundamental frequency and displacement amplitude change at the beam tip for a beam with a 15 mm crack location at 50 °C. Although both the fundamental frequency and displacement amplitude decrease with crack growth, their trends and differences from the initial values are different.
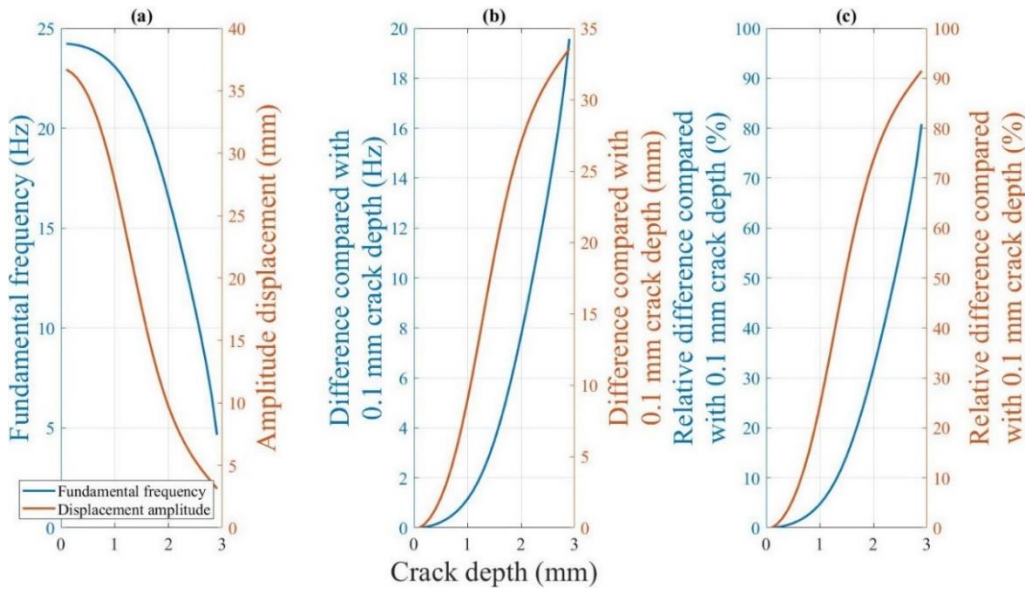
Figure 7-17 (a) Dynamic response of the beam during crack growth at a 15 mm crack location at 60 °C (b) Difference in the dynamic response with that for a 0.1 mm crack depth. (c) Percentage difference in the dynamic response with that for a 0.1 mm crack depth.

Figure 7-17 (b) shows that the fundamental frequency of the beam changes by only approximately 1 Hz, although the displacement amplitude of the beam decreases by 8 mm when the crack depth of the beam increases from 0.1 mm to 1 mm. In other words, a significant change occurs in the displacement amplitude of the beam, whereas the change in the fundamental frequency is extremely small at the beginning of the crack growth when the crack is close to

the beam surface. **Figure 7-17** (c) shows that compared to the initial value, the relative difference in the displacement amplitude is always higher than that in the fundamental frequency for the same crack depth throughout the process from an intact state to the final fracture.

Therefore, the displacement amplitude is more sensitive to changes in the crack depth than the fundamental frequency response of the fractured beam in the early stages of crack growth. In reality, the detection of small initial cracks is extremely critical. The accurate prediction of initial cracks can often prevent the catastrophic failure of the structure even if the cracks continue to grow. This finding suggests that using the displacement amplitude to estimate the crack depth yields more accurate results than those obtained using the fundamental frequency for small cracks. In other words, the accuracy requirements for the sensor can be lowered if the displacement amplitude is measured. The fundamental frequency and displacement amplitude can be analysed in combination for longer cracks to determine the crack depth accurately.

7.5.2 Sensitivity of the Dynamic Response to the Crack Location

Figure 7-18 shows the fundamental frequency and displacement amplitude change for beams with 15 mm and 25 mm crack locations. The crack location moves away from the fixed end of the beam. The fundamental frequency and displacement amplitude of the beam decrease.

Figure 7-18 (b) shows the difference in this decreasing trend. The displacement amplitude is the most sensitive to the crack location when the crack depth is close to approximately 1.4 mm. The change in the fundamental frequency is greatest when the crack position changes from 15 to 25 mm at a crack depth of approximately 2.3 mm.

Figure 7-18 (c) illustrates the relative difference in the fundamental frequency and displacement amplitude. The relative differences of the two dynamic responses for different crack locations are minor in the early stages of crack growth. However, a 1% difference in the displacement amplitude is considerably more significant than a 0.17% difference in the fundamental frequency for a 0.5

mm crack depth when the crack location changes from 15 mm to 25 mm. Furthermore, throughout the crack growth, the slopes of the displacement amplitude curve are greater than those of the fundamental frequency when the crack depth is less than 2.3 mm.
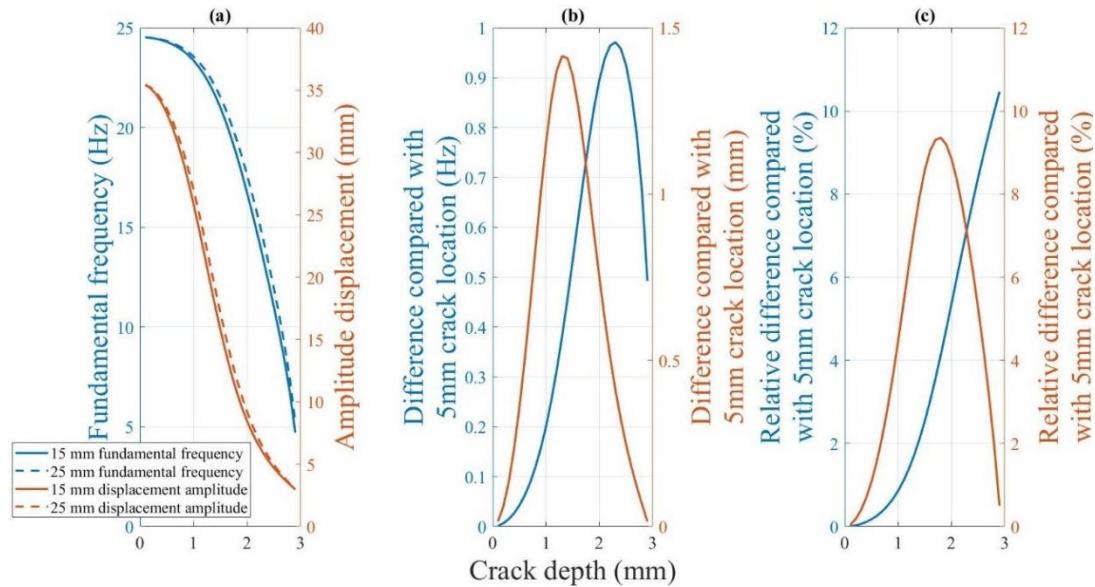
Figure 7-18 (a) Difference in the dynamic responses of the beam with 5 and 15 mm crack locations at 60 °C. (b) The difference in the dynamic responses. (c) The relative difference in the dynamic response corresponding.

In other words, similar to the crack depth, the displacement amplitude is more sensitive to the crack location than the fundamental frequency at the critical stage of early crack growth and for most crack depths. Therefore, using the difference in the displacement amplitude to determine the crack location may yield superior results than those obtained using the fundamental frequency.

8 3D PRINTING PARAMETER EFFECT ON FATIGUE LIFE OF FDM STRUCTURE UNDER THERMO-MECHANICAL LOADS

Before the experiments evaluating the dynamic response, this research investigated the effect of 3D printing parameters on the fatigue performance of the structure firstly, which achieved the fourth objective shown in Section 1.4. The determined optimal printing parameters from the tests were used to manufacture the specimens for later model validation. However, to retain the continuity of the modelling and validation, it was decided to provide the details of optimisation at the end.

8.1 DMA Tests Results

The storage modulus of each specimen cut from the cracked cantilever beams at a temperature ranging from 50 to 70 °C was also measured by DMA. The statistical significance was determined using MATLAB. A Kruskal–Wallis one-way analysis of variance (Kruskal–Wallis test) with three independent variables (building orientation, nozzle size and layer thickness) was conducted without considering temperature because the data group did not meet the normal distribution requirement. Each printing parameter group contained the sample data, which was the constant in that parameter, but with the different values in other parameters. This tested the hypothesis that the storage modulus of different parameters were equal against the alternative hypothesis that at least one group was different from the others.

The variation of the storage modulus with temperature and statistical data is depicted in **Figure 8-1** and **Figure 8-2**. The mean storage moduli for different printing parameters are listed in **Table 8-1**. Although calculating the mean storage modulus was not the primary purpose of this study, this value can be used as a reference since it significantly affects the performance of structural fatigue. Higher storage modulus means higher stiffness. It may potentially lead to longer fatigue life.

As can be observed, the storage modulus consistently decreased with the increase in temperature during the DMA test for all the specimens. This is similar to other materials (Baqasah et al., 2019; Khan et al., 2015; Zai et al., 2020a). For the mean storage modulus under the different printing parameter settings, the X orientation provided the highest mean storage modulus, 1692 MPa. The mean storage modulus for the specimen with the Y orientation was only 1561 MPa. The XY building orientation between these two orientations had a mean storage modulus of 1616 MPa. The variation in the storage modulus was similar to that reported in previous studies (Afrose et al., 2014; Rankouhi et al., 2016; Riddick et al., 2016; Schirmeister et al., 2019).
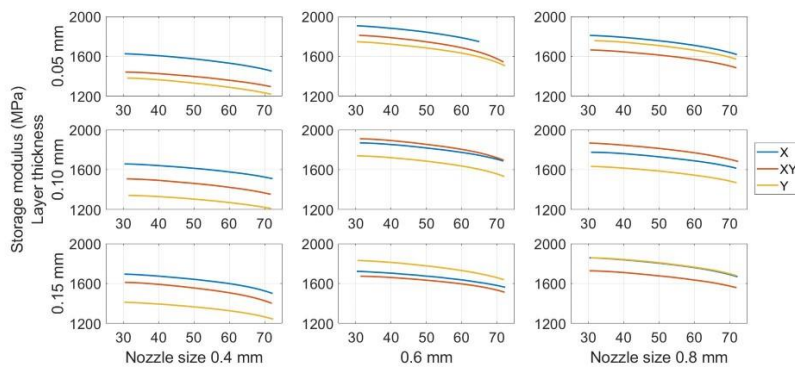
Figure 8-1 Detailed storage modulus change for different printing parameters from 30 to 70 °C.
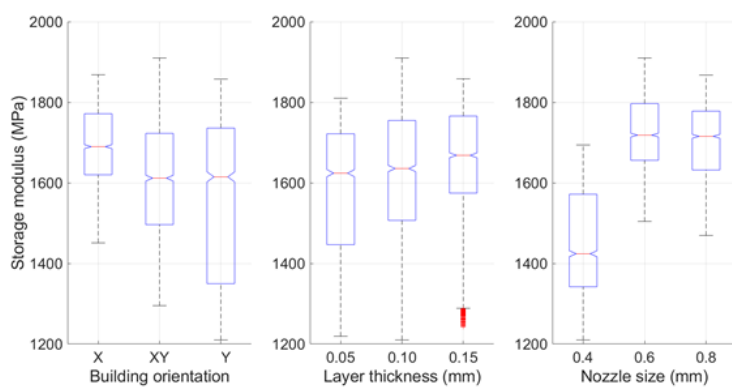
Figure 8-2 Statistical analysis of the storage modulus for different printing parameters.

Table 8-1 Mean storage modulus for different printing parameters.

Printing Parameters	Group	Mean Storage Modulus (MPa)	p-Value
Building Orientation	X	1692	2.34e−115
	XY	1616	
	Y	1561	
Nozzle Size (mm)	0.4	1450	0
	0.6	1722	
	0.8	1708	
Layer Thickness (mm)	0.05	1590	2.30e−31
	0.10	1622	
	0.15	1648	

The influence of the layer thickness appeared to be insignificant. Specimens with a layer thickness of 0.15 mm could provide a mean storage modulus of 1648 MPa, which is only approximately 60 MPa more than that provided by a 0.05 mm-thick layer specimen (1590 MPa). Whereas the results showed the difference when comparing with the previous works. Other previous research presented that lower layer thickness seemed to provide the higher strength (Hibbert et al., 2019)(Rankouhi et al., 2016). However, the nozzle size was found to have a significant influence on the storage modulus. The specimens printed with 0.6 mm and 0.8 mm nozzles had a significantly improved storage modulus, that is, over 1700 MPa, compared with the 1450 MPa mean storage modulus provided by the 0.4 mm nozzle size.

A statistical analysis of the data also indicated a similar conclusion. Compared with the p-value for different printing parameters, the p-value for the layer thickness of 2.30e−31 was greater than the other two parameters. It confirmed

that the change in layer thickness does not significantly impact the storage modulus of FDM ABS compared with the other two parameters.

8.2 Bending Fatigue Life of All Parameter Combinations

Each group of three specimens was tested with a bending fatigue test, and the mean cycles to fracture were recorded. The outliers inside each set were filtered and removed. **Figure 8-3** shows the mean number of cycles to the fracture counted for each parameter combination at different environmental temperatures. As can be seen, the specimen with an X raster orientation, nozzle size of 0.8 mm, and layer thickness of 0.15 mm printing had the longest fatigue life until the fracture at different environmental temperatures.
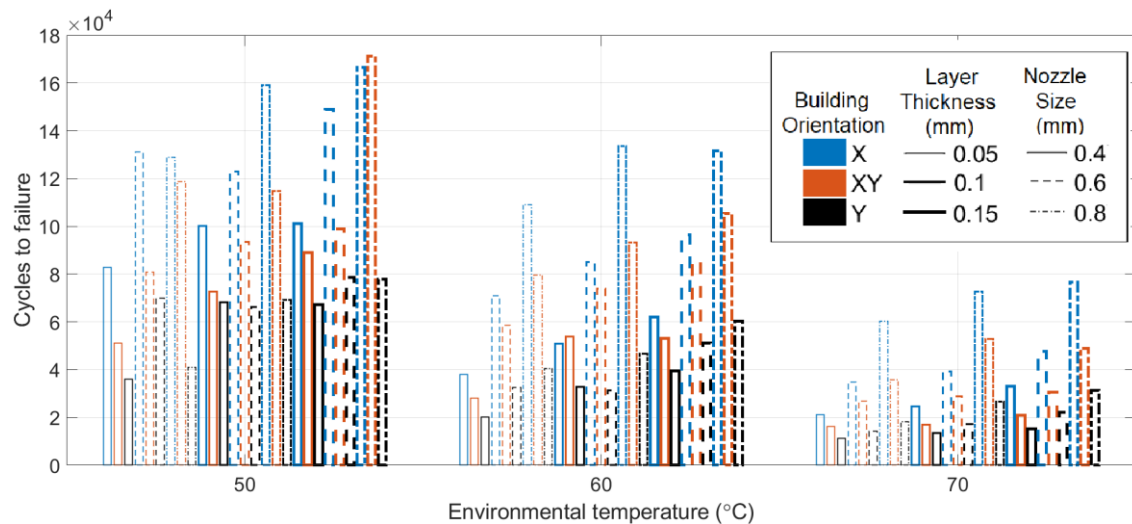
Figure 8-3 Mean number of cycles of specimens at different temperatures.

The fatigue life results were analysed through the Kruskal–Wallis test at a 95% confidence interval for each parameter (He and Khan, 2021). The study calculated the mean number of cycles for each constant parameter as one data group. The Kruskal–Wallis test tested the hypothesis that all group means are equal against the alternative hypothesis that at least one group is different from the others. It was used to determine whether the number of cycles from each group of parameters had a common mean. It can then find out whether different parameters have different influences on the beam's fatigue life.

Table 8-2 lists the F and *p*-values for each parameter. The *p*-value for the building orientation is 0.0001, for the nozzle size is 0.0027, for the layer thickness is 0.1684, and for the temperature is 1.11e−9.

Table 8-2 Statistical parameter values.

Parameter	Chi-Square	*p*-Value
Building Orientation	17.79	0.0001
Nozzle Size	11.81	0.0027
Layer Thickness	3.56	0.1684
Temperature	41.24	1.11e−9

Based on the *p*-values listed in **Table 8-2**, we can confirm that temperature has the most significant influence on fatigue strength, statistically. Building orientation and nozzle size also critically affect fatigue life. However, layer thickness did not significantly influence the range of values tested because the *p*-value of 0.1684 exceeded 0.05.

8.3 Temperature Influence on Fatigue Life

Figure 8-4 show the variation in the fatigue life at different environmental temperatures. As can be seen, the temperature has a significant impact on fatigue life. Notably, all the curves show similar decreasing trends, confirming that the fatigue resistance decreases when the temperature increases from 50 to 70 °C. The prior research focusing on conventional manufactured ABS had the same conclusion (Kim and Wang, 1995; Kim, Wang and Abdullah, 1994; Mura, Ricci and Canavese, 2018). **Table 8-3** presents the statistical data regarding the influence of temperature. The mean data was calculated by all specimens with the same temperatures regardless of other parameter settings. The subsequent statistical analysis of other parameters was also based on the same processing. By increasing the environmental temperature from 50 to 70 °C, the mean number of cycles until failure drops from 96,545 to 31,774 drastically.
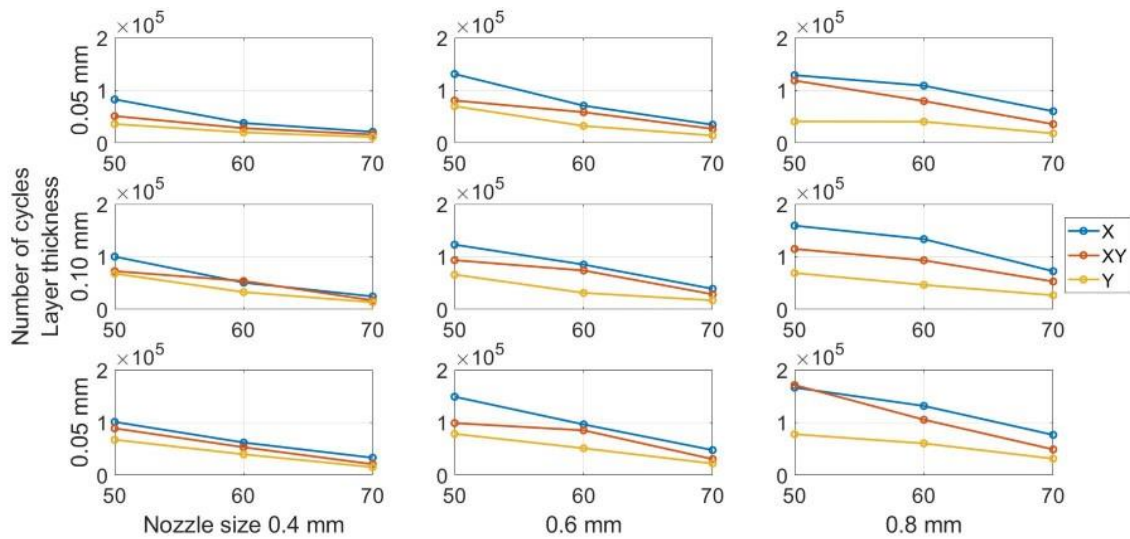
Figure 8-4 Effect of temperature on fatigue life.

Table 8-3 Mean number of cycles until fracture at different temperatures.

Environmental Temperature (°C)	Mean Number of Cycles until the Fracture	Standard Deviation
50	96,545	36,969
60	65,312	31,163
70	31,773	17,747

This most significant influence of temperature on fatigue life was due to the deterioration of the mechanical properties with the increase in temperature. The FDM ABS appeared to be glassy at lower temperatures in terms of the molecular microstructure. In other words, the rotation of the molecular chain ceased to occur and, therefore, the coil could not uncoil and lengthen (Anon, 2015). The side group and the chain elements could move in a small area. By increasing the environmental temperature, the energy of the moving units and movable space increased. Additionally, the van der Waals force between molecules decreased. The chemical bonds between the molecules were easy to break, and as such, the chain slip occurred easily (Tuttle, n.d.). Therefore, it can be concluded that microstructural fractures, crack initiation, and propagations

108

are easier in FDM ABS at higher temperatures. Furthermore, such changes in the microstructural properties influence the mechanical behaviour of the specimens. Finally, both the change in the microstructural and mechanical behaviour in FDM ABS contributes significantly to the fatigue life of the beam.

8.4 Building Orientation Influence on Fatigue Life

The building orientation is the most critical printing parameter affecting the fatigue life of the FDM ABS beam. **Figure 8-5** show the variation in the fatigue life for different building orientations. The specimens with the X building orientation have the highest number of cycles in all the subplots. The Y building orientation provides the worst fatigue performance, whereas the performance provided by the XY building orientation lies between them. **Table 8-4** lists the average fatigue life for groups with different building orientations. The X building orientation provides the longest fatigue life with an average of 96,545 cycles until fracture. However, the number of cycles is only 40,699 for beams with the Y building orientation. It is less than half the fatigue life of the X orientation. The experimental results are different from those presented in most previous studies, which performed the tensile fatigue test and reported that XY orientation had the best fatigue strength (Afrose et al., 2014, 2016; Letcher and Waytashek, 2014; Ziemian, Sharma and Ziemi, 2012; Ziemian, Ziemian and Haile, 2016; Ziemian, Okwara and Ziemian, 2015). The difference between tension and bending fatigue tests may cause this different result.

The results are reasonable. The initial seeded crack is lateral on the beam, the same as in the specimen with a Y building orientation. In fracture mechanics, the crack initiates and propagates from micro-cracks on or in the structure (Wang, 1996). These micro-cracks can be represented by 3D printing defects in the research. The micro-voids occur between the filaments in the structure. The presence of these air voids between the fibres leads to stress concentration when the beam vibrates.
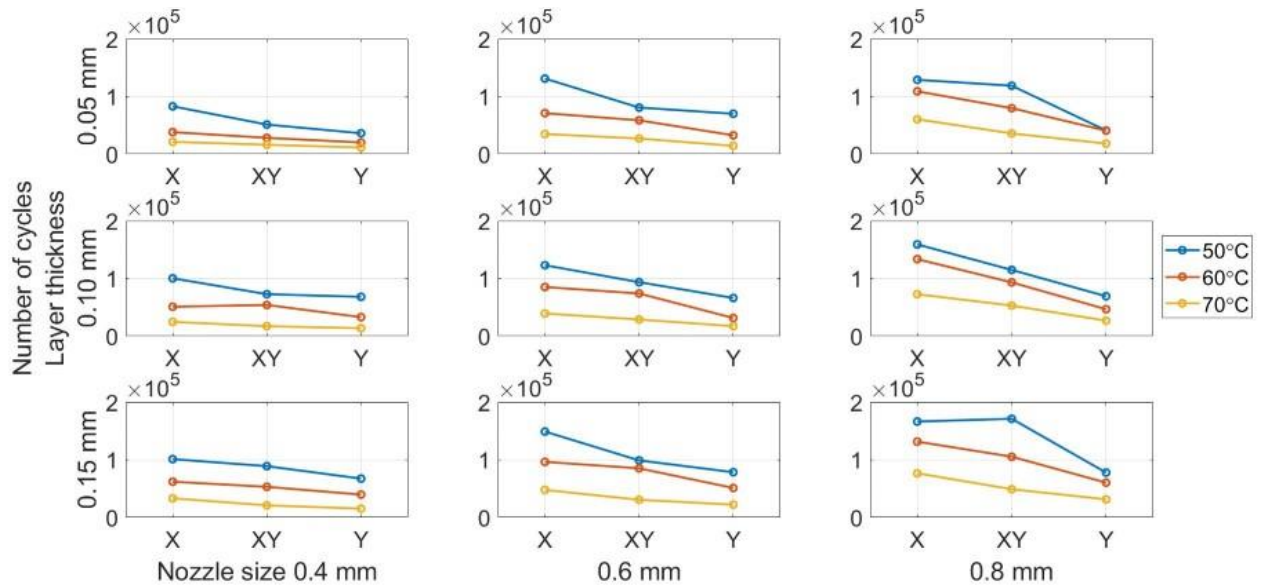
Figure 8-5 Building orientation effect on fatigue life.

Table 8-4 Mean number of cycles until fracture for different building orientations.

Building Orientation	Mean Number of Cycles until the Fracture	Standard Deviation
X	86,270	43,307
XY	66,659	37,338
Y	40,699	21,850

Furthermore, the bonds between the filaments are the weakest in the areas where the voids are present. The occurrence of crazing is earlier in the area with the voids. Notably, the direction of the void area is the same as that of the initial-seeded crack. This provides an excellent crack path that leads to quick crack propagation. On the contrary, due to the beam's vibration, the bending stress is longitudinal and acts on the Y orientation voids vertically, thereby accelerating the crack growth and decreasing the fatigue life.

8.5 Nozzle Size Influence on Fatigue Life

Figure 8-6 show the variation tendency of fatigue life for different nozzle sizes. As can be seen, the fatigue strength has an increasing trend when the nozzle size increases for all the specimens. The tests had the similar conclusion with FDM PLA (Gomez-Gras et al., 2018; Jerez-Mesa et al., 2017; Travieso-Rodriguez et al., 2019). **Table 8-5** present the mean fatigue life for the specimen group with different nozzle sizes. The mean number of cycles increases from 45,195 for the 0.4 mm nozzle size to 84,087 for the 0.8 mm nozzle size. The nozzle size also significantly influences the manufacturing time.
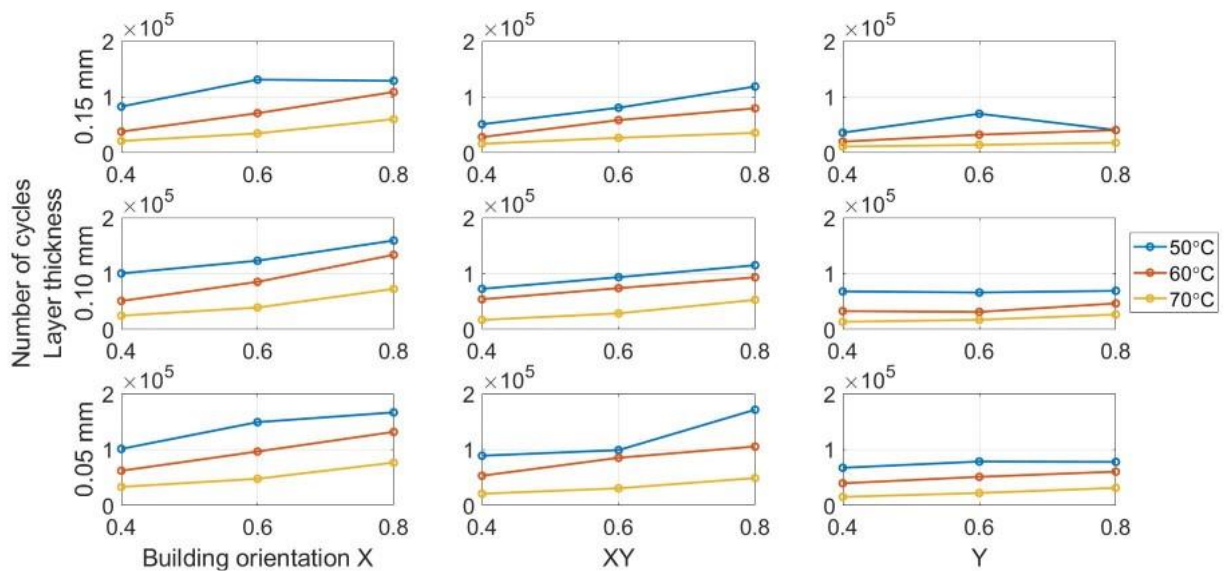
Figure 8-6 Influence of nozzle size on fatigue life.

Table 8-5 Mean number of cycles until fracture for different nozzle sizes.

Nozzle Size (mm)	Mean Number of Cycles until the Fracture	Standard Deviation
0.4	45,195	27,329
0.6	64,346	36,201
0.8	84,087	44,604

The effect of nozzle size on the fatigue life was similar to that in the case of a previously reported micro air voids theory. We assumed the spacing between the void defects during the printing process to be almost constant between the filaments, regardless of the thickness of the filament. This implies that the beam printed with a 0.8 mm-nozzle had fewer micro-voids than that printed with a 0.4-mm nozzle. Fewer void defects increase the global density of the specimen, thus reducing the stress concentration. The specimen then has a higher storage modulus, and the crack propagation becomes considerably difficult. Therefore, the overall fatigue life increases with the increase in the size of the nozzle.

8.6 Influence of Layer Thickness

We can verify the results obtained from the analysis of variance (ANOVA) test in Section 8.2 based on the data presented in **Figure 8-7**. The fatigue life only increases slightly when the layer thickness changes from 0.05 mm to 0.15 mm for all the specimens. A similar trend was reported in FDM PLA research (Gomez-Gras et al., 2018; Jerez-Mesa et al., 2017; Travieso-Rodriguez et al., 2019). Despite the ANOVA results regarding layer thickness show there is no significant relationship between it and fatigue life and the influence of layer thickness on the average fatigue life is not entirely clear based on the presented data. The statistical results presented in **Table 8-6** demonstrate the potential relationship between layer thickness and fracture resistance. The average fatigue life of the beam with a 0.15-mm layer thickness (74,463 cycles) is slightly higher than 0.1-mm (65,196 cycles) and 0.05-mm (53,969) layer thicknesses.

The possible cause of the effect of layer thickness may be the same as that in the case of nozzle size. Since micro air voids exist between each layer, the size of the voids is also almost constant and does not relate to the layer thickness. As a result, the beam with a thicker layer has fewer microvoids. Therefore, a 0.15-mm thick layer provides the best fatigue performance.
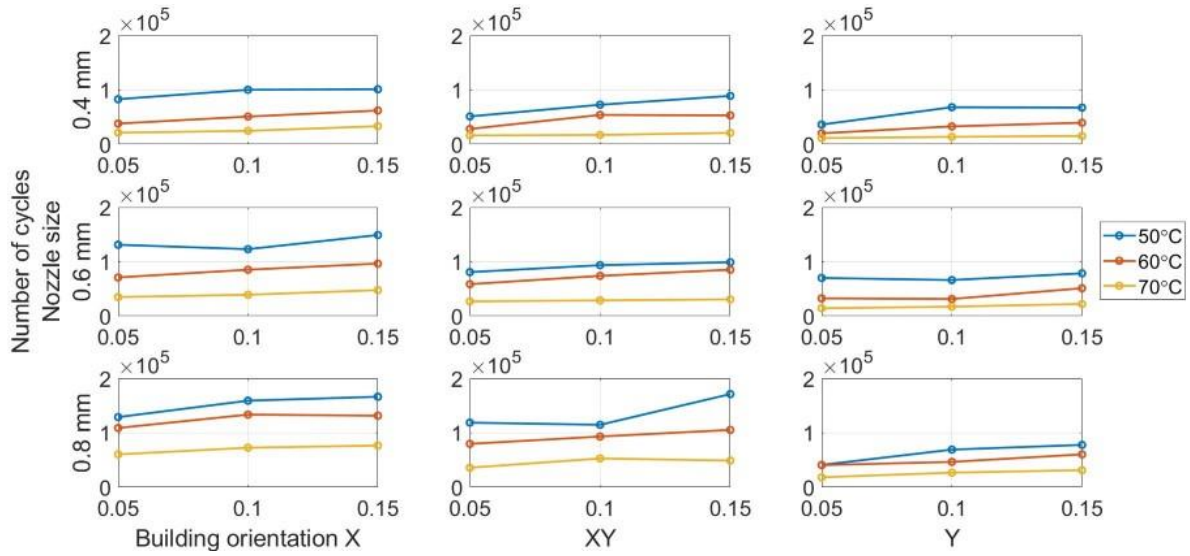
Figure 8-7 Layer thickness influence on fatigue life.

Table 8-6 Mean number of cycles until fracture for different layer thicknesses.

Layer Thickness (mm)	Mean Number of Cycles until the Fracture	Standard Deviation
0.05	53,969	35,857
0.10	65,196	38,314
0.15	74,463	43,126

8.7 Technological Recommendations for 3D Printing

The results obtained for fatigue life, as presented above, can help us obtain the optimal 3D printing parameter combination to ensure a better bending fatigue life within a specific parameter range investigated in this thesis. These parameters are listed in **Table 8-7**. A nozzle size of 0.8 mm and a layer thickness of 0.15 mm also significantly impacted the fatigue life as the use of these parameters led to a significant reduction in the manufacturing time of the parts.

Table 8-7 Optimal printing parameter combination for longer fatigue life.

Parameter	Optimal Level for Greater Resistance to Fatigue
Building Orientation	X
Nozzle Size	0.8 mm (The maximum nozzle provided by Ultimaker®)
Layer Thickness	0.15 mm

8.8 Fractography

After the bending fatigue tests, different pictures of the specimen fracture section were taken with a Dino-Lite digital microscope. **Figure 8-8** shows which surface is captured by the microscope. All the pictures in the following figures show the different levels of stress-whitening. Furthermore, it can be seen that the mixture of ductile and brittle breaks occur during the fracture for all the specimens. The white area represents the ductile fracture, but the red area represents the brittle fracture.
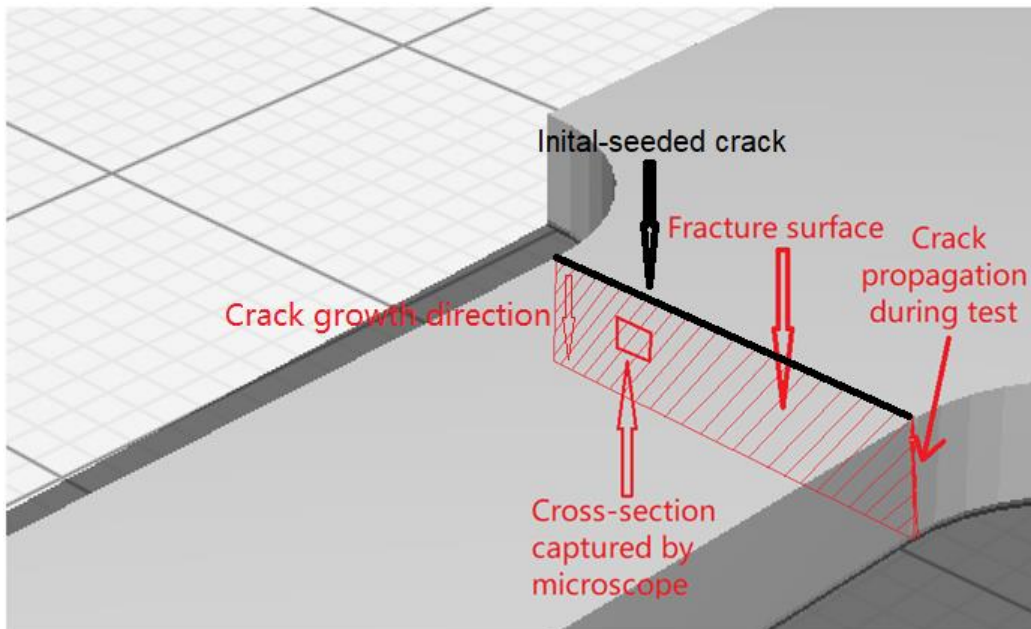
Figure 8-8 A schematic to show which cross-section was captured by the Dino-Lite digital microscope.

As a universal phenomenon in polymers, stress-whitening is caused by microvoids and crazes (Bucknall and Smith, n.d.). The polymer chains reorganize during tension when the beam is vibrating. The straightening, slipping, and shearing of the fillers and the polymer chains during movement within the plastic's microenvironment may lead to the formation of occlusions or holes in some cases. When these occlusions are combined, microvoids are produced. The transmitted light is scattered when the microvoids cluster to a size greater than or equal to the wavelength of light (380–750 nm). The microvoids change the refractive index of the plastic, causing the object to appear white.

In other words, the defects (voids) of the 3D printing ABS cause local stress concentration and these areas are more likely to induce crazes. **Figure 8-9** to **Figure 8-11** show the specimens with different nozzle sizes. Similarly, printing defects occur between each filament. However, the distance between each void, representing the nozzle size, varies in the horizontal direction. As seen from the aforementioned figures, all the pictures show some bright white lines extending from the printing voids along the direction of crack growth, confirming that the crack propagates along the microvoids and crazes. Then, the void numbers in the cross-section of specimens were calculated approximately. For the 0.15 mm layer thickness specimen, the 0.4 mm nozzle printed a total of 500 air voids. This was more than the 333 voids of 0.6 mm and 250 voids of 0.4 mm. This can also be visually observed from **Figure 8-9** to **Figure 8-11**. Because the number of voids within the same area cross-section of a 0.4-mm nozzle (61) is more than that of a 0.6 (40) and 0.8 mm nozzle (31), consequently, the number of stress whitening areas is also greater in the former. This results in higher fatigue crack growth rate and short fatigue life.

Furthermore, from the figures mentioned above, it can be observed that all the pictures show that the crack growth rate is time-dependent. The white and red areas alternately appear along the crack propagation direction. This means the crack growth dominated by the ductile break and brittle break alternately occur. The layer-by-layer 3D-printed structure may lead to the phenomenon.

Furthermore, the brittle break rate in the red area is higher than the ductile break in the white area. It is also reflected in the global colour distribution along the crack propagation direction on the section. The colour near the beam surface is significantly whiter than the bottom area. The ductile break gradually changes to a brittle break during crack propagation. This implies that the initial crack growth rate is less than the latter because the crack tip's stress may increase along with the depth of the crack. The greater the stress, the faster and easier the brittle fracture.
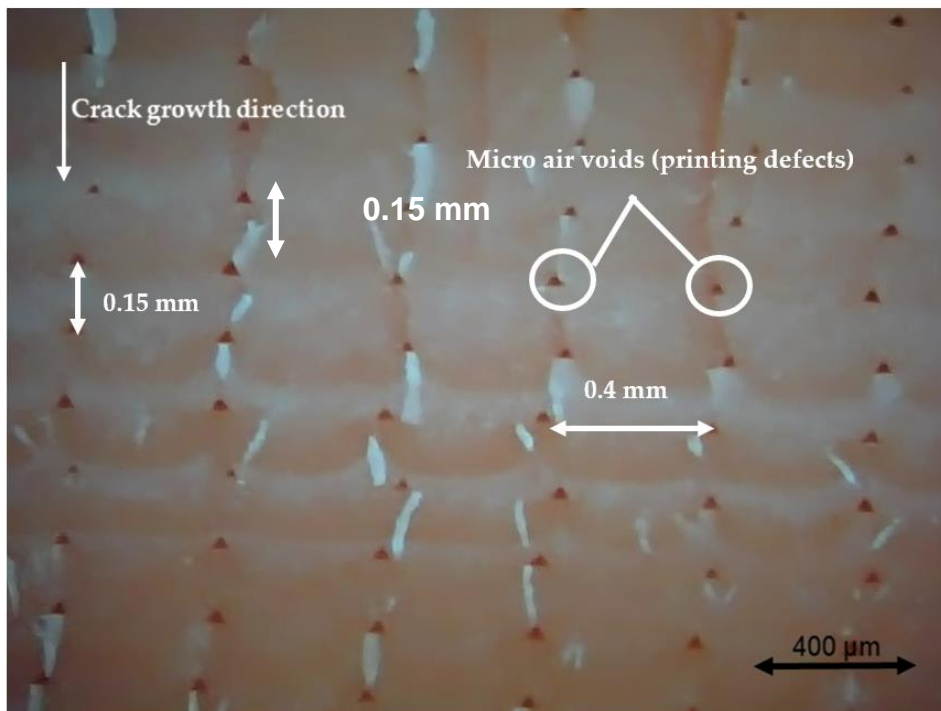
Figure 8-9 Specimen with a nozzle size of 0.4 mm, X building orientation, and layer thickness of 0.15 mm.

Figure 8-12 shows the cross-sectional area for the XY building orientation. Compared to **Figure 8-9**, **Figure 8-12** shows a larger area of voids. Furthermore, the larger stress whitening area connects the voids. These larger area voids decreased the strength of a structure, leading to decreased fatigue life than X building orientation. However, **Figure 8-13**, which presents the fracture section of the Y printing orientation, shows that there is almost no stress whitening in this section. This is because this section has the weakest bonds between the two filaments. Therefore, the brittle fracture continues along

this section. The voids between each filament and layer, represented by dark red, occupy a large fracture surface area, speeding up the crack growth rate.

The inter-filament bonding strength along the crack path in the specimen with a Y building orientation is also extremely weak. As can be seen from **Figure 8-13** and **Figure 8-14**, some loose filaments are peeled off the fractured surface.

When **Figure 8-15** and **Figure 8-16** are compared for the layer thickness effect, we can see that the section with a 0.15 mm layer thickness has fewer defects (dark red area) between the layers in the unit section. This may be the reason why it has a longer fatigue life.
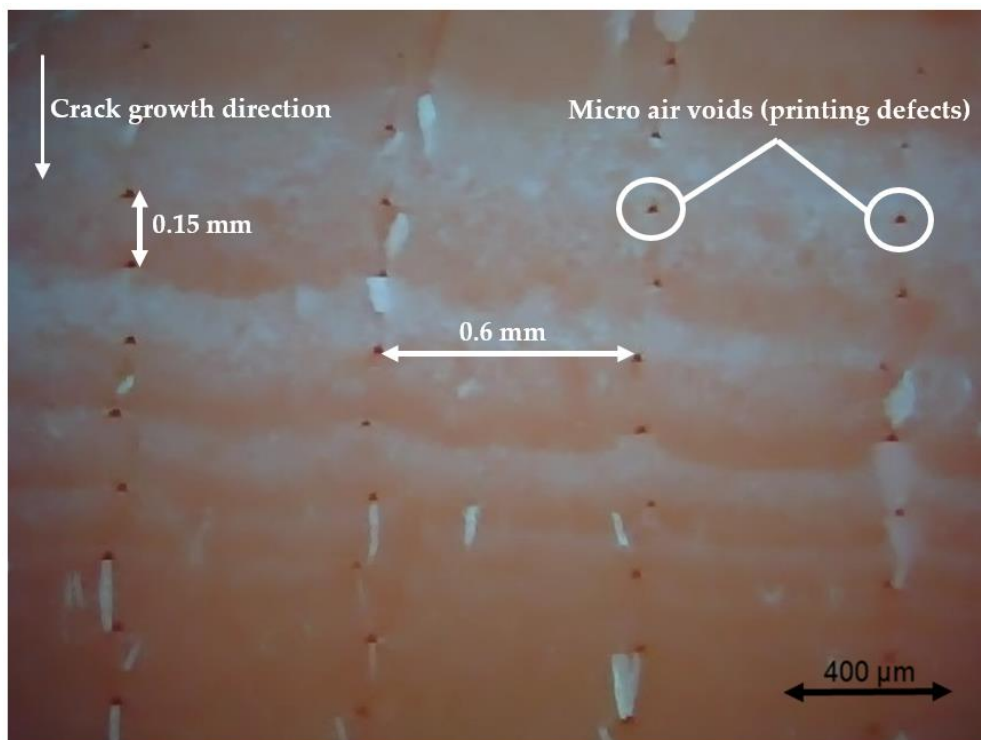
Figure 8-10 Specimen with a nozzle size of 0.6 mm, X building orientation, and layer thickness of 0.15 mm.
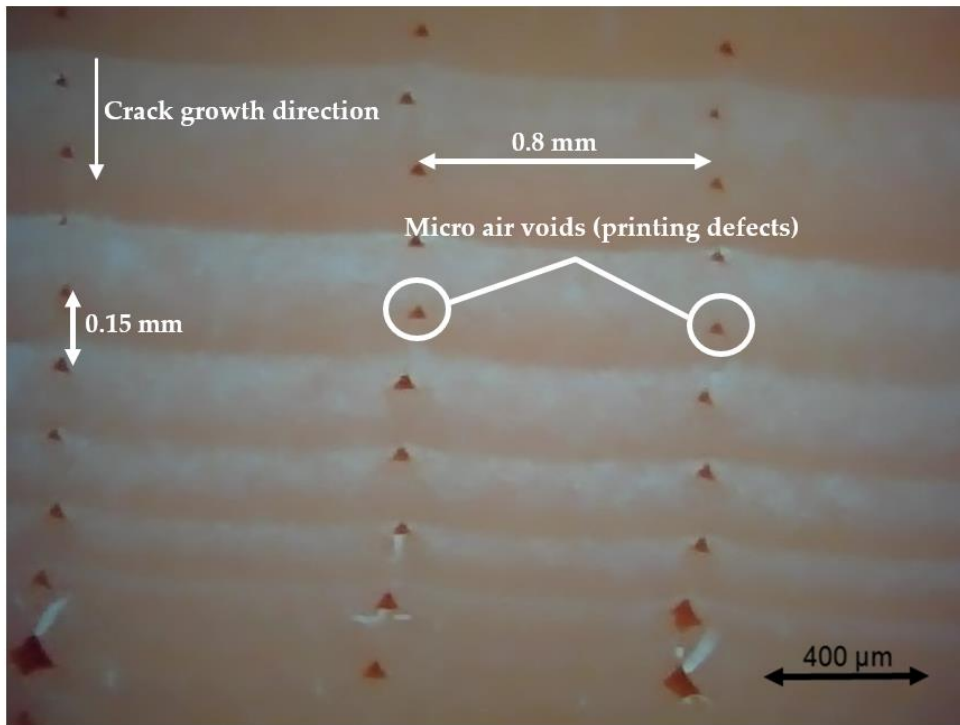
Figure 8-11 Specimen with a nozzle size of 0.8 mm, X building orientation, and a layer thickness of 0.15 mm.
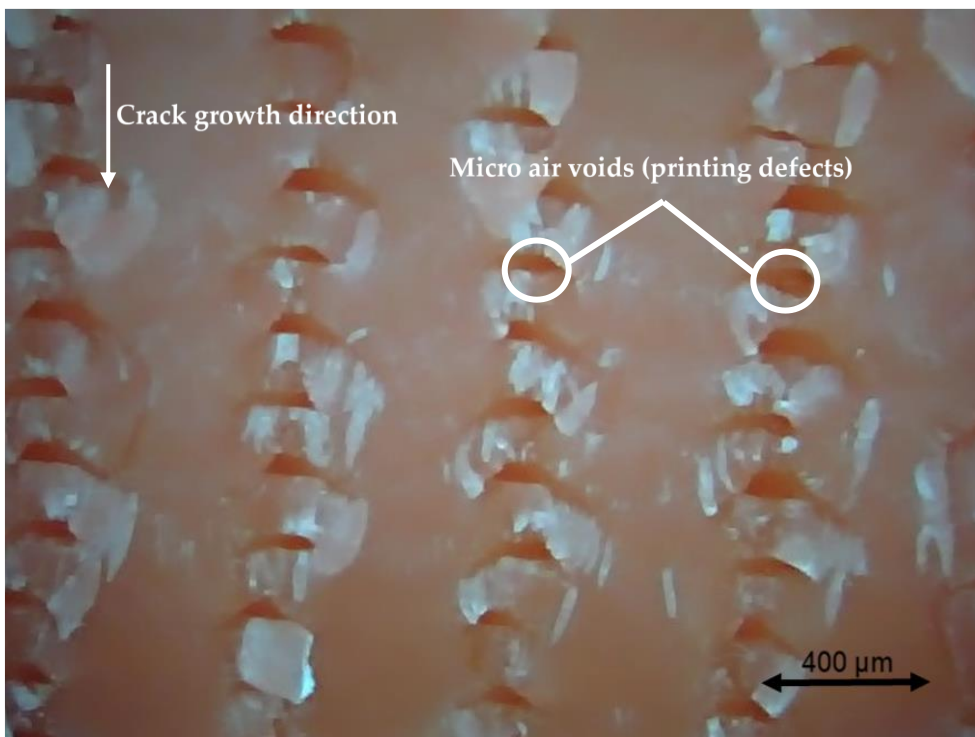
Figure 8-12 Specimen with nozzle sizes of 0.4 mm, XY building orientation and layer thickness of 0.15 mm.
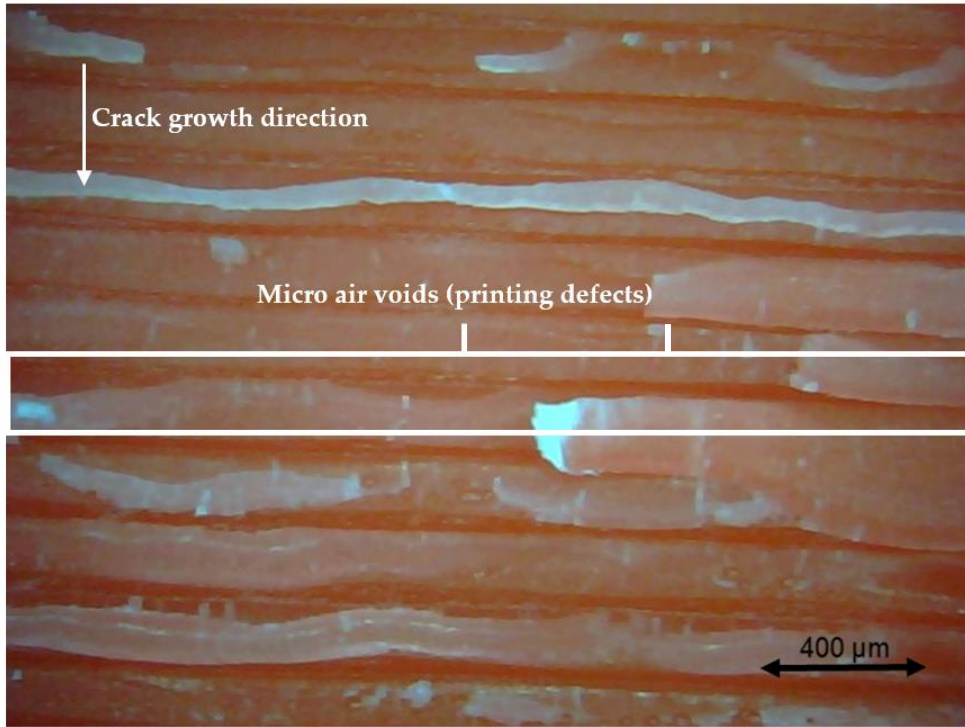
Figure 8-13 Specimen with a nozzle size of 0.4 mm, Y building orientation, and layer thickness of 0.15 mm.

Figure 8-14 Specimen with a nozzle size of 0.8 mm, Y building orientation, and layer thickness of 0.15 mm.
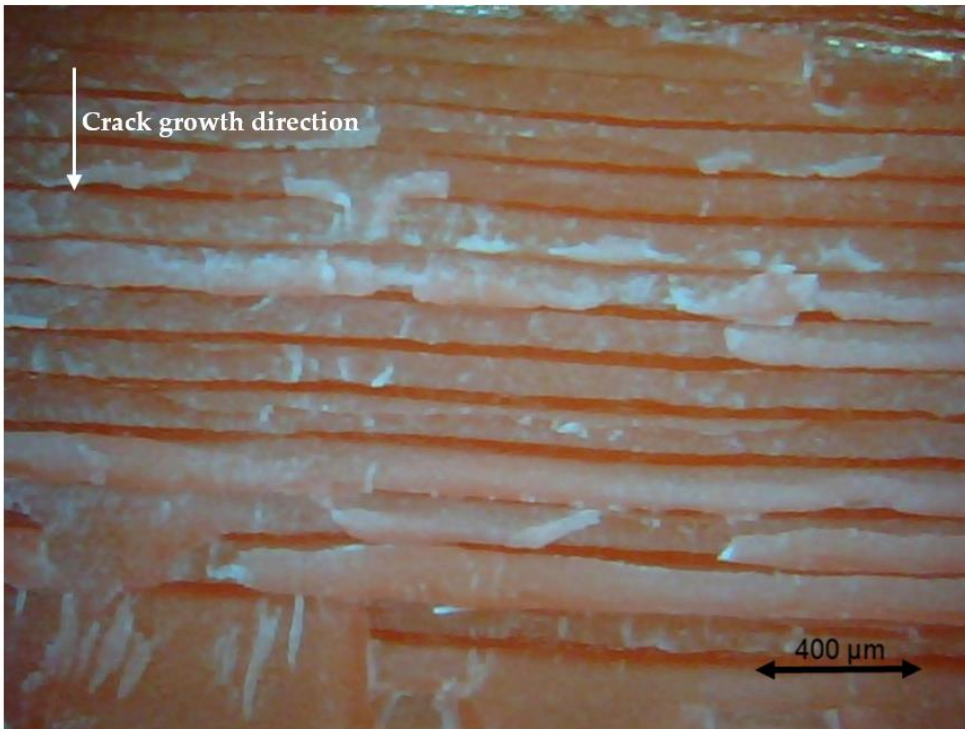
Figure 8-15 Specimen with a nozzle size of 0.6 mm, Y building orientation, and layer thickness of 0.1 mm.
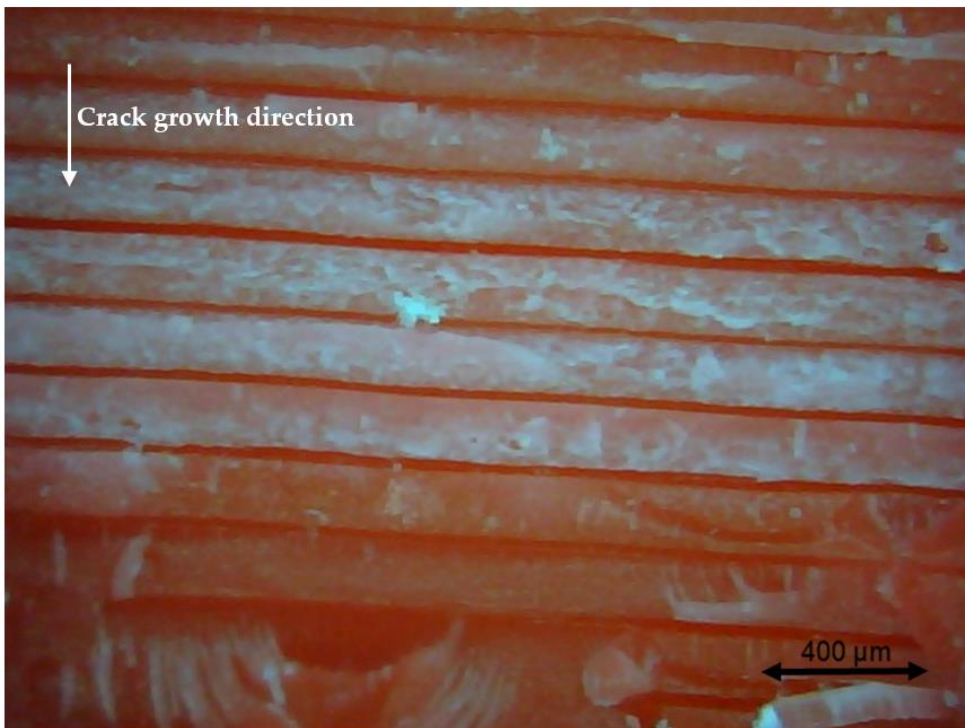
Figure 8-16 Specimen with a nozzle size of 0.6 mm, Y building orientation, and layer thickness of 0.15 mm.

9 CONCLUSIONS

This research investigated the dynamic response of cracked FDM structures under thermo-mechanical loads in an in-situ manner. The interactions between thermo-mechanical loads, crack propagation and dynamic response were analysed with the corresponding experimental validation. The research objectives shown in Section 1.4 were achieved and some novel contributions are summarised below.

9.1 Achievement of the Objectives

Objective 1 - Evaluate the relationship between the crack severity and structural dynamic response for 3D-printed ABS cantilever beam at elevated temperatures. (achieving in Chapters 3, 4 and 7)

The research improved the torsional spring model in prior research. An additional dimensionless coefficient $\left(\frac{H-a}{H}\right)$ was introduced and used for crack size modelling. Therefore, a more accurate analytical relationship between the natural frequency and structural integrity was developed. The estimation accuracy prediction accuracy improved by at least 50% compared to the previous model. The estimation accuracy has even increased significantly by around 20% to 120% for the high crack depth (a/H >0.6). The research also first proposed the analytical model for amplitude calculation of cracked structure under thermo-mechanical loads.

Objective 2 – Evaluate the relationship between the crack tip loading and structural dynamic response. (achieving in Chapter 5)

The research proposed an analytical model to calculate the stress loading at crack tip according to the structural dynamic response. The cracked beam governing equation is used to develop the relationship between the beam tip displacement amplitude under fundamental frequency and stress intensity factor at the crack tip.

Objective 3 - Develop the experiments and data post-process method for dynamic fatigue test to validate the analytical model. (achieving in Chapters 6 and 8)

A series of experiments were designed with the consideration of dynamic thermo-mechanical loads. The author built suitable experiment setups and designed the experimental scheme and procedure. The raw data from experiments were processed appropriately. The proposed analytical models were validated with a comparison with experimental data.

Objective 4 - Evaluate the dynamic fatigue life for 3D printed ABS and determine the optimal 3D printing parameter combination under dynamic thermo-mechanical loads.

The fatigue life of FDM structure with 27 different printing parameter combinations was investigated experimentally under dynamic thermo-mechanical loads. After the comprehensive investigation, the research proposed the optimal printing parameters (i.e. X building orientation, 0.8 mm nozzle size and 0.15 mm layer thickness for the beam-like structure under dynamic bending load in a thermal environment. The optimal printing parameters provide a 50% longer fatigue life than the average value.

9.2 Novel Contribution and Their Significance

9.2.1 Analytical Modelling between Dynamic Response and Crack Propagation

This research proposed an analytical model to determine the dynamic response of a cracked 3D-printed ABS cantilever beam under a thermal environment. Compared with the previous model, the fundamental frequency can be modelled more precisely. The corresponding displacement amplitudes were also calculated accurately for the first time.

For the dynamic response to the structural crack, both fundamental frequency and displacement amplitude decrease as crack growth. On the other hand, the crack location further away from the fixed end of the beam leads to higher

fundamental frequency and displacement amplitude. Moreover, the increased temperature reduces the fundamental frequency of the fractured beam.

For comparing the fundamental frequency and displacement amplitude, the displacement amplitude at the beam tip is more sensitive than the fundamental frequency to crack depth and location change at the beginning of crack growth.

In practical applications, the proposed analytical model in this thesis has excellent potential to be used to assess structural integrity. Whether it is the vibration displacement of the beam or the fundamental frequency, or even just the load applied to the structure, by analysing their relationship to the crack depth or location, one can accurately estimate the severity of the damage under a complex working environment.

9.2.2 Modelling between Loading Conditions at Crack Tip and Dynamic Response

An analytical relationship was proposed between the stress condition at the crack tip and the dynamic response for cracked FDM structure under thermo-mechanical loads. Therefore, the interaction of the dynamic thermo-mechanical loads and crack propagation can be represented analytically. The stress condition at the crack tip can be in-situ estimated by simply measuring the dynamic response of the structure in practical applications

9.2.3 3D Printing Parameters Effect on Fatigue Behaviour of FDM Structure

With the experimental validations for the analytical model, the research also evaluated the influence of printing parameters (building orientation, nozzle size, and layer thickness) and environmental temperature on the bending fatigue life of the FDM ABS beam under thermo-mechanical loads.

The thesis proposed that the printing air void defects fundamentally reduced the fatigue life of the FDM structure. Most of the printing parameters ultimately affect the fatigue behaviour by influencing the structural porosity. Therefore, minimising the adverse effects of microscopic air voids by adjusting printing parameters is critical to improving structural fatigue behaviour. The research

also provides the optimal printing parameters combination which can be used for FDM manufacturing in the future.

9.3 Research Work Limitations

Although the study developed several analytical models for the relationship between dynamic response and crack severity, there are still limitations for the current work.

The effect of the crack breathing and closure on displacement amplitude is still represented by a mathematical formula rather than pure analytical relation. Due to the size limitation of the experimental equipment and specimen, the analytical model of dynamic response can only be validated for relatively small structures. The analytical model presented in this thesis is only for simple beam structures, so further research is required for other complex structures.

For the investigation of printing parameters, the optimum performance of the specimen also depends on the actual loading conditions. The pure bending considered in this research is still too simple compared to the practical application. Furthermore, this research only tests the global printing parameters, which means every printed unit cell has the same parameters. It might be helpful to consider testing the local different print parameters influence on fatigue life for one specimen for actual load situations.

9.4 Future Works

The proposed analytical models in the thesis are suitable for beam structures only, and however, many other geometries of FDM structures are available for practical engineering applications. Therefore, the next step in the research is to develop an applicable dynamic response model for plate FDM structures.

Based on the analytical relationship between stress conditions at the crack tip and structural dynamic response, future research will focus on the crack growth rate in FDM structure under dynamic thermo-mechanical loads.

The effect of printing parameters on crack growth rate in FDM structure will be investigated experimentally. Furthermore, the research will work on the direct

analytical modelling between dynamic thermo-mechanical loads and crack growth rate.

The crack propagation in AM composite under dynamic thermo-mechanical loads will also be evaluated in the future.

REFERENCES

Afrose, M.F., Masood, S.H., Iovenitti, P., Nikzad, M. and Sbarski, I. (2016) 'Effects of part build orientations on fatigue behaviour of FDM-processed PLA material', *Progress in Additive Manufacturing*, 1(1–2) Springer International Publishing, pp. 21–28.

Afrose, M.F., Masood, S.H., Nikzad, M. and Iovenitti, P. (2014) 'Effects of Build Orientations on Tensile Properties of PLA Material Processed by FDM', *Advanced Materials Research*, 1044–1045, pp. 31–34.

Agarwalla, D.K. and Parhi, D.R. (2013) 'Effect of crack on modal parameters of a cantilever beam subjected to vibration', *Procedia Engineering*, 51(NUiCONE 2012) Elsevier B.V., pp. 665–669.

Ahn, S., Montero, M., Odell, D., Roundy, S., Wright, P.K., Montero, M. and Wright, P.K. (2002) 'Anisotropic material properties of fused deposition modeling ABS', *Rapid Prototyping Journal*, 8(4), pp. 248–257.

Akbarzadeh Khorshidi, M. and Soltani, D. (2013) 'Diagnosis of Type, Location and Size of Cracks by Using Generalized Differential Quadrature and Rayleigh Quotient Methods', *Journal of Theoretical and Applied Mechanics*, 43(1), pp. 61–70.

Akil, H. and Zamri, M.H. (2013) *Performance of natural fiber composites under dynamic loading*. Woodhead Publishing Limited.

Aliheidari, N., Tripuraneni, R., Christ, J., Ameli, A., Aliheidari, N., Tripuraneni, R., Hohimer, C. and Christ, J. (2017) 'The impact of nozzle and bed temperatures on the fracture resistance of FDM printed materials', *Proceedings of SPIE - The International Society for Optical Engineering*., Vol.10165.

Altunışık, A.C., Okur, F.Y. and Kahya, V. (2017) 'Modal parameter identification and vibration based damage detection of a multiple cracked cantilever beam', *Engineering Failure Analysis*, 79(April), pp. 154–170.

Andrady, A.L. and Neal, M.A. (2009) 'Applications and societal benefits of plastics', *Philosophical Transactions of the Royal Society B: Biological Sciences*, 364(1526), pp. 1977–1984.

Ang, K.C., Leong, K.F., Chua, C.K. and Chandrasekaran, M. (2006) 'Investigation of the mechanical properties and porosity relationships ...', *Rapid Prototyping Journal*, 12(2), pp. 100–105.

Anon (n.d.) '*ISO 527*'

Anon (n.d.) '*ISO 178*'

Anon (2015) *Introduction to Polymers.*, *The Open University* Available at: https://www.open.edu/openlearn/science-maths-technology/science/chemistry/introduction-polymers/content-section-2.5.3 (Accessed: 18 July 2021).

Baker, A.A., Jones, R. and Callinan, R.J. (1985) 'Damage tolerance of graphite/epoxy composites', *Composite Structures*, 4(1), pp. 15–44.

Baker, D.A., Hastings, R.S. and Pruitt, L. (2000) 'Compression and tension fatigue resistance of medical grade ultra high molecular weight polyethylene: The effect of morphology, sterilization, aging and temperature', *Polymer*

Baqasah, H., He, F., Zai, B.A., Asif, M., Khan, K.A., Thakur, V.K. and Khan, M.A. (2019) 'In-situ dynamic response measurement for damage quantification of 3D printed ABS cantilever beam under thermomechanical load', *Polymers*, 11(12)

Barad, K.H., Sharma, D.S. and Vyas, V. (2013) 'Crack detection in cantilever beam by frequency based method', *Procedia Engineering*, 51(NUiCONE 2012) Elsevier B.V., pp. 770–775.

Basu, S. and Giessen, E. Van Der (2002) 'A thermo-mechanical study of mode I

, small-scale yielding crack-tip fields in glassy polymers', *International Journal of Plasticity*, 18, pp. 1395–1423.

Bellini, A. and Güçeri, S. (2003) 'Mechanical characterization of parts fabricated using fused deposition modeling', *Rapid Prototyping Journal*, 9(4), pp. 252–264.

Bertoldi, M., Yardimci, M.A., Pistor, C.M., Guyeri, S.I. and Sala, G. (1998) 'Mechanical Characterization of Parts Processed via Fused Deposition', *International Solid Freeform Fabrication Symposium.*, pp. 557–566.

Bjerke, T. and Lambros, J. (2002) 'Heating During Shearing and Opening Dominated Dynamic Fracture of Polymers', *Experimental Mechanics*, 42(1), pp. 107–114.

Bjerke, T.W. and Lambros, J. (2003) 'Theoretical development and experimental validation of a thermally dissipative cohesive zone model for dynamic fracture of amorphous polymers', *Journal of the Mechanics and Physics of Solids*, 51, pp. 1147–1170.

Böhning, M., Frasca, D., Schulze, D. and Schartel, B. (2019) *Multilayer graphene/elastomer nanocomposites.* Elsevier Inc.

Boltezar, M., Strancar, B. and Kuhelj, A. (1998) 'Identification of transverse crack location in flexural vibrations of free-free beams', *Journal of Sound and Vibration*, 211(5), pp. 729–734.

Bretz, P.E., Hertzberg, R.W. and Manson, J.A. (1981) 'Mechanisms of fatigue damage and fracture in semi-crystalline polymers', *Polymer*, 22(9), pp. 1272–1278.

Brillhart, M. and Botsis, J. (1994) 'Fatigue crack growth analysis in PEEK', *International Journal of Fatigue*, 16(2), pp. 134–140.

Brillhart, M. and Botsis, J. (1992) 'Fatigue fracture behaviour of PEEK: 2. Effects of thickness and temperature', *Polymer*, 33(24), pp. 5225–5232.

Bucknall, C.B. and Smith, R.R. (n.d.) '*Stress-whitening in High-impact Polystyrenes*', , pp. 437–446.

Chandy, T., Hee, J. Van, Nettekoven, W. and Johnson, J. (2009) 'Long-Term In Vitro Stability Assessment of Polycarbonate Urethane Micro Catheters : Resistance to Oxidation and Stress Cracking', *Journal of Biomedical Materials Research - Part B Applied Biomaterials*, 89(2), pp. 314–324.

Chati, M., Rand, R. and Mukherjee, S. (1997) 'Modal analysis of a cracked beam', *Journal of Sound and Vibration*, 207(2), pp. 249–270.

Chen, Y.T. and Liu, K.X. (2015) 'Crack propagation in viscoplastic polymers : Heat generation in near-tip zone and viscoplastic cohesive model', *Applied Physics Letters*, 106(6)

Cheng, W.M., Miller, G.A., Manson, J.A., Hertzberg, R.W. and Sperling, L.H. (1990) 'Mechanical behaviour of poly (methyl methacrylate) The temperature and frequency effects on the fatigue crack propagation behaviour', *Journal of Materials Science*, 25(4), pp. 1924–1930.

Chou, Y.F. and Sun, C.T. (1983) 'Modeling of the frequency effect on fatigue crack propagation in PMMA', *Engineering Fracture Mechanics*, 17(I), pp. 17–26.

Das, S., Saha, P. and Patro, S.K. (2016) 'Vibration-based damage detection techniques used for health monitoring of structures: a review', *Journal of Civil Structural Health Monitoring*, 6(3) Springer Berlin Heidelberg, pp. 477–507.

Dastjerdi, S. and Abbasi, M. (2019) 'A vibration analysis of a cracked micro-cantilever in an atomic force microscope by using transfer matrix method', *Ultramicroscopy*, 196(September 2018) Elsevier B.V., pp. 33–39.

Ding, G., Karlsson, A.M. and Santare, M.H. (2017) 'Numerical evaluation of fatigue crack growth in polymers based on plastically dissipated energy', *International Journal of Fatigue*, 94 Elsevier Ltd, pp. 89–96.

Ding, J., Remij, E.W., Remmers, J.J.C. and Huyghe, J.M. (2019) 'Effects of Intrinsic Properties on Fracture Nucleation and Propagation in Swelling Hydrogels', *Polymers*, 11(5), pp. 1–12.

Douka, E. and Hadjileontiadis, L.J. (2005) 'Time-frequency analysis of the free

vibration response of a beam with a breathing crack', *NDT and E International*, 38(1), pp. 3–10.

Dumpleton, P. and Bucknall, C.B. (1987) 'Comparison of static and dynamic fatigue crack growth rates in high- density polyethylene', *International journal*, 9(3), pp. 151–155.

Eftekhari, M. and Fatemi, A. (2016) 'On the strengthening effect of increasing cycling frequency on fatigue behavior of some polymers and their composites: Experiments and modeling', *International Journal of Fatigue*, 87 Elsevier Ltd, pp. 153–166.

Ellyson, B., Chekir, N., Brochu, M. and Brochu, M. (2017) 'Characterization of bending vibration fatigue of WBD fabricated Ti-6Al-4V', *International Journal of Fatigue*, 101 Elsevier Ltd, pp. 36–44.

Estevez, R., Basu, S. and Giessen, E. VAN DER (2005) 'Analysis of temperature effects near mode I cracks in glassy', *International Journal of Fracture*, 132, pp. 249–273.

Fan, H., Keer, L.M. and Cheng, H.S. (1993) 'Competition Between Fatigue Crack Propagation and Wear', *Journal of Tribology*, 115(January), pp. 141–147.

Fang, Q., Li, H. and Wang, T. (2007) 'Fatigue crack growth behavior of PC and PC/ABS', *Acta Polymerica Sinica*, (8), pp. 713–718.

Fang, Q.Z., Wang, T.J. and Li, H.M. (2007) 'Overload effect on the fatigue crack propagation of PC/ABS alloy', *Polymer*, 48(22), pp. 6691–6706.

Fleet, T., Kamei, K., He, F., Khan, M.A., Khan, K.A. and Starr, A. (2020) 'A machine learning approach to model interdependencies between dynamic response and crack propagation', *Sensors (Switzerland)*, 20(23), pp. 1–13.

Ford, A.C., Gramling, H., Li, S.C., Sov, J. V, Srinivasan, A. and Pruitt, L.A. (2018) 'Journal of the Mechanical Behavior of Biomedical Materials Micromechanisms of fatigue crack growth in polycarbonate polyurethane : Time dependent and hydration e ff ects', *Journal of the Mechanical Behavior*

ofBiomedical Materials, 79(January), pp. 324–331.

Foyos, J., Noorani, R., Mendelson, M., Marloth, R. and Pregger, B.A. (2000) 'Effect of Layer Orientation on Mechanical Properties of Rapid Prototyped Samples', *Materials and Manufacturing Processes*, 15(1), pp. 107–122.

Gao, W., Zhang, Y., Ramanujan, D., Ramani, K., Chen, Y., Williams, C.B., Wang, C.C.L., Shin, Y.C., Zhang, S. and Zavattieri, P.D. (2015) 'The status, challenges, and future of additive manufacturing in engineering', *CAD Computer Aided Design*, 69 Elsevier Ltd, pp. 65–89.

Ghadimi, S. and Kourehli, S.S. (2017) 'Multiple crack identification in Euler beams using extreme learning machine', *KSCE Journal of Civil Engineering*, 21(1), pp. 389–396.

Ghuzlan, K.A. and Carpenter, S.H. (2000) 'Energy-Derived, Damage-Based Failure Criterion for Fatigue Testing', *Transportation Research Record: Journal of the Transportation Research Board*, 1723(1), pp. 141–149.

Gillich, G.-R., Praisach, Z.-I., Abdel Wahab, M. and Furdui, H. (2014) 'A new modal-based damage location indicator', *{P}roceedings of the {I}nternational {C}onference on {N}oise and {V}ibration {E}ngineering {ISMA 2014}*, (September), pp. 499–512.

Gillich, G.R., Furdui, H., Abdel Wahab, M. and Korka, Z.I. (2019) 'A robust damage detection method based on multi-modal analysis in variable temperature conditions', *Mechanical Systems and Signal Processing*, 115 Elsevier Ltd, pp. 361–379.

Gillich, G.R., Maia, N.M.M., Mituletu, I.C., Praisach, Z.I., Tufoi, M. and Negru, I. (2015) 'Early structural damage assessment by using an improved frequency evaluation algorithm', *Latin American Journal of Solids and Structures*, 12(12), pp. 2311–2329.

Gillich, G.R. and Praisach, Z.I. (2014) 'Modal identification and damage detection in beam-like structures using the power spectrum and time-frequency analysis', *Signal Processing*, 96(PART A) Elsevier, pp. 29–44.

Gomez-Gras, G., Jerez-Mesa, R., Travieso-Rodriguez, J.A. and Lluma-Fuentes, J. (2018) 'Fatigue performance of fused filament fabrication PLA specimens', *Materials & Design*, 140 Elsevier Ltd, pp. 278–285.

Gupta, A., Jain, N.K., Salhotra, R. and Joshi, P.V. (2017) 'Effect of thermal environment on vibration analysis of isotropic micro plate with inclined crack based on modified couple stress theory', *24th International Congress on Sound and Vibration, ICSV 2017*, , pp. 1–7.

Hahn, M.T., Hertzberg, R.W., Manson, J.A., Lang, R.W. and Bretz, P.E. (1982) 'Effect of test frequency and water content on localized crack-tip heating in nylon-6,6', *Polymer*, 23(11), pp. 1675–1679.

Hartwig, G. and Knaak, S. (1991) 'Fatigue behaviour of polymers', *Cryogenics*, 31(4), pp. 231–233.

Hassanpour, P.A., Esmailzadeh, E., Cleghorn, W.L. and Mills, J.K. (2010) 'Generalized Orthogonality Condition for Beams with Intermediate Lumped Masses Subjected to Axial Force', *Journal of Vibration and Control*, 16(5), pp. 665–683.

He, F. and Khan, M. (2021) 'Effects of Printing Parameters on the Fatigue Behaviour of 3D-Printed ABS under Dynamic Thermo-Mechanical Loads', *Polymers*, 13(14), p. 2362.

He, F., Khan, M.A. and Zai, B.A. (2019) 'Material mechanics of crack growth in structural dynamics', *Procedia Structural Integrity*, 17 Elsevier B.V., pp. 72–79.

He, F., Kumar, V. and Khan, M.A. (2020) 'Evolution and New Horizons in Modelling Crack Mechanics of Polymeric Structures', *Materials Today Chemistry*

Henriques, I.R., Borges, L.A., Costa, M.F., Soares, B.G. and Castello, D.A. (2018) 'Comparisons of complex modulus provided by different DMA', *Polymer Testing*, 72, pp. 394–406.

Hertzberg, R.W., Manson, J.A. and Skibo, M. (1975) 'Frequency sensitivity of

fatigue processes in polymeric solids', *Polymer Engineering & Science*, 15(4), pp. 252–260.

Hertzberg, R.W., Skibo, M.D., Manson, J.A. and Donald, J.K. (1979) 'Comments on "A model of fatigue crack growth in polymers"', *Journal of Materials Science*, 14(7), pp. 1754–1759.

Hibbert, K., Warner, G., Brown, C., Ajide, O., Owolabi, G. and Azimi, A. (2019) 'The Effects of Build Parameters and Strain Rate on the Mechanical Properties of FDM 3D-Printed Acrylonitrile Butadiene Styrene', *Open Journal of Organic Polymer Materials*, 09(01), pp. 1–27.

Hoshyar, A.N., Samali, B., Liyanapathirana, R., Houshyar, A.N. and Yu, Y. (2020) 'Structural damage detection and localization using a hybrid method and artificial intelligence techniques', *Structural Health Monitoring*, 19(5), pp. 1507–1523.

Hu, J. (n.d.) '*An integrated approach to detection of cracks using vibration characteristics*', , pp. 841–853.

Hu, J. and Liang, R.Y. (1993) 'An integrated approach to detection of cracks using vibration characteristics', *Journal of the Franklin Institute*, 330(5), pp. 841–853.

Imeri, A., Fidan, I., Allen, M., Wilson, D.A. and Canfield, S. (2018) 'Fatigue analysis of the fiber reinforced additively manufactured objects', *International Journal of Advanced Manufacturing Technology*, 98(9–12) The International Journal of Advanced Manufacturing Technology, pp. 2717–2724.

Inglis, C.E. (1913) 'Stress in a plate due to the presence of cracks and sharp corners', *Transactions of the Institute of Naval Architects*, 55, pp. 219–241.

Irfan-ul-Haq, M. and Merah, N. (2003) 'Effect of Temperature on Fatigue Crack Growth in CPVC', *Journal of Pressure Vessel Technology*, 125(1), p. 71.

Irwin, G.R. (1957) 'Analysis of Stresses and Strains Near the End of a Crack Traversing a Plate', *Journal of Applied Mechanics*, 24, pp. 361–364.

Isaac, J.P. and Tippur, H. V (2019) 'Quasi-Static and Dynamic Fracture Behaviors of Additively Printed ABS Coupons Studied Using DIC : Role of Build Architecture and Loading Rate', *Conference Proceedings of the Society for Experimental Mechanics Series.*, Vol.8, pp. 11–19.

Itakura, K., Honda, T., Oyama, S., Kida, K., Hazeyama, S. and Kashima, Y. (2013) 'Surface Profile Observation of PTFE Thrust Bearings under Rolling Contact Fatigue in Water', *Advanced Materials Research*, 683, pp. 391–395.

Iwamoto, M., Jinen, E. and Suzuki, M. (1988) 'Effects of crystallinity and temperature on fatigue crack growth behavior of polypropylene. Macroscopic considerations.', *Journal of the Society of Materials Science, Japan*, 37(418), pp. 807–812.

Jap, N.S.F., Pearce, G.M., Hellier, A.K., Russell, N., Parr, W.C. and Walsh, W.R. (2019) 'The effect of raster orientation on the static and fatigue properties of filament deposited ABS polymer', *International Journal of Fatigue*, 124(March) Elsevier, pp. 328–337.

Jassim, Z.A., Ali, N.N., Mustapha, F. and Abdul Jalil, N.A. (2013) 'A review on the vibration analysis for a damage occurrence of a cantilever beam', *Engineering Failure Analysis*, 31 Elsevier Ltd, pp. 442–461.

Jerez-Mesa, R., Travieso-Rodriguez, J.A., Llumà-Fuentes, J., Gomez-Gras, G. and Puig, D. (2017) 'Fatigue lifespan study of PLA parts obtained by additive manufacturing', *Procedia Manufacturing*, 13 Elsevier B.V., pp. 872–879.

Khan, M.A., Cooper, D. and Starr, A. (2009) 'BS - ISO Helical Gear Fatigue Life Estimation and Wear Quantitative Feature Analysis', *Strain*, 45(4), pp. 358–363.

Khan, M.A., Khan, K.A., Khan, S.Z., Nisar, S. and Starr, A. (2018) 'Fracture life estimation of Al-1050 thin beams using empirical data and a numerical approach', *Insight: Non-Destructive Testing and Condition Monitoring*, 60(7), pp. 363–368.

Khan, M.A., Khan, S.Z., Sohail, W., Khan, H., Sohaib, M. and Nisar, S. (2015) 'Mechanical fatigue in aluminium at elevated temperature and remaining life

prediction based on natural frequency evolution', *Fatigue and Fracture of Engineering Materials and Structures*, 38(8), pp. 897–903.

Kharazan, M., Irani, S. and Noorian, M.A. (2020) 'Effect of a breathing crack on the damping changes in nonlinear vibrations of a cracked beam : Experimental and theoretical investigations', *Journal of Vibration and Control*, (August)

Khiem, N.T. and Huyen, N.N. (2017) 'A method for crack identification in functionally graded Timoshenko beam', *Nondestructive Testing and Evaluation*, 32(3) Taylor & Francis, pp. 319–341.

Khiem, N.T. and Tran, H.T. (2014) 'A procedure for multiple crack identification in beam-like structures from natural vibration mode', *JVC/Journal of Vibration and Control*, 20(9), pp. 1417–1427.

Kim, H.-S. and Mai, Y.-W. (1993) 'Effect of temperature on fatigue crack growth in unplasticized polyvinyl chloride', *Journal of Materials Science*, 28(20), pp. 5479–5485.

Kim, H.O.S. and Wang, X.M. (1995) 'Temperature and Frequency Effects on Fatigue Crack Growth in Acrylonitrile-Butadiene-Styrene (ABS)', *Journal of Applied Polymer Science*, 57(7), pp. 811–817.

Kim, H.S. and Wang, X.M. (1994) 'Temperature and frequency effects on fatigue crack growth of uPVC', *Journal of Materials Science*, 29(12), pp. 3209–3214.

Kim, H.S., Wang, X.M. and Abdullah, N.A.H.N. (1994) 'EFFECT OF TEMPERATURE ON FATIGUE CRACK GROWTH IN THE POLYMER ABS', *Fatigue & Fracture of Engineering Materials and Structures*, 17(3), pp. 361–367.

Kirsch, E.G. (1898) 'Die Theorie der Elastizität und die Bedürfnisse der Festigkeitslehre', *Zeitschrift des Vereins deutscher Ingenieure*, 42, pp. 797–807.

Koike, H., Honda, T. and Kida, K. (2011) 'Influence of radial load on PEEK plastic bearings life cycle under water lubricated conditions', *Advanced Materials Research*, 218, pp. 1260–1265.

Koike, H., Kida, K., Honda, T., Mizobe, K., Oyama, S., Rozwadowska, J., Kashima, Y. and Kanemasu, K. (2012) 'Observation of crack propagation in PEEK polymer bearings under water-lubricated conditions', *Advanced Materials Research.*, Vol.566, pp. 109–114.

Kotousov, A.G. (2002) 'On a thermo-mechanical effect and criterion of crack propagation', *International Journal of Fracture*, 114, pp. 349–358.

Kuronuma, Y., Shindo, Y., Takeda, T. and Narita, F. (2011) 'Crack growth characteristics of carbon nanotube-based polymer composites subjected to cyclic loading', *Engineering Fracture Mechanics*, 78(17) Elsevier Ltd, pp. 3102–3110.

Lee, B.H., Abdullah, J. and Khan, Z.A. (2005) 'Optimization of rapid prototyping parameters for production of flexible ABS object', *Journal of Materials Processing Technology*, 169(1), pp. 54–61.

Leigh, S.J., Bradley, R.J., Purssell, C.P., Billson, D.R. and Hutchins, D.A. (2012) 'A Simple, Low-Cost Conductive Composite Material for 3D Printing of Electronic Sensors', *PLoS ONE*, 7(11), pp. 1–6.

Letcher, T. and Waytashek, M. (2014) 'Material property testing of 3D-printed specimen in pla on an entry-level 3D printer', *ASME International Mechanical Engineering Congress and Exposition, Proceedings (IMECE).*, Vol.2A.

Li, H., Jiang, G., Fang, Q. and Wang, T. (2015) 'Experimental investigation on the essential work of mixed-mode fracture of PC/ABS alloy', *Journal of Mechanical Science and Technology*, 29(1), pp. 33–38.

Lim, B.S., Jeong, C.S. and Keum, Y.T. (2003) 'Effect of Temperature on Fatigue Crack Growth in P92 Steel', *Metals and Materials International*, 9(6), pp. 543–547.

Liu, T. and Liu, M. (2014) 'Theoretical Analysis of the Relationship between Elastic Constants of Metals and Remperatures', *Materials for Mechanical Engineering*, 38(3), pp. 85–95.

Long, J., Gholizadeh, H., Lu, J. and Seyfoddin, A. (2017) 'Review: Application of Fused Deposition Modelling (FDM) Method of 3D Printing in Drug Delivery', *Current Pharmaceutical Design*, 23(3), pp. 433–439.

Loya, J.A., Rubio, L. and Fernández-Sáez, J. (2006) 'Natural frequencies for bending vibrations of Timoshenko cracked beams', *Journal of Sound and Vibration*, 290(3–5), pp. 640–653.

Lugo, M., Fountain, J.E., Hughes, J.M., Bouvard, J. and Horstemeyer, M.F. (2014) 'Microstructure-Based Fatigue Modeling of an Acrylonitrile Butadiene Styrene (ABS) Copolymer', *Journal of Applied Polymer Science*, 131(20)

Luo, W., Li, M., Huang, Y., Yin, B. and Hu, X. (2019) 'Effect of Temperature on the Tear Fracture and Fatigue Life of Carbon-Black-Filled Rubber', *Polymers*, 11(5)

Mai, Y.W. and Williams, J.G. (1979) 'Temperature and enviromental effects on the fatigue fracture in polystyrene', *Journal of Materials Science*, 14(8), pp. 1933–1940.

Manson, J.A., Hertzberg, R.W., Kim, S.L. and Skibo, M. (1975) 'The β transition and frequency sensitivity in fatigue crack propagation of polymers', *Polymer*, 16(11), pp. 850–851.

Marco, Y., Huneau, B., Masquelier, I., Saux, V. Le and Charrier, P. (2017) 'Prediction of fatigue properties of natural rubber based on the descriptions of the cracks population and of the dissipated energy', *Polymer Testing*, 59 Elsevier Ltd, pp. 67–74.

MARS, W. V. and FATEMI, A. (2004) 'FACTORS THAT AFFECT THE FATIGUE LIFE OF RUBBER', *Rubber Chemistry and Technology*, 77(3), pp. 391–412.

Mars, W. V and Fatemi, A. (2002) 'A literature survey on fatigue analysis approaches for rubber', *International Journal of Fatigue*, 24(9), pp. 949–961.

Martin, G.C. and Gerberich, W.W. (1976) 'Temperature effects on fatigue crack

growth in polycarbonate', *Journal of Materials Science*, 11(2), pp. 231–238.

Mazanoglu, K. and Sabuncu, M. (2012) 'A frequency based algorithm for identification of single and double cracked beams via a statistical approach used in experiment', *Mechanical Systems and Signal Processing*, 30 Elsevier, pp. 168–185.

Mazanoglu, K., Yesilyurt, I. and Sabuncu, M. (2009) 'Vibration analysis of multiple-cracked non-uniform beams', *Journal of Sound and Vibration*, 320(4–5), pp. 977–989.

Mazidi, M.M., Aghjeh, M.K.R. and Abbasi, F. (2012) 'Evaluation of fracture toughness of ABS polymers via the essential work of fracture (EWF) method', *Journal of Materials Science*, 47(17), pp. 6375–6386.

Mazidi, M.M., Aghjeh, M.K.R. and Abbasi, F. (2013) 'Unstable fracture behavior of rubber toughened poly(styrene-co- acrylonitrile)', *Journal of Macromolecular Science, Part B: Physics*, 52(8), pp. 1158–1182.

McGinty, B. (n.d.) *Fracture Mechanics*. Available at: http://www.fracturemechanics.org/sif.html (Accessed: 27 October 2021).

Meirovitch, L. (2001) *FUNDAMENTALS OF VIBRATIONS*.Internatio. Singapore: McGraw-Hill.

Merah, N., Irfan-Ul-Haq, M. and Khan, Z. (2004) 'Effects of injection molding weld on fatigue crack resistance of CPVC at different temperatures', *Journal of Materials Processing Technology*, 155–156(1–3), pp. 1261–1265.

Merah, N., Khan, Z., Bazoune, A. and Saghir, F. (2006) 'Temperature And Loading Frequency Effects On Fatigue Crack Growth In HDPE Pipe Material', *Arabian Journal for Science and Engineering*, 31(2), pp. 19–30.

Merah, N., Khan, Z., Mezghani, K., Budair, M.O., Younas, M. and Olabisi, O. (2001) 'FATIGUE CRACK PROPAGATION IN WELD ZONE OF CPVC PIPE FITTINGS AT DIFFERENT TEMPERATURES', *Journal of Polymer Engineering*, 21(6), pp. 521–542.

Merah, N., Saghir, F., Khan, Z. and Bazoune, A. (2005) 'A study of frequency and temperature effects on fatigue crack growth resistance of CPVC', *Engineering Fracture Mechanics*, 72(11), pp. 1691–1701.

Michel, J., Manson, J.A. and Hertzberg, R.W. (1984) 'A simple viscoelastic model for fatigue crack propagation in polymers as a function of molecular weight', *Polymer*, 25(11), pp. 1657–1666.

Moradi, S., Makvandi, H., Poorveis, D. and Shirazi, K.H. (2019) 'Free vibration analysis of cracked postbuckled plate', *Applied Mathematical Modelling*, 66 Elsevier Inc., pp. 611–627.

Mortazavian, S. and Fatemi, A. (2015) 'Fatigue behavior and modeling of short fiber reinforced polymer composites: A literature review', *International Journal of Fatigue*, 70 Elsevier Ltd, pp. 297–321.

Mura, A., Ricci, A. and Canavese, G. (2018) 'Investigation of fatigue behavior of ABS and PC-ABS polymers at different temperatures', *Materials*, 11(10), pp. 1–14.

Naebe, M., Abolhasani, M.M., Khayyam, H., Amini, A. and Fox, B. (2016) 'Crack damage in polymers and composites: A review', *Polymer Reviews*, 56(1), pp. 31–69.

Nahvi, H. and Jabbari, M. (2005) 'Crack detection in beams using experimental modal data and finite element model', *International Journal of Mechanical Sciences*, 47(10), pp. 1477–1497.

Nandwana, B.P. and Maiti, S.K. (1997) 'Modelling of vibration of beam in presence of inclined edge or internal crack for its possible detection based on frequency measurements', *Engineering Fracture Mechanics*, 58(3), pp. 193–205.

Nguyen, K.V. (2014) 'Mode shapes analysis of a cracked beam and its application for crack detection', *Journal of Sound and Vibration*, 333(3) Elsevier, pp. 848–872.

Ning, F., Cong, W., Hu, Y. and Wang, H. (2017) 'Additive manufacturing of carbon fiber-reinforced plastic composites using fused deposition modeling : Effects of process parameters on tensile properties', *Journal of Composite Materials*, 51(4), pp. 451–462.

Ning, F., Cong, W., Qiu, J., Wei, J. and Wang, S. (2015) 'Additive manufacturing of carbon fiber reinforced thermoplastic composites using fused deposition modeling', *Composites Part B: Engineering*, 80 Elsevier Ltd, pp. 369–378.

Nitesh A., M. and Vaibhav S., P. (2015) 'Analysis of Crack Detection of A Cantilever Beam using Finite Element Analysis', *International Journal of Engineering Research & Technology*, 4(04), pp. 713–718.

Odahara, S. (2012) 'Mechanical Strength Properties of Wind-Lens Blades', *Nihon Kikai Gakkai Ronbunshu, A Hen/Transactions of the Japan Society of Mechanical Engineers, Part A*, 78(786), pp. 244–248.

Okayasu, M., Yamazaki, T., Ota, K., Ogi, K. and Shiraishi, T. (2013) 'Mechanical properties and failure characteristics of a recycled CFRP under tensile and cyclic loading', *International Journal of Fatigue*, 55 Elsevier Ltd, pp. 257–267.

Ostachowicz, W.M. and Krawczuk, M. (1991) 'Analysis of the effect of cracks on the natural frequencies of a cantilever beam', *Journal of Sound and Vibration*, 150(2), pp. 191–201.

Oyama, S., Kida, K., Santos, E.C., Koike, H., Honda, T. and Kashima, Y. (2012) 'Observations of Cracks from Microscopic Holes of PEEK Bearings under Rolling-Contact Fatigue in Water', *Advanced Materials Research*, 566, pp. 197–202.

Oyama, S., Koike, H., Kashima, Y. and Kida, K. (2013) 'Influence of load and rotation speed on life of PPS radial bearings under water lubricant conditions', *Advanced Materials Research*, 683, pp. 439–443.

Pandey, A.K., Biswas, M. and Samman, M.M. (1991) 'Damage Detection From

Mode Changes In Curvature', *Journal of Sound and Vibration*, 145, pp. 321–332.

Paris, P. and Erdogan, F. (1963) 'A Critical Analysis of Crack Propagation Laws', *Journal of Basic Engineering*

Paris, P.C., Gomez, M.P. and Anderson, W.E. (1961) 'A rational analytic theory of fatigue', *The Trend in Engineering*, 13, pp. 9–14.

Parsons, M., Stepanov, E. V., Hiltner, A. and Baer, E. (2000a) 'Correlation of fatigue and creep slow crack growth in a medium density polyethylene pipe material', *Journal of Materials Science*

Parsons, M., Stepanov, E. V, Hiltner, A. and Baer, E. (2000b) 'Effect of strain rate on stepwise fatigue and creep slow crack growth in high density polyethylene', *Journal of Materials Science*, 5, pp. 1857–1866.

Patil, D.P. and Maiti, S.K. (2003) 'Detection of multiple cracks using frequency measurements', *Engineering Fracture Mechanics*, 70(12), pp. 1553–1572.

Peterson, A.M. (2019) Review of acrylonitrile butadiene styrene in fused filament fabrication: A plastics engineering-focused perspective *Additive Manufacturing*. Elsevier B.V.,

Poduška, J., Hutař, P., Kučera, J., Sadílek, J., Frank, A., Pinter, G. and Náhlík, L. (2017) 'The Effect of Residual Stress on the Process of Crack Growth Rate Determination in Polymer Pipes', *8th International Conference on Materials Structure and Micromechanics of Fracture.*, Vol.258, pp. 174–177.

Popescu, D., Zapciu, A., Amza, C., Baciu, F. and Marinescu, R. (2018) 'FDM process parameters in fl uence over the mechanical properties of polymer specimens : A review', *Polymer Testing*, 69(April), pp. 157–166.

Priyadarshini, A. (2013) '*Identification of cracks in beams using vibrational analysis*', (211)

Pruitt, L. and Bailey, L. (1998) 'Factors affecting near-threshold fatigue crack propagation behavior of orthopedic grade ultra high molecular weight

polyethylene', *Polymer*, 39(8–9), pp. 1545–1553.

Qi, Z., Lu, L., Doan, L., Thota, B., Zeng, D. and Su, X. (2017) 'Frequency Effects on High-Density Polyethylene Failure under Cyclic Loading', *SAE World Congress Experience*.

Qian, G.L., Gu, S.N. and Jiang, J.S. (1990) 'The dynamic behaviour and crack detection of a beam with a crack', *Journal of Sound and Vibration*, 138(2), pp. 233–243.

Rabbi, M.F., Chalivendra, V.B. and Li, D. (2019) 'A Novel Approach to Increase Dynamic Fracture Toughness of Additively Manufactured Polymer', *Experimental Mechanics*, 59(6), pp. 899–911.

Radon, J.C. (1980) 'Fatigue crack growth in polymers', *International Journal of Fracture*, 16(6), pp. 533–552.

Radon, J.C. and Culver, L.E. (1975a) 'Effect of temperature and frequency in fatigue of polymers', *Polymer*

Radon, J.C. and Culver, L.E. (1975b) 'Effect of temperature and frequency in fatigue of polymers', *Polymer Engineering and Science*, 16(7), pp. 539–544.

Radon, J.C. and Culver, L.E. (1975c) 'Fatigue crack growth in polymers. I. Effect of frequency and temperature', *Polymer Engineering & Science*, 15(7), pp. 500–506.

Rankouhi, B., Javadpour, S., Delfanian, F. and Letcher, T. (2016) 'Failure Analysis and Mechanical Characterization of 3D Printed ABS With Respect to Layer Thickness and Orientation', *Journal of Failure Analysis and Prevention*, 16(3) Springer US, pp. 467–481.

Revi, R. and V.S., I. (2015) 'Crack Detection of Propped Cantilever Beam Using Dynamic Analysis', *International Journal of Technical Research and Applications*, 3(4), pp. 2320–8163.

Riddell, M.N., Koo, G.P. and O'Toole, J.L. (1966) 'Fatigue Mechanisms of Thermoplastics', *Polymer Engineering and Science*, 6(4), pp. 363–368.

Riddick, J.C., Haile, M.A., Wahlde, R. Von, Cole, D.P., Bamiduro, O. and Johnson, T.E. (2016) 'Fractographic analysis of tensile failure of acrylonitrile-butadiene-styrene fabricated by fused deposition modeling', *Additive Manufacturing*, 11 Elsevier B.V., pp. 49–59.

Rizos, P.F., Aspragathos, N. and Dimarogonas, A.D. (1990) 'Identification of crack location and magnitude in a cantilever beam from the vibration modes', *Journal of Sound and Vibration*, 138(3), pp. 381–388.

Rodriguez, J.F., Thomas, J.P. and Renaud, J.. (2001) 'Mechanical behavior of acrylonitrile butadiene styrene (ABS) fused deposition materials . Experimental investigation', *Rapid Prototyping Journal*, 7(3), pp. 148–158.

Rodríguez, J.F., Thomas, J.P. and Renaud, J.E. (2003) 'Mechanical behavior of acrylonitrile butadiene styrene fused deposition materials modeling', *Rapid Prototyping Journal*, 9(4), pp. 219–230.

Romaszko, M., Sapiński, B. and Sioma, A. (2015) 'Forced vibrations analysis of a cantilever beam using the vision method', *Journal of Theoretical and Applied Mechanics (Poland)*, 53(1), pp. 243–254.

Ruellan, B., Cam, J. Le, Jeanneau, I., Canévet, F., Mortier, F. and Robin, E. (2019) 'Fatigue of natural rubber under different temperatures', *International Journal of Fatigue*, 124(October 2018) Elsevier, pp. 544–557.

Rybachuk, M., Alice Mauger, C., Fiedler, T. and Öchsner, A. (2017) 'Anisotropic mechanical properties of fused deposition modeled parts fabricated by using acrylonitrile butadiene styrene polymer', *Journal of Polymer Engineering,* 37(7), pp. 1–8.

Sadeghi, F., Jalalahmadi, B., Slack, T.S., Raje, N. and Arakere, N.K. (2009) 'A review of rolling contact fatigue', *Journal of Tribology*, 131(4), pp. 1–15.

Safai, L., Cuellar, J.S., Smit, G. and Zadpoor, A.A. (2019) 'A review of the fatigue behavior of 3D printed polymers', *Additive Manufacturing*, 28(March) Elsevier, pp. 87–97.

Saghir, F., Merah, N., Khan, Z. and Bazoune, A. (2005) 'Modeling the combined effects of temperature and frequency on fatigue crack growth of chlorinated polyvinyl chloride (CPVC)', *Journal of Materials Processing Technology*, 164–165, pp. 1550–1553.

Saib, K.S., Evans, W.J. and Isaac, D.H. (1993) 'The role of microstructure during fatigue crack growth in poly(aryl ether ether ketone) (PEEK)', *Polymer*, 34(15), pp. 3198–3203.

Sauer, J.A. and Richardson, G.C. (1980) 'Fatigue of polymers', *International Journal of Fracture*, 16(6), pp. 499–532.

Schirmeister, C.G., Hees, T., Licht, E.H. and Mülhaupt, R. (2019) '3D printing of high density polyethylene by fused fi lament fabrication', *Additive Manufacturing*, 28(February) Elsevier, pp. 152–159.

Seichter, S., Archodoulaki, V., Koch, T., Holzner, A. and Wondracek, A. (2017) 'Investigation of different in fl uences on the fatigue behaviour of industrial rubbers', *Polymer Testing*, 59 Elsevier Ltd, pp. 99–106.

Shah, A., Stepanov, E. V., Hiltner, A., Baer, E. and Klein, M. (1997) 'Correlation of fatigue crack propagation in polyethylene pipe specimens of different geometries', *International Journal of Fracture*, 84(2), pp. 159–173.

Shah, A., Stepanov, E. V., Klein, M., Hiltner, A. and Baer, E. (1998) 'Study of polyethylene pipe resins by a fatigue test that simulates crack propagation in a real pipe', *Journal of Materials Science*

Shi, X., Ando, M., Kashima, Y. and Kida, K. (2016) 'Crack observation of PPS polymer thrust bearings under RCF test in water', *Advanced Materials Research*, 703, pp. 178–182.

Shi, X., Kida, K., Kashima, Y., Shi, X., Kida, K. and Kashima, Y. (2014) 'Surface crack and wear of PPS polymer thrust bearings under rolling contact fatigue in water Surface crack and wear of PPS polymer thrust bearings under rolling contact fatigue in water', *Materials Research Innovations*, 18

Shinde, Y.D. and Katekar, S.D. (2014) 'Vibration Analysis of Cantilever Beam With Single Crack using Experimental Method', *International Journal of Engineering Research & Technology*, 3(5), pp. 1644–1648.

Shirashi, T., Ogiyama, H. and Tsukuda, H. (1997) 'Effect of Compressive Stress on Fatigue by Crack Propagation in Polymers', *J. Soc. Mat. Sci., Japan*, 46(11), pp. 1255–1260.

Shojib Hossain, M., Espalin, D., Ramos, J., Perez, M. and Wicker, R. (2014) 'Improved Mechanical Properties of Fused Deposition Modeling-Manufactured Parts Through Build Parameter Modifications', *Journal of Manufacturing Science and Engineering*, 136(6), p. 061002.

Shrestha, R., Simsiriwong, J., Shamsaei, N. and Moser, R.D. (2016) 'Cyclic deformation and fatigue behavior of polyether ether ketone (PEEK)', *International Journal of Fatigue*, 82 Elsevier Ltd, pp. 411–427.

Stein, R.S. (1994) 'Polymer science and engineering: The shifting research frontiers', *Journal of Polymer Science, Part A: Polymer Chemistry*

Suresh, J.A., Saravana Kumar, G., Ramu, P. and Rengaswamy, J. (2018) 'Fatigue Life Characterization of Additively Manufactured Acrylic like Poly-Jet Printed Parts', in *Advances in Structural Integrity*. , pp. 623–632.

Suyitno, S. and Pujilaksono, L. (2017) 'Fatigue crack propagation of ultra-high molecular weight polyethylene', *7th International Annual Engineering Seminar*.

Takei, A. and Matter, S. (2018) 'Crack propagation in porous polymer sheets with different pore sizes', *MRS Communications*, 8, pp. 1477–1482.

Tee, Y.L., Loo, M.S. and Andriyana, A. (2018) 'Recent advances on fatigue of rubber after the literature survey by Mars and Fatemi in 2002 and 2004', *International Journal of Fatigue*, 110(January) Elsevier, pp. 115–129.

Torrado, A.R., Shemelya, C.M., English, J.D., Lin, Y., Wicker, R.B. and Roberson, D.A. (2015) 'Characterizing the effect of additives to ABS on the mechanical property anisotropy of specimens fabricated by material extrusion

3D printing', *Additive Manufacturing*, 6 Elsevier B.V., pp. 16–29.

Travieso-Rodriguez, J.A., Jerez-Mesa, R., Llumà, J., Traver-Ramos, O., Gomez-Gras, G. and Rovira, J.J.R. (2019) 'Mechanical properties of 3D-printing polylactic acid parts subjected to bending stress and fatigue testing', *Materials*, 12(23)

Türk, D., Brenni, F., Zogg, M. and Meboldt, M. (2017) 'Mechanical characterization of 3D printed polymers for fiber reinforced polymers processing', *Materials and Design*, 118 Elsevier Ltd, pp. 256–265.

Tuttle, M.E. (n.d.) *A brief introduction to polymeric materials*

Ultimaker (2018) *Mechanical properties Injection molding 3D printing Technical Data Sheet ABS*. Available at: https://support.ultimaker.com/hc/en-us/article_attachments/360010199279/TDS_ABS_v3.011_-en.pdf (Accessed: 18 July 2021).

Waller, J.H., Lalande, L., Leterrier, Y. and Månson, J.A.E. (2011) 'Modelling the effect of temperature on crack onset strain of brittle coatings on polymer substrates', *Thin Solid Films*, 519(13) Elsevier B.V., pp. 4249–4255.

Wang, C.-H. (1996) *Introduction To Fracture Mechanics*. Kensington: DSTO Aeronautical and Maritime Research Laboratory.

Wann, R.J., Martin, G.C. and Gerberich, W.W. (1976) 'The mechanical behavior of polyarylsulfone', *Polymer Engineering & Science*, 16(9), pp. 645–651.

Westergaard, H.M. (1939) 'Bearing pressures and cracks', *Journal of Applied Mechanics*, 6(2), pp. A49–A53.

Williams, J.. (1977) 'A model of fatigue crack growth in polymers', *Journal of Materials Science*, 12(12), pp. 2525–2533.

Wyzgoski, M.G., Novak, G.E. and Simon, D.L. (1990) 'Fatigue fracture of nylon polymers Part 1 Effect of frequency', *Journal of Materials Science*, 25(10), pp. 4501–4510.

Xu, Z. and Ma, L. (2007) *Structural Dynamics*.Ver. 1.Anqi, T. (ed.) Beijing:

Science Press.

Zai, B.A., Khan, M., Khan, K.A., Mansoor, A., Shah, A. and Shahzad, M. (2019a) 'The role of dynamic response parameters in damage prediction', *Proceedings of the Institution of Mechanical Engineers, Part C: Journal of Mechanical Engineering Science*, 233(13) SAGE Publications Ltd, pp. 4620–4636.

Zai, B.A., Khan, M.A., Khan, K.A. and Mansoor, A. (2020a) 'A novel approach for damage quantification using the dynamic response of a metallic beam under thermo-mechanical loads', *Journal of Sound and Vibration*, 469, p. 115134.

Zai, B.A., Khan, M.A., Khan, S.Z., Asif, M., Khan, K.A., Saquib, A.N., Mansoor, A., Shahzad, M. and Mujtaba, A. (2020b) 'Prediction of crack depth and fatigue life of an acrylonitrile butadiene styrene cantilever beam using dynamic response', *Journal of Testing and Evaluation*, 48(2), pp. 1520–1536.

Zai, B.A., Khan, M.A., Mansoor, A., Khan, S.Z. and Khan, K.A. (2019b) 'Instant dynamic response measurements for crack monitoring in metallic beams', *Insight: Non-Destructive Testing and Condition Monitoring*, 61(4) British Institute of Non-Destructive Testing, pp. 222–229.

Zein, I., Hutmacher, D.W., Tan, K.C. and Teoh, S.H. (2002) 'Fused deposition modeling of novel scaffold architectures for tissue engineering applications', *Biomaterials*, 23, pp. 1169–1185.

Zhang, H., Cai, L., Golub, M., Zhang, Y., Yang, X., Schlarman, K. and Zhang, J. (2018) 'Tensile , Creep , and Fatigue Behaviors of 3D-Printed Acrylonitrile Butadiene Styrene', *Journal of Materials Engineering and Performance*, 27(1) Springer US, pp. 57–62.

Zhang, J., He, X.D., Suo, B. and Du, S.Y. (2008) 'Elastic – plastic finite element analysis of the effect of compressive loading on crack tip parameters and its impact on fatigue crack propagation rate', *Engineering Fracture Mechanics*, 75(18) Elsevier Ltd, pp. 5217–5228.

Zhang, K. and Yan, X. (2017) 'Multi-cracks identification method for cantilever

beam structure with variable cross-sections based on measured natural frequency changes', *Journal of Sound and Vibration*, 387 Elsevier, pp. 53–65.

Zhang, S.-U., Han, J. and Kang, H.-W. (2017) 'Temperature-dependent mechanical properties of ABS parts fabricated by fused deposition modeling and vapor smoothing', *International Journal of Precision Engineering and Manufacturing*, 18(5), pp. 763–769.

Zhang, Y., Vassilopoulos, A.P. and Keller, T. (2010) 'Effects of low and high temperatures on tensile behavior of adhesively-bonded GFRP joints', *Composite Structures*, 92(7) Elsevier Ltd, pp. 1631–1639.

Zhou, Y. and Brown, N. (1992) 'The Mechanism of Fatigue Failure in a Polyethylene Copolymer', *Polymer Physics*, 30(5), pp. 477–487.

Ziemian, C., Sharma, M. and Ziemi, S. (2012) 'Anisotropic Mechanical Properties of ABS Parts Fabricated by Fused Deposition Modelling', in Gokcek, M. (ed.) *Mechanical Engineering*. London: IntechOpen Limited.

Ziemian, C.W., Ziemian, R.D. and Haile, K. V (2016) 'Characterization of stiffness degradation caused by fatigue damage of additive manufactured parts', *Materials and Design*, 109 Elsevier Ltd, pp. 209–218.

Ziemian, S., Okwara, M. and Ziemian, C.W. (2015) 'Tensile and fatigue behavior of layered acrylonitrile butadiene styrene', *Rapid Prototyping Journal*, 21(3), pp. 270–278.

APPENDICES

Appendix A MATLAB Code for Analytical Models

```matlab
clc
clear all

load('validation.mat');
% load('Emodel.mat');
% load('Lmodel.mat');

%%

syms beta x E I b H a L row f k t w m J l AA BB CC DD EE;

I = b*H^3/12;


f = 0.6384*(a/H)^2-1.035*(a/H)^3+3.7201*(a/H)^4-5.1773*(a/H)^5 ...
    +7.553*(a/H)^6-7.3324*(a/H)^7+2.4909*(a/H)^8;
k = E*b*H^2*(H-a)/(H*72*pi*f);

t = E*I/k;
J = 0;

BC1 = [1 0 1 0 0 0 0 0];
BC2 = [0 1 0 1 0 0 0 0];
BC3 = [sin(beta*x) cos(beta*x) sinh(beta*x) cosh(beta*x) ...
    -sin(beta*x) -cos(beta*x) -sinh(beta*x) -cosh(beta*x)];
BC4 = [-cos(beta*x) sin(beta*x) -cosh(beta*x) -sinh(beta*x) ...
    cos(beta*x)+t*beta*sin(beta*x) -sin(beta*x)+t*beta*cos(beta*x) ...
    cosh(beta*x)-t*beta*sinh(beta*x) sinh(beta*x)-t*beta*cosh(beta*x)];
BC5 = [-sin(beta*x) -cos(beta*x) sinh(beta*x) cosh(beta*x) ...
    sin(beta*x) cos(beta*x) -sinh(beta*x) -cosh(beta*x)];
BC6 = [-cos(beta*x) sin(beta*x) cosh(beta*x) sinh(beta*x) ...
    cos(beta*x) -sin(beta*x) -cosh(beta*x) -sinh(beta*x)];
BC7 = [0 0 0 0 -sin(beta*L)-beta^3*J/(row*b*H)*cos(beta*L)...
    -cos(beta*L)+beta^3*J/(row*b*H)*sin(beta*L)...
    sinh(beta*L)-beta^3*J/(row*b*H)*cosh(beta*L)...
    cosh(beta*L)-beta^3*J/(row*b*H)*sinh(beta*L)];
BC8 = [0 0 0 0 -cos(beta*L)+m*beta/(row*b*H)*sin(beta*L)...
    sin(beta*L)+m*beta/(row*b*H)*cos(beta*L)...
    cosh(beta*L)+m*beta/(row*b*H)*sinh(beta*L)...
    sinh(beta*L)+m*beta/(row*b*H)*cosh(beta*L)];
matrix = [BC1; BC2; BC3; BC4; BC5; BC6; BC7; BC8];
sys = det(matrix);

%%

sys = matlabFunction(sys);

U = 0.002;
row = 1070;
L = 150/1000;
b = 10/1000;
H = 3/1000;
I = b*H^3/12;
m = 0.6/1000;

T = 50;


E = (Emodel(1)*T^2+Emodel(2)*T+Emodel(3))*10^6;
delta = (Lmodel(1)*T^2+Lmodel(2)*T+Lmodel(3))*10^6/E;


%%

depth = 0.0001:0.0001:0.0029;
l = 0.005:0.01:0.025;
% l = 0.015;
% depth = 0.0001;
```

```matlab
s = zeros(length(l),length(depth));
omega_n = zeros(length(l),length(depth));
frequency = zeros(length(l),length(depth));
mode = cell(length(l),length(depth));
amplitude = zeros(length(l),length(depth));
t1 = zeros(length(l),length(depth));
K = zeros(length(l),length(depth));

for i = 1:length(l)
    for j = 1:length(depth)
        xx = l(i);
        a = depth(j);
        t1(i) = double(subs(t));
        s(i,j) = vpasolve(sys(H,L,a,b,beta,m,row,xx)==0,beta,[0.001 inf]); % beta
        omega_n(i,j) = s(i,j)^2*((E*I)/(row*b*H))^0.5;
        frequency(i,j) = omega_n(i,j)/(2*pi);
        A1 = [1 0 1 0 0 0 0 0];
        A2 = [0 1 0 1 0 0 0 0];
        A3 = [sin(s(i,j)*xx) cos(s(i,j)*xx) sinh(s(i,j)*xx) cosh(s(i,j)*xx) ...
            -sin(s(i,j)*xx) -cos(s(i,j)*xx) -sinh(s(i,j)*xx) -cosh(s(i,j)*xx)];
        A4 = [-cos(s(i,j)*xx) sin(s(i,j)*xx) -cosh(s(i,j)*xx) -sinh(s(i,j)*xx) ...
            cos(s(i,j)*xx)+t1(i)*s(i,j)*sin(s(i,j)*xx) -
sin(s(i,j)*xx)+t1(i)*s(i,j)*cos(s(i,j)*xx) ...
            cosh(s(i,j)*xx)-t1(i)*s(i,j)*sinh(s(i,j)*xx) sinh(s(i,j)*xx)-
t1(i)*s(i,j)*cosh(s(i,j)*xx)];
        A5 = [-sin(s(i,j)*xx) -cos(s(i,j)*xx) sinh(s(i,j)*xx) cosh(s(i,j)*xx) ...
            sin(s(i,j)*xx) cos(s(i,j)*xx) -sinh(s(i,j)*xx) -cosh(s(i,j)*xx)];
        A6 = [-cos(s(i,j)*xx) sin(s(i,j)*xx) cosh(s(i,j)*xx) sinh(s(i,j)*xx) ...
            cos(s(i,j)*xx) -sin(s(i,j)*xx) -cosh(s(i,j)*xx) -sinh(s(i,j)*xx)];
        A7 = [0 0 0 0 -sin(s(i,j)*L)-s(i,j)^3*J/(row*b*H)*cos(s(i,j)*L)...
            -cos(s(i,j)*L)+s(i,j)^3*J/(row*b*H)*sin(s(i,j)*L)...
            sinh(s(i,j)*L)-s(i,j)^3*J/(row*b*H)*cosh(s(i,j)*L)...
            cosh(s(i,j)*L)-s(i,j)^3*J/(row*b*H)*sinh(s(i,j)*L)];
        A8 = [0 0 0 0 -cos(s(i,j)*L)+m*s(i,j)/(row*b*H)*sin(s(i,j)*L)...
            sin(s(i,j)*L)+m*s(i,j)/(row*b*H)*cos(s(i,j)*L)...
            cosh(s(i,j)*L)+m*s(i,j)/(row*b*H)*sinh(s(i,j)*L)...
            sinh(s(i,j)*L)+m*s(i,j)/(row*b*H)*cosh(s(i,j)*L)];
        A = [A1; A2; A3; A4; A5; A6; A7; A8];
        xxx = null(A);

        Ycorrelation =
xxx(5)*sin(s(i,j)*L)+xxx(6)*cos(s(i,j)*L)+xxx(7)*sinh(s(i,j)*L)+...
            xxx(8)*cosh(s(i,j)*L);
        xxx = xxx/Ycorrelation;

        Y1 = xxx(1)*sin(s(i,j)*x)+xxx(2)*cos(s(i,j)*x)+xxx(3)*sinh(s(i,j)*x)+...
            xxx(4)*cosh(s(i,j)*x);
        Y2 = xxx(5)*sin(s(i,j)*x)+xxx(6)*cos(s(i,j)*x)+xxx(7)*sinh(s(i,j)*x)+...
            xxx(8)*cosh(s(i,j)*x);
        w = omega_n(i,j);        % calculate amplitude under natural frequency

        diffY1 = diff(Y1);
        diffY1 = matlabFunction(diffY1);
        diffY2 = diff(Y2);
        diffY2 = matlabFunction(diffY2);
        diffdiffY2 = diff(diff(Y2));
        diffdiffY2 = matlabFunction(diffdiffY2);
        AA = E*I*(int(diff(Y1,2)^2,x,0,xx)+int(diff(Y2,2)^2,x,xx,L))+...
            2*(E*I)^2/k*diffdiffY2(xx)^2;
        BB = delta*AA;
        CC = row*b*H*(int(Y1^2,x,0,xx)+int(Y2^2,x,xx,L))+m*diffdiffY2(L)^2;
        DD = (AA-w^2*CC)*U*w^2*(row*b*H+m)*(int(Y1,x,0,xx)+int(Y2,x,xx,L))/...
            ((AA-w^2*CC)^2+BB^2*w);
        EE = -BB*w*DD/(AA-w^2*CC);
        amp = Y2*(DD^2+EE^2+U^2)^0.5;

        amp = matlabFunction(amp);
        amplitude(i,j) = abs(amp(E,H,a,b,L))*1000; % unit mm
        mode(i,j) = {xxx};
    end
end

frequency = frequency';
```

149

```matlab
%% stress calculation
clear all
clc

c = 1.875104;
L = 150/1000;
l = 5/1000;
b = 10/1000;
H = 3/1000;
I = b*H^3/12;
E = 1831; % change Young's Modulus with correct value

%%
load('FT.mat'); %delete this line, using import to import
start = round(3.96142600000000/(1/2048)+1); % pick the start pick time
finish = round(30.7612300000000/(1/2048)+1); % pick the end pick time

t = FT(start:finish,1); % change FT to your data name
t = t - t(1);
acc = FT(start:finish,2);
acc = lowpass(acc,5,2048);
data = [t acc];

%

peak = data(1,:);

j = 2;

for i = 2:(length(t)-1)
    if (acc(i)-acc(i-1))*(acc(i+1)-acc(i))<0
        peak(j,:) = [t(i) acc(i)];
        j = j+1;
    end
end

t_peak = peak(:,1);
acc_peak = peak(:,2);

% Calculate displacement amplitude

amp_peak = zeros(length(acc_peak),1);
for i =1:(length(acc_peak)-1)
    T = 2*(t_peak(i+1)-t_peak(i));
    f = 1/T;
    amp_peak(i+1)=abs(acc_peak(i+1)-acc_peak(i))/2/(2*pi*f)^2;
end

% Calculate curvature

beta = c/L;
A = zeros(length(acc_peak),1);
cu = zeros(length(acc_peak),1);
for i = 1:length(acc_peak)
    A(i) = amp_peak(i)/(sin(c)+(cos(c)+cosh(c))/(sin(c)-sinh(c))*cos(c)-sinh(c)...
        -(cos(c)+cosh(c))/(sin(c)-sinh(c))*cosh(c));
    B = (cos(c)+cosh(c))/(sin(c)-sinh(c))*A(i);
    C = -A(i);
    D = -B;
    cu(i) = beta^2*(-A(i)*sin(beta*l)-B*cos(beta*l)+C*sinh(beta*l)+D*cosh(beta*l));
end

% Calculate bending moment

M = zeros(length(acc_peak),1);
for i = 1:length(acc_peak)
    M(i) = abs(E*I*cu(i));
end

% Calculate maximum stress

stress_max = zeros(length(acc_peak),1);
for i = 1:length(amp_peak)
    stress_max(i) = 6*M(i)/(b*H^2);
```

```
end
```

```
amplitude = amplitude';
```

Appendix B MATLAB Code for Experimental Data Process

```
data = table2array(IT);
```

```
Acc=data(:,2);
Time=data(:,1);
```

```
%velocity=cumtrapz(Time,Acc);Dis = cumtrapz(Time,velocity);
```

```
figure(2)
plot(Time,Acc)
grid on
```